
**Microcantilever Actuation Generated by
Redox-induced Surface Stress**

Vincent Tabard-Cossa

Department of Physics

McGill University

Montréal, Québec

Canada

December, 2005

A Thesis submitted to

McGill University

in partial fulfillment of the requirements for the degree of

Doctor of Philosophy

© Vincent Tabard-Cossa, 2005



Library and
Archives Canada

Bibliothèque et
Archives Canada

Published Heritage
Branch

Direction du
Patrimoine de l'édition

395 Wellington Street
Ottawa ON K1A 0N4
Canada

395, rue Wellington
Ottawa ON K1A 0N4
Canada

Your file *Votre référence*
ISBN: 978-0-494-25264-2
Our file *Notre référence*
ISBN: 978-0-494-25264-2

NOTICE:

The author has granted a non-exclusive license allowing Library and Archives Canada to reproduce, publish, archive, preserve, conserve, communicate to the public by telecommunication or on the Internet, loan, distribute and sell theses worldwide, for commercial or non-commercial purposes, in microform, paper, electronic and/or any other formats.

The author retains copyright ownership and moral rights in this thesis. Neither the thesis nor substantial extracts from it may be printed or otherwise reproduced without the author's permission.

AVIS:

L'auteur a accordé une licence non exclusive permettant à la Bibliothèque et Archives Canada de reproduire, publier, archiver, sauvegarder, conserver, transmettre au public par télécommunication ou par l'Internet, prêter, distribuer et vendre des thèses partout dans le monde, à des fins commerciales ou autres, sur support microforme, papier, électronique et/ou autres formats.

L'auteur conserve la propriété du droit d'auteur et des droits moraux qui protègent cette thèse. Ni la thèse ni des extraits substantiels de celle-ci ne doivent être imprimés ou autrement reproduits sans son autorisation.

In compliance with the Canadian Privacy Act some supporting forms may have been removed from this thesis.

Conformément à la loi canadienne sur la protection de la vie privée, quelques formulaires secondaires ont été enlevés de cette thèse.

While these forms may be included in the document page count, their removal does not represent any loss of content from the thesis.

Bien que ces formulaires aient inclus dans la pagination, il n'y aura aucun contenu manquant.


Canada

Table of Contents

TABLE OF CONTENTS.....	III
ABSTRACT	V
RÉSUMÉ.....	VII
ACKNOWLEDGMENTS.....	IX
STATEMENT OF ORIGINALITY	XI
1 INTRODUCTION	1
1.1 MICROMECHANICAL CANTILEVER-BASED SENSORS	4
1.1.1 Modes of operation and detection methods	5
1.1.2 Sensing applications.....	7
1.1.3 Interpretation of the cantilever's mechanical response.....	11
1.1.4 Outline.....	13
2 EXPERIMENTAL METHODS	17
2.1 COMBINED ELECTROCHEMISTRY AND DIFFERENTIAL CANTILEVER-BASED SENSING ..	19
2.1.1 Cell	21
2.1.2 Electrical Contact to the WE.....	23
2.1.3 Microcantilever as an Electrode	24
2.1.4 Deflection Sensing Scheme.....	29
2.2 MATERIALS AND METHODS FOR ELECTROCHEMICAL EXPERIMENTS.....	32
3 CALIBRATION.....	35
3.1 OPTICAL BEAM DEFLECTION TECHNIQUE.....	36
3.1.1 Interferometric Calibration	36
3.1.2 Geometrical Calibration.....	38
3.1.3 Index of Refraction	42
3.2 QUANTIFYING SURFACE STRESS	45
3.3 INSTRUMENT SENSITIVITY AND RESOLUTION	48
3.4 TESTING OF THE INSTRUMENT.....	49
3.4.1 Validation of the Calibration.....	49
3.4.2 Differential Mode	52
4 SURFACE STRESS AT THE SOLID-LIQUID INTERFACE	57
4.1 THERMODYNAMIC OF THE SOLID-LIQUID INTERFACE	59
4.1.1 Definitions	59
4.1.2 Debate on the thermodynamics of solid electrodes	63
4.1.3 Model of the double layer structure.....	65
4.2 SURFACE ENERGY VERSUS SURFACE STRESS	69
4.3 CHARGE-INDUCED SURFACE STRESS	76
4.4 SPECIFIC ADSORPTION AND A SIMPLE MODEL OF THE ORIGIN OF SURFACE STRESS	80
4.5 EFFECT OF MORPHOLOGY, ADHESION AND CLEANLINESS OF THE AU SURFACE ON THE MEASURED SURFACE STRESS	86
4.6 SUMMARY.....	97
5 REDOX-INDUCED SURFACE STRESS OF POLYPYRROLE-BASED ACTUATORS.....	101
5.1 SAMPLE PREPARATION.....	104
5.1.1 Pre-treatment of the WE gold surface	104

5.1.2	<i>Deposition of PPy</i>	105
5.2	REDOX-INDUCED SURFACE STRESS.....	111
5.2.1	<i>Actuation Principle of conducting polymers</i>	111
5.2.2	<i>Surface stress during redox reaction in PPy(DBS)</i>	112
5.2.3	<i>Passivity of the backside</i>	114
5.2.4	<i>Redox inhibiting electrolyte</i>	115
5.2.5	<i>1st Reduction Scan</i>	119
5.2.6	<i>Life Time: Multiple Cycles</i>	122
5.3	SUMMARY	129
6	SUMMARY AND OUTLOOK	131
6.1	SUMMARY	131
6.2	OUTLOOK.....	136
	APPENDIX	142
	REFERENCES	147

Abstract

Electrochemically-induced changes in surface stress at the solid-liquid interface are measured using a differential cantilever-based sensor. The simultaneous, in situ measurements of the current (charge) and interfacial stress changes are performed by employing an AFM cantilever as both the working electrode (in a conventional three-probe electrochemical cell configuration) and as the mechanical transducer (bending of the cantilever). The custom-built instrument achieves a surface stress sensitivity of 1×10^{-4} N/m and a dynamic range of 5×10^5 . Combining electrochemistry with cantilever-based sensing provides the extra surface characterization capability essential for the interpretation of the origin of the surface stress.

The objective of the present study is to gain a better understanding of the mechanisms responsible for the nanomechanical motion of cantilever sensors during *adsorption* and *absorption* processes. The study of these simple model systems will lead to a general understanding of the cantilever-based sensor's response and provide insights into the physical origin of the measured surface stress.

The surface stress generated by the electrochemically-controlled absorption of ions into a thin polypyrrole film is investigated. A compressive change in surface stress of about -2 N/m is measured when the polymer is electrochemically switched between its oxidized and neutral (swollen) state. The volume change of the polymer phase with respect to the gold-coated cantilever is shown to be responsible for the mechanical motion observed.

The potential-induced surface stress and surface energy change on an Au(111)-textured cantilever, in a 0.1 M HClO₄ electrolyte, are simultaneously measured. These measurements revealed that for solid electrodes these two thermodynamic parameters are significantly different. In the double layer region, a surface stress change of -0.55 ± 0.06 N/m is measured during ClO₄⁻ adsorption whereas the surface energy variation is smaller by one order of magnitude. The origin of the surface stress change at the metal-electrolyte interface is understood by the variation in electron density at the surface which alters the inter-atomic bonds strength between surface atoms, while the specificity of adsorption of ions is found to be mostly responsible for the fine structure of the surface stress profile.

Résumé

Le changement de tension de surface induit de manière électrochimique à l'interface solide-liquide est mesuré à l'aide d'un microlevier utilisé comme capteur biochimique. Ces mesures simultanées du changement de tension de l'interface et du courant électrique sont réalisées en utilisant un microlevier d'AFM à la fois comme l'électrode de travail et comme transducteur mécanique. Cet instrument est doté d'une sensibilité de 1×10^{-4} N/m. L'association de ce type de capteur biochimique à des techniques de caractérisations de surfaces électrochimiques permet une interprétation plus explicite de l'origine de la tension de surface.

Cette étude a été réalisée dans le but d'acquérir une meilleure compréhension des mécanismes responsables du mouvement nanomécanique du microlevier lors de processus d'adsorption et d'absorption. Elle contribuera à comprendre l'origine physique de la tension de surface et ainsi améliorer la performance de ce type de capteur biochimique.

La tension de surface générée lors de l'absorption d'ions par un film de polypyrrole, recouvrant un microlevier, a été étudiée. Un changement de tension de surface de l'ordre de -2 N/m a été mesuré lors de la transformation électrochimique du film de polypyrrole de son état oxydé à son état neutre. Le changement de volume du polymère par rapport au substrat du microlevier a été identifié comme étant responsable du mouvement mécanique du dispositif.

La tension et l'énergie de surface induites par le changement de potentiel d'un microlevier d'Au(111), dans une solution de 0.1 M HClO_4 , ont été mesurées simultanément. Ces mesures ont révélé que dans le cas d'électrodes solides ces

deux paramètres thermodynamiques diffèrent de manière significative. Un changement de tension de surface de -0.55 ± 0.06 N/m a été mesuré lors de l'adsorption d'ions ClO_4^- dans la double couche électrique, alors que la variation de l'énergie de surface était inférieure par un ordre de grandeur. L'origine de la tension de surface est expliquée par un changement dans la distribution électronique de la surface d'or modifiant la force des liaisons inter-atomiques entre les atomes de la surface. La spécificité de l'adsorption est quant à elle responsable de la structure dans la courbe de la tension de surface en fonction du potentiel.

Acknowledgments

I would like to thank a number of people who have contributed to the development of this thesis and who have made my overall experience as a graduate student at McGill University enjoyable and rewarding.

First I would like to thank my supervisor Dr. Peter Grutter for introducing me to the field of Nanoscience and for giving me the opportunity to work on this interesting project, allowing my passion for both physics and chemistry to be fully expressed. His patience and support has given me the freedom to explore this research field and the opportunity to become independent in my research activities. His insightful guidance and infectious enthusiasm allowed my research skills to develop and my creativity to flourish.

I must thank my friend and colleague, Dr. Michel Godin, for his constant guidance and support. I am forever indebted to him for countless hours of fruitful discussions. Without him this thesis would not have been possible.

I am especially grateful to Dr. Ian Burgess for providing answers to my questions concerning the electrochemical aspect of my research. His advice and expertise had a great impact on my research. His work ethic was inspirational.

I thank every member of the sensor group for their assistance and technical support. Prof. Bruce Lennox for offering his expertise and advice on the chemistry aspect of my project. Dr. Luc Y. Beaulieu for his highly valuable input to this project as a post-doctoral member. Prof. Peter Williams for his contribution to this project during his sabbatical stay at McGill. Brian Seivewright, Olivier Laroche, Dr. H el ene Bourque, all deserve to be recognize for their input through useful discussions and technical help on various aspects of this project. I am indebted to my colleague Tanya Monga for proofreading this thesis and for her exceptional assistance in the last year of this study. Her enthusiasm, sense of humor and motivation had a great impact on this project.

I thank Prof. Antonella Badia and her students for initially introducing me to some aspect of this project and for many helpful discussions.

I am indebted to my friends and lab-mates for their support and discussions. In particular, Manuel Pumarol, Ben Smith, Jeffrey Mativetsky, Mehdi El Ouali, Nela Durisic, Romain Stomp, Alex Wlasenko, Dr. Henrik Mortensen, and Dr. Mark Roseman. Special thanks to Dr. Yoichi Miyahara and Cristiano Dias for many helpful discussions. I must also acknowledge all of the other group members that I have worked with in the lab over the years.

I thank the all technical staff of the Physics Department at McGill University, in particular Eddie Del Campo, Leo Nikkinen, Steve Kecani, and Frank Van Gils. I want to specially thank Robert Gagnon for all of his technical assistance. He has been a great source of knowledge and expertise.

Financial support through McGill Major postgraduate scholarships as well as from the Physics Department, the Center for Materials Physics and my supervisor Dr. Peter Grutter was also greatly appreciated.

Je voudrais aussi remercier tous mes amis, de Nantes à Montréal en passant par Mexico, pour m'avoir permis de garder les pieds sur terre pendant ce long processus et de m'avoir fait découvrir des choses que je n'aurais pas connues autrement. Michel, Kimio, Mouna, Sergio, Erwan et Sylvain, merci à tous.

Un grand merci à mes parents, Annie et Daniel, pour leurs encouragements et leur soutien ainsi que pour la confiance dont ils m'ont fait part tout au long de mes études. Vous avez été extraordinaires.

Élise, ton affection, ton humour, et surtout ta présence à mes côtés, m'ont aidé à donner un sens à ces derniers mois. Ton dynamisme dans le travail m'a servi de modèle pour me surpasser. Tu es une source de motivation formidable. Je t'aime.

Statement of Originality

The author claims the following aspects of the thesis constitute original scholarship and an advancement of knowledge. Some of these findings have been published (see appendix for complete publication list).

- The design and construction of a differential cantilever-based sensor integrated with an electrochemical instrument. This unique system uses commercially-available atomic force microscope (AFM) cantilevers and is capable of quantitative surface stress measurements at the solid-liquid interface with a sensitivity of 1×10^{-4} N/m. This system is composed of two AFM cantilever sensors. The first active cantilever serves as the working electrode (in a conventional three-probe electrochemical cell configuration) and as the mechanical transducer (bending of the microcantilever), yielding simultaneous, real-time, in situ measurements of the current and interfacial stress changes. The second cantilever serves as a reference sensor to detect any unwanted cantilever deflection resulting from temperature variations, mechanical vibrations and/or uncontrolled chemical reactions. This unique system provides complementary information essential for the interpretation the origin of the measured surface stress.
- **Vincent Tabard-Cossa et al.**, *Sensors and Actuators B* 107 (2005) 233-241.
- The simultaneous measurement, using AFM cantilevers, of surface stress and surface energy changes. Within the electrical double layer, from +200 mV to +700 mV (vs. Ag/AgCl), a compressive surface stress change of -0.55 ± 0.06 N/m was measured whereas the surface energy varied only by ~ -0.065 N/m.

- The surface stress induced during ClO_4^- adsorption on polycrystalline Au(111) was found to be in excellent agreement with results obtained on single crystal Au(111). For anion adsorption, the effect of grain boundaries and grain size on the measured surface stress is insignificant. In addition the adhesion of an evaporated metal film was found to be sufficient in completely transferring the stress to the underlying substrate. On the contrary, discontinuities in the film were found to quantitatively affect the magnitude of the surface stress change.

- The cleanliness of the gold surface was found to have a direct impact on both the magnitude and the shape of the potential-induced surface stress curve. These measurements possibility explained some previously reported controversial AFM cantilever sensor results.

- The measurement of the potential-induced surface stress on thiol-modified electrodes. The results revealed a parabolic dependence of surface stress on potential, qualitatively similar to the change in surface energy.

- The quantification of the surface stress evolution during the anomalous first reduction of a dodecyl benzenesulfonate-doped polypyrrole, PPy(DBS), 300 nm thin film. An average tensile surface stress change of $+1.0 \pm 0.5$ N/m was measured which was attributed to a non-reversible structural change of the freshly polymerized film.
 - **Vincent Tabard-Cossa** et al., *Journal of Physical Chemistry B* 109 (2005) 17531-17537

- The identification of two main competing origins of surface stress acting on a PPy(DBS)-covered gold-coated cantilever actuator device; one purely mechanical due to a volume change of the conducting polymer with respect to the substrate and a second charge-induced owing to the interaction of anions of the supporting electrolyte with exposed gold.
 - **Vincent Tabard-Cossa** et al., *Journal of Physical Chemistry B* 109 (2005) 17531-17537.

1 Introduction

Today and tomorrow's bio-chemical sensor applications, ranging from biomedical analysis and medical diagnostics to environmental monitoring or quality control for the food industry, require devices with smaller size, higher sensitivity, improved selectivity, faster response times and sure enough low cost. The necessity for new sensing technologies to meet these demands is driving extensive research efforts in many areas of science and engineering.

The concept of chemical sensors encompasses two main features [1]; a physical transducer and a chemically receptive and selective layer (see Figure 1). The chemical layer provides specific binding sites for the target analyte of interest. The selectivity of the receptive layer can be designed employing principles of molecular and biomolecular recognition; for example antigen-antibody binding (i.e. any chemicals, bacteria, viruses, or pollen binding to a specific protein). Other surface functionalizations such as self-assembled monolayer and polymer coatings are also employed. The selectivity is then achieved by a specific chemical reaction on the functionalized sensor's surface. However, absolute selectivity remains a major challenge. In fact, most sensing technologies are faced

with the issue of non-specific interactions which can complicate the sensor response, produce false positives, and affect the reproducibility and the suitability of the sensor system for a particular application. The chemical layer must therefore be designed to maximize the sensor's sensitivity to the specific response. An otherwise completely opposite approach is to examine the non-specific response of an array of sensors analyzed using principle components analysis (PCA) or other statistical tools. This method has given rise to electronic noses capable of distinguishing a variety of odors from the vapor phase via the swelling of polymer coatings and measuring the associated volume changes or conductivity changes [2,3]. The unique identification fingerprints of sensor arrays can offer a solution to the selectivity issue in some chemical sensing technologies in a similar way as surface enhanced Raman scattering (SERS) sensors [4] which provide a distinctive spectrum for a given molecule.

Once the analyte is recognized by the chemical layer, the transducer converts the chemical stimulus into a measurable output signal, as shown in Figure 1.ⁱ Both the chemical layer and the physical transducer impose limitations on the performance of a certain class of sensors. Nevertheless it is often the physical transducer which determines the limits of detection attainable. The search for new transduction principles is therefore constantly stimulated.

ⁱ An example of one of the most commonly used sensors is the glucose sensor used by diabetics which is based on an electrochemical transduction mechanism.

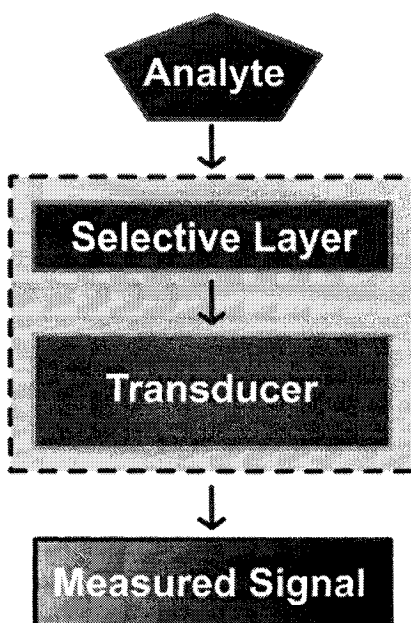


Figure 1 : Generalized schematic representation of a chemical sensor. The analyte is recognized by the selective and receptive layer. In response the transducer produces an output signal.

Each step depicted in Figure 1 has an influence on the sensor's performance. From the mechanism that drives the analyte to the sensor (e.g. microfluidic, activated diffusion, etc.), to the instrument reading the output signal of the transducer; all stages are the subject of extensive research efforts. This thesis will focus on the investigation of the transduction mechanism behind a given class of sensors: cantilever-based surface stress sensors. By studying simple model systems a general understanding for the physical origins of the measured surface stress will be developed. This understanding will enable enhancement of cantilever-based sensors performance through optimization of the response signal, control over the reproducibility, and determination of the ultimate sensitivity.

1.1 Micromechanical cantilever-based sensors

The advent of atomic force microscopy (AFM) in 1986 [5], and the advances in micromechanical systems (MEMS) have allowed the AFM microcantilevers to emerge as a new family of transducers.

It was quickly realized, in the early days of AFM, that during experiments the cantilever experiences bending due to fluctuations in temperature of the environment as a consequence of the bimetallic effect. Having a different coefficient of thermal expansion, the reflecting metal coating on the silicon or silicon nitride cantilever expands more than the substrate, thus deforming the beam. A further example is the thermal effect of the laser, used to detect the displacement of the cantilever, which under certain circumstances can introduce noise (i.e. deflection due to laser heating) in the acquired image. In addition, while performing AFM measurements it was observed that the resonance frequency is affected by variation in the relative humidity of the air. The adsorption of water on the surface of the cantilever increases its mass and thus lowers its resonance frequency. These observations suggested that the AFM cantilever could serve as a versatile sensor which could be tailored for the detection of specific physical and chemical events. The transduction mechanism of cantilever sensors is based on mechanical movements or deformations of the beam when subjected to a particular stimulus. Up to now cantilever-based sensors have been shown to be capable of measuring surface stress changes [6,7], mass [8,9,10], and heat [11,12,13,14].

1.1.1 Modes of operation and detection methods

Micromechanical cantilever-based sensors can be operated, sometime simultaneously, in two modes: the *static mode* where the bending of the cantilever is measured and the *dynamic mode* where the change in resonance frequency of the cantilever is monitored (see Figure 2). The static mode is sensitive to surface stress changes and temperature fluctuations whereas the dynamic mode is susceptible to mass variations (microbalance)ⁱⁱ.

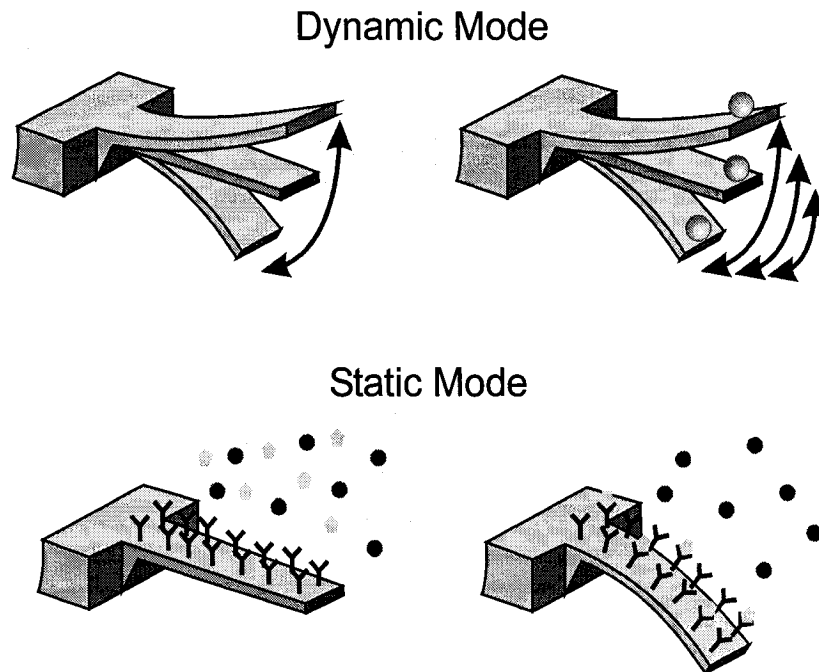


Figure 2: Schematic drawings of the two possible modes of operation of cantilever-based sensors.

ⁱⁱ Note that changes in surface stress also affect the resonance frequency of the cantilever and hence the mass detection (see G.Y. Chen, T. Thundat, E.A. Wachter and R.J. Warmack, *J. Appl. Phys.* 77, 1995, pp. 3618-3622)

The bending and resonance frequency shifts can be measured with high precision using a variety of methods. The simplest way of measuring cantilever deflection is by optical beam deflection as in most AFM instruments. In the optical beam deflection technique a laser diode is focused at the free end of the cantilever and the reflected laser beam is monitored using a position sensitive photodetector. The typical displacement sensitivity achieved using this technique is on the order of 10^{-9} m. Its advantages are its simplicity, linear response, and lack of electrical connections. However it suffers some limitations. A calibration is needed in order to obtain the recorded signal in terms of the actual cantilever deflection. Index of refraction changes of the surrounding medium of the cantilever can produce artificial deflection and the technique cannot be used in opaque media such as blood.

Another optical method which can attain better performance is interferometry. When using a fiber optic interferometer, the interference signal from the reflected light off the cleaved end of the fiber optic and off the cantilever surface is a direct measure of the cantilever displacement. Deflection in the range of 10^{-11} to 10^{-13} m can be measured [15]. However, this method is confronted with a few technical problems. The fiber must be delicately positioned in proximity of the cantilever and only small displacements can be measured. Rugar et al. [16,17] are now using this technique for single-spin magnetic resonance microscopy.

Another alternative is the piezoresistance method. Piezoresistivity is the variation in the bulk resistivity under applied stress. When a silicon cantilever is stressed because of its bending, a highly doped region will change resistance in a sensitive way. The variation of cantilever resistance is typically measured with a dc-biased

Wheatstone bridge. The advantage of this technique is that the sensor and the detection scheme can be easily integrated into lab-on-a-chip type devices. In addition it is more compatible with large array formats. However, this method possesses electrical connections which need to be protected for experiments performed in liquids and requires current to flow through the cantilever. This results in heat dissipation and thermal drifts which causes parasitic cantilever deflections.

Other, less widely used, readout schemes exist such as the capacitive method, piezoelectric method and electron tunneling. More recently, displacement detection methods for nanoscale cantilevers were implemented. Cleland et al. [18] developed a scheme based on capacitively coupling a nanobeam to a single electron transistor (SET) achieving sensitivity down to 10^{-14} m.

1.1.2 Sensing applications

The work presented in this thesis makes use of cantilever-based sensors in the static mode together with an optical beam deflection technique to measure surface stress changes. For a typical sensing experiment one surface of the cantilever is rendered sensitive to a specific chemical or molecular analyte while the opposing surface is passivated. When the analyte of interest interacts with the sensitized surface a surface stress change can be induced. The difference in surface stress induced on the functionalized side relative to the passivated side results in a mechanical deflection of the cantilever. The surface stress change is directly

proportional to the cantilever deflection and is described by an improved form of Stoney's equation (see section 3.2).

Figure 3 is a schematic of the adsorption induced surface stress during the self-assembly of alkanethiol monolayer on gold. For this particular molecular sensing experiment, one surface of the cantilever is rendered sensitive to thiol molecules through a gold coating while the opposing passivated surface is bare silicon or silicon nitride (cantilever material).

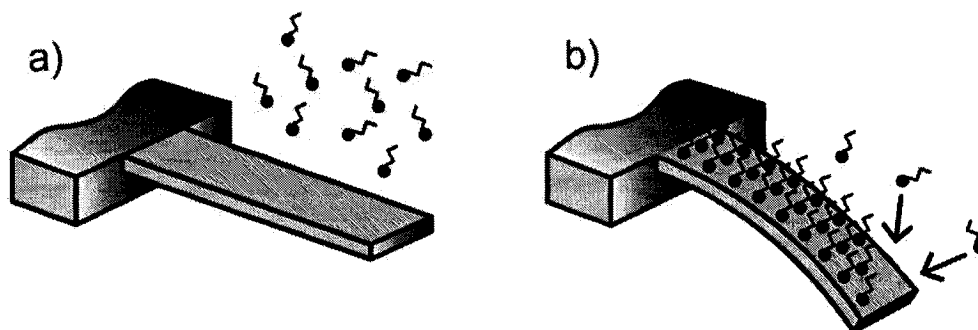


Figure 3 : Schematic of molecularly induced surface stress. (a) The gold-coated side (upper surface) is the sensitized surface whereas the silicon or silicon underside is the passivated surface. (b) Upon molecular adsorption a surface stress is generated on the gold-coated surface of the cantilever. The difference in surface stress of the two opposing surfaces results in a mechanical deflection of the cantilever.

Passivating the backside of microcantilevers poses a difficult challenge and is the subject of ongoing research [19]. The choice of a particular surface passivation approach strongly depends on the analyte to be detected. In the experiment described in Figure 3 it is the high affinity of sulfur for gold which renders the

gold-coated side the sensitive surface and by default the silicon nitride side passivated [106,7]. On the contrary, if the same microcantilever is used as a pH sensor [20,21], the gold-coated side will, this time, serve as a passivation layer, while the silicon nitride side will change its surface charge density (by protonation). There are further examples in the literature using alkanethiol self-assembled monolayers (SAMs) with specific end groups (-CH₃ as opposed to -COOH) or bovine serum albumin (BSA) for surface passivation. Nonetheless, the degree of passivity of a passivated surface is an important issue to consider when performing experiments and interpreting the results since the effect of non-specific interactions is extremely difficult to prevent. Differential measurements, subtracting the signal of a reference cantilever from that of an active cantilever, can provide a solution to non-specific interaction problems.

Some very promising biomedical applications, relevant to motivate the work presented in this thesis, were tested using cantilever-based sensors. Several groups have functionalized the surface of cantilevers to perform biomolecular sensing experiments. Fritz et al. [22] have reported direct conversion of receptor-ligand interactions into a mechanical response. For such detection, they have immobilized different single stranded DNA (ssDNA) probes on the surface of an array of two gold-coated cantilevers via thiol chemistry. Subsequently, the cantilever array was exposed to the complementary oligonucleotide to one of the ssDNA probes. The resulting hybridization, through steric and/or electrostatic interactions, generated the surface stress and the mechanical response of the cantilever. It is only through the differential deflection (see Figure 4C) that the

molecular recognition signal, with single-base mismatch sensitivity, is obtained as the response of individual cantilevers is affected by large non-specific interactions. Hybridization of DNA on the surface of cantilevers induced a surface stress change on the order of a few mN/m which generated a ~ 10 nm differential deflection signal. Given the deflection noise of 0.5 nm, a concentration detection limit of 10 nM is expected by this technique. More recently McKendry et al. [23] reported a similar detection limit of target oligonucleotide using an array of eight cantilevers as shown in Figure 4. These breakthrough experiments suggest the capability to detect single base mutations and the ability to perform DNA sequencing by hybridization.

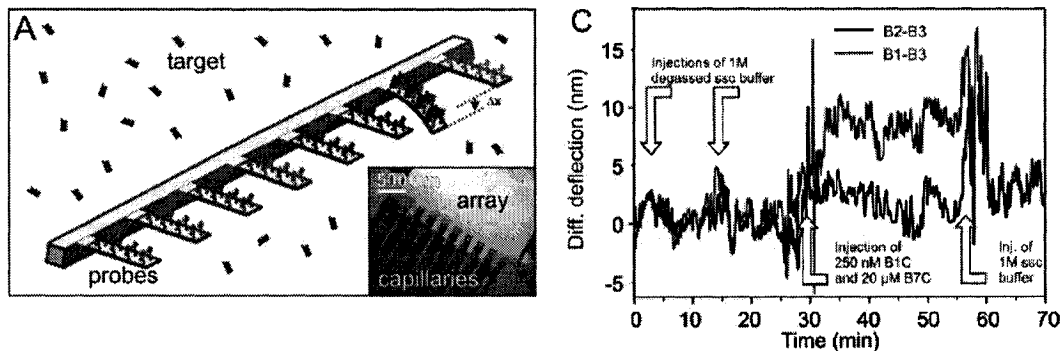


Figure 4: A) Illustration of the basic principle of mechanical label free biodetection with an array of eight cantilevers. The inset shows how the immobilization of different probes is performed with the help of microcapillaries. C) Detection of 250 nM B1C (complementary target to the immobilized probe on cantilever B1) in the presence of 20 μ M of a non-complementary probe. B2 and B3 serve as reference cantilevers. The differential deflection indicates a ~ 10 nm deflection (blue curve) with respect to the baseline (black curve). This corresponds to a compressive surface stress change of ~ 2 mN/m. Data reproduced from McKendry et al. Proc. Natl. Acad. Sci. U.S.A. 99 (2002) 9738.

1.1.3 Interpretation of the cantilever's mechanical response

Other groups have also reported DNA hybridization and protein detection using cantilever sensors [24,25,26]. In particular, Hansen et al. [27], using a single cantilever setup, reported results contradictory (in part) to those by Fritz et al. [22], which led the authors to argue some of the interpretations previously put forward to explain the mechanism behind of the sensor's response. Both analyses were later challenged, to a different extend, by Alvarez et al. [28] in an article showing the failures as much as the successes of DNA hybridization experiments on cantilevers.

It is clear that, overall, biosensing experiments are highly non-trivial to perform. The cantilever motion and the surface stress generated from biomolecular interactions arising from van der Waals forces, steric hindrance and/or electrostatic repulsion are small. One clear issue is that the magnitude of the response of cantilever transducers to this type of specific interaction is comparable to non-specific signals. Unfortunately, most of the work published thus far lacks comprehensive experiments to investigate the effect of the non-specific interactions and the nature of the interactions that actually generate the measured surface stress. The packing density and the ordering of probes on the sensor's surface must have a role in generating the observed response. Moreover, the role of spacer and filler molecules must be clearly identified. For example, defects in the sensing layer can provide binding sites for anions and/or ssDNA to

interact with the gold surface and generate a surface stress change, since it has been shown that there is a base-dependent competitive adsorption of ssDNA on gold [29].

Wu et al. [30] touched on the issue of the origin of cantilever motion induced by biomolecular interactions. They revealed how the ionic concentration of the buffer solution affected the magnitude and sign of the surface stress response. Hence, they demonstrated how configurational entropy changes of the DNA probe immobilized on the surface controlled the direction of motion of cantilevers.

Nevertheless the different mechanisms (electrostatic repulsion, entropic changes or steric hindrance) suggested by these groups for the generation of the observed surface stress have never been compared with precise theoretical models to ascertain the physical origin of the measured forces. It follows that the interpretation of the origin of the surface stress in cantilever-based sensors remains uncertain.

A major limitation of today's cantilever sensors is the very small surface stress (\sim mN/m) generated during biomolecular recognition events. If cantilever-based sensors are to become a viable technology for medical diagnostics or other practical applications, the magnitude of the surface stress signal needs to be significantly improved. While current efforts focus on the microfabrication of cantilevers with smaller spring constants, to increase the sensitivity, this approach also amplifies the parasitic deflections arising from non-specific interactions and thermal fluctuations (bimetallic effect). For example, research is being conducted to develop of polymer-based cantilever array systems [31], employing SU-8 (an

epoxy-based photoresist) as a polymer material which has a Young's modulus about 40 times lower than that of silicon. Few studies have aimed at understanding the physical origins of the induced surface stress. In order to maximize the sensor's response, a general understanding for the relevance of the various interactions that contribute to a measured surface stress needs to be established. Ultimately, this understanding will enable the optimization of sensor performance by suitably tailoring the properties of the sensing layer, favoring interactions that will generate the maximum surface stress response.

1.1.4 Outline

To develop an understanding of the origin of the nanomechanical motion of cantilever sensors, the surface stress change on the surface of the cantilever should be studied in a reproducible and controlled fashion. In this work, control over the surface stress change is achieved by combining electrochemistry together with cantilever-based sensing. The integrated electrochemical aspect of the combined instrument provides the extra surface and interfacial characterization capabilities required to interpret the surface stress signal. This thesis investigates the transduction mechanism of microcantilever-based sensors under controlled, well defined surface science conditions. By studying simple *adsorption* and *absorption* systems an understanding of the parameters influencing the surface stress sensor's response is developed.

This work begins with a description of the experimental methods used in this study. Chapter 2 presents the design and development of a differential cantilever-based surface stress sensor integrated with electrochemistry. The combined instrument employs an AFM cantilever as both the working electrode and as the mechanical transducer for simultaneous, in situ measurement of the current (charge) and interfacial stress changes. Chapter 3 follows with a description of the calibration procedures used to convert the instrument output signal into an actual cantilever deflection, and the subsequent conversion of this deflection into an accurate surface stress change. Chapter 4 introduces and reviews the concept of surface stress and surface energy along with a description of the solid-liquid interface. The difference between these two thermodynamic quantities is examined as a function of electric potential and charge density on the cantilever surface. In addition, the effect of specific adsorption (charge transfer) together with a qualitative description from an atomistic viewpoint of the origin of the surface stress at the solid-liquid interface is provided. The effect of morphology, adhesion, and cleanliness of the gold sensing surface on the measured surface stress is also investigated. As a practical application of the knowledge developed in the previous chapters, the mechanism of actuation of electrochemically controlled conjugated organic thin film is studied. Chapter 5 presents the redox-induced surface stress of polypyrrole-based microactuators. The surface stress during absorption of ions into a conducting polymer-coated cantilever is investigated. The surface stress sensor's response during the anomalous first reductive scan is studied. Lastly, the lifetime of the microactuator device is

examined as a function of the nature of the supporting electrolyte. To conclude this thesis chapter 6 provides a summary of the work and offers an outlook.

2 Experimental Methods

In microcantilever-based sensing experiments the interpretation of the origin of the measured surface stress is not trivial based on the microcantilever response alone. For this reason, it can be advantageous to combine this type of sensors with other measurement techniques. I have combined a differential microcantilever-based sensor with electrochemical techniques by using the micromechanical cantilever sensor as the working electrode (WE), yielding simultaneous, *in situ* measurements of current (or charge) and surface stress changes. Combining electrochemistry with microcantilever-based sensing allows for kinetics measurements to be performed on clean well-defined surfaces, and often the ability to study processes occurring on the microcantilever in a reversible fashion. The development of this combined instrument is further motivated by the results of M. Godin's PhD. Thesis [118], which revealed that the most relevant of the various interactions contributing to the surface stress, during alkanethiol molecules adsorption, is the charge transfer between the sulfur and gold atoms and the associated electronic redistribution of the gold surface. In fact, the electrochemical instrument allows for the surface charge density on the cantilever to be experimentally determined. Ultimately, this will allow for the possibility of

direct quantitative testing of the theoretical models aimed at understanding the physical origins of the measured surface stress. Additionally, during sensing experiments, electrochemistry provides control over the orientation of the probe molecules on the cantilever surface [32] and gives the ability to drive target molecules to the surface (i.e. activated diffusion). This last point is particularly important, as diffusion alone is often not fast enough at low analyte concentrations to bring a molecule in contact with the sensing layer [33].

This chapter describes a complete electrochemical microcantilever-based sensor instrument and the experimental procedure to perform surface stress measurements. In section 2.1 I will provide a complete description of the integration of a differential micromechanical cantilever-based sensor with a standard three-probe electrochemical system. In particular, in section 2.1.2, I present a fast, easy, and clean approach to isolate the active microcantilever electrical contact point from the electrolyte solution. Moreover, in section 2.1.3, I implement a method for reproducibly defining a 1.0 mm^2 working electrode area, which allows for a quantitative measure of the current density, and therefore knowledge of the charge consumed per unit area.

2.1 Combined Electrochemistry and Differential Cantilever-based Sensing

Figure 5 is a photograph of the differential microcantilever-based sensor combined with a standard three-electrode system composed of an Ag/AgCl reference electrode (RE), and a platinum wire as a counter electrode (CE). A gold-coated, rectangular-shaped, tipless silicon microcantilever is used as the active microcantilever, serving as both the working electrode (WE) and as the sensing platform of the surface stress sensor. A second identical gold-coated microcantilever is used as a reference sensor. A commercial potentiostat is used to apply a potential to the active microcantilever (WE) and to monitor the current response during cyclic voltammetric experiments. In parallel, an optical beam technique is used to monitor the microcantilevers' deflections.

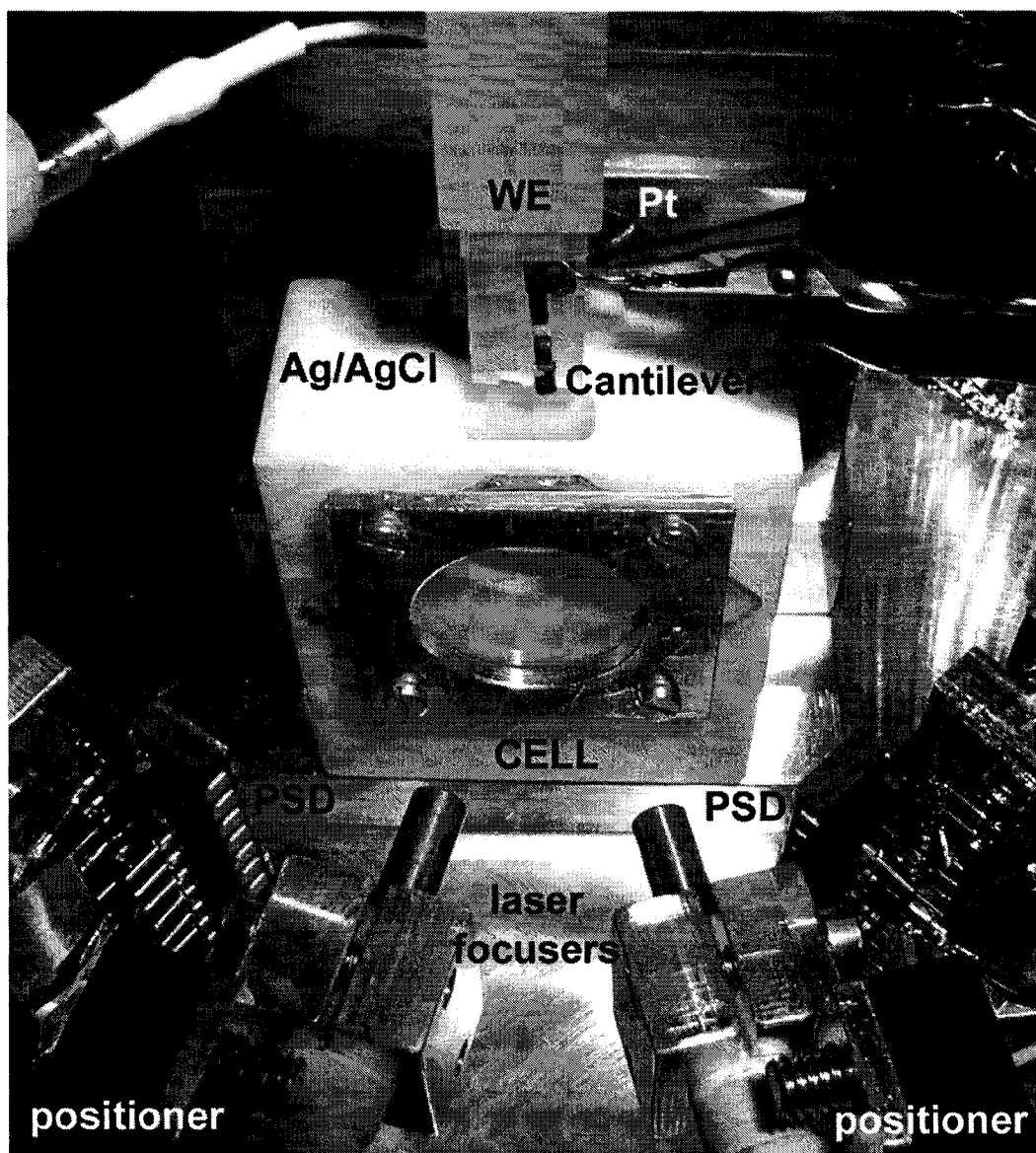


Figure 5: Optical photograph of the system showing the configuration of the liquid cell and electrodes (microcantilever: WE, Ag/AgCl: RE, and Pt: CE). The microcantilever is mechanically clamped with the clip onto a Kel-F rod which is attached to the micropositioner. The deflection sensing components (laser focusers and PSDs) are also shown. The second laser focuser and PSD are present for the differential sensor mode, eliminating thermal drifts and mechanical vibrations from the measured signal. Note that the mechanical clip for the reference cantilever is missing in this picture.

2.1.1 Cell

The cell was designed to accommodate the constraints imposed by the electrochemical and microcantilever sensor experiments. The electrochemical aspect of the combined instrument requires three electrodes, RE, CE and WE. The WE is the platform on which the electrochemical reaction takes place. This electrochemical reaction can result in organic or metal thin film deposition, ion adsorption or produce any types of redox reactions on the WE surface, etc. This reaction is compensated at the CE. Current flows between the WE and CE. The presence of the RE provides an equilibrium reaction that determines the reference level in the electrochemical cell. No current flows through the RE. The CE area is about 100 times larger than the WE area, to accommodate the compensating reaction. The electrodes are placed at equal distance (~1cm) from each other, as shown schematically in Figure 6a. This separation distance prevents interference between the compensating reaction species with the WE electrochemical reaction, although this distance could certainly be reduced. The cell was machined from a chemically inert material, Teflon™. The external dimensions are 40 mm (wide) ×45 mm (high) ×20 mm (deep) with an inner cell diameter of 20 mm. The cell has a volume of 6 cm³, in order to accommodate the size of the RE, and to facilitate calibration of the optical deflection sensing scheme. Ultimately it is the size of the available commercial RE which imposes the constraint on the dimension of the cell. The electrodes are inserted at the top of the cell through openings of the same diameter. This helps to minimize the exposure to air and evaporation of the

electrolyte solution. The front of the cell is fitted with a glass window to accommodate the optical beam deflection sensing scheme, and to provide direct visual access to the microcantilevers for control of their immersion depth into the electrolyte solution and alignment of the laser beams onto the apex of each microcantilever. Another glass window at the back of the cell, when removed, grants access to the back of the microcantilevers for calibration of the deflection measurements by interferometry [56]. Aluminium frames press the two glass windows onto Viton o-rings to seal the cell. During measurements, the cell is secured onto an aluminium base plate.

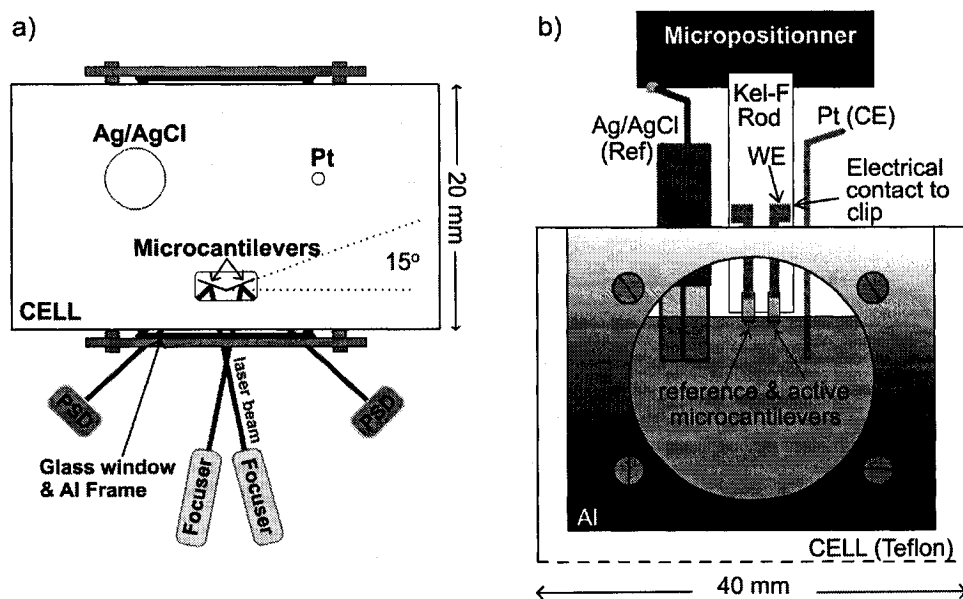


Figure 6: a) Top view of the system. The laser light passes through a glass window and is reflected off the cantilever before reaching the PSD. The three electrodes present in the cell form an equilateral triangle. b) Front view of the cell. The vertically-mounted cantilever chip is immersed into the electrolyte solution using a micropositioner. On the Kel-F rod, the cantilever chip is mechanically held by a metal clip with which electrical contact is made. The Kel-F rod can be flipped in order to reflect the laser beam on either side of the cantilevers.

2.1.2 Electrical Contact to the WE

Electrical contacts to each electrode are made outside the cell so as to avoid the possibility of electrochemical reactions occurring at the contact points. In particular, due to its small size, special care was taken to protect the WE contact point from the electrolyte solution. The active (WE) and the reference microcantilever chips sit in grooves and are mechanically held with beryllium/copper clips [34] at the end of a Kel-F® rod attached to a micropositioner. The grooves are angled at 15° with respect to the front glass window of the cell. This angle is used to separate the reflected spot from the glass and the reflected spot from the microcantilever's apex impinging the position sensing photodetector (PSD), since the former can alter the deflection measurements [90] (Figure 6a). The active (WE) and reference microcantilevers are vertically immersed into the electrolyte using the micropositioner [35] so that only the microcantilevers and a small portion of their chip are in the solution. Electrical contact is made only to the active microcantilever (WE), on the gold-coated side, at the end of the chip located outside the electrolyte solution, with the beryllium/copper clip, as illustrated in Figure 7 and Figure 6b. This technique offers a clean, easy and quick way to isolate the electrical contact point from the electrolyte solution. It avoids the use of epoxy resin to encapsulate the electrical contact as employed by other groups [89,90,91,92,96], which may induce some

level of contamination in the electrochemical cell. No electrical contact is made to the reference microcantilever.

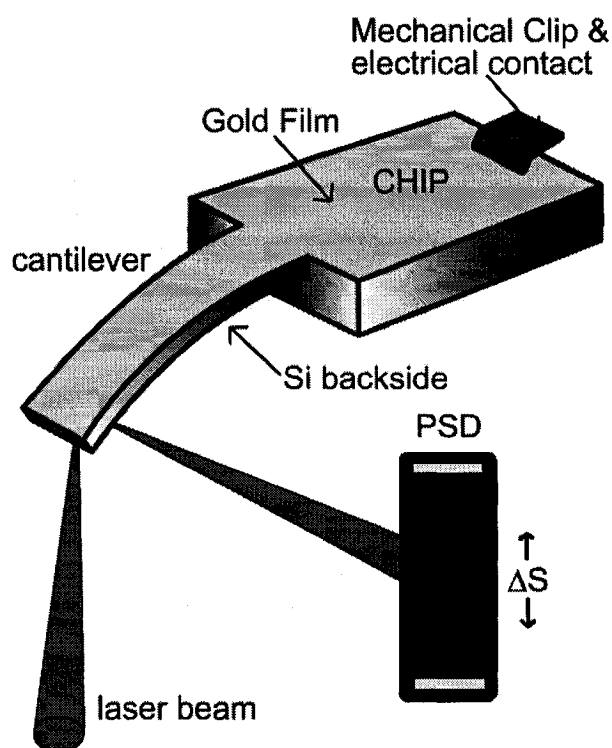


Figure 7: Schematic representation of the optical beam deflection technique used to monitor the microcantilever deflection. The laser reflects off the apex of the Si side of the microcantilever and then hits the PSD. A gold film covers the other side of the microcantilever and the chip, rendering the surface conductive. Electrical contact is made to the gold-coated side at the opposite end of the chip.

2.1.3 Microcantilever as an Electrode

The microcantilever sensors used herein are rectangular silicon cantilevers from MikroMasch type CSC12/without Al/tipless, with a typical length, width, thickness, and spring constant of 350 μm , 35 μm , 1 μm , and 0.03 N/m, respectively

(Figure 8). However, these dimensions were independently measured by SEM for each microcantilever in order to improve the accuracy of the measured surface stress. In addition, the spring constant was determined each time as described in section 3.2

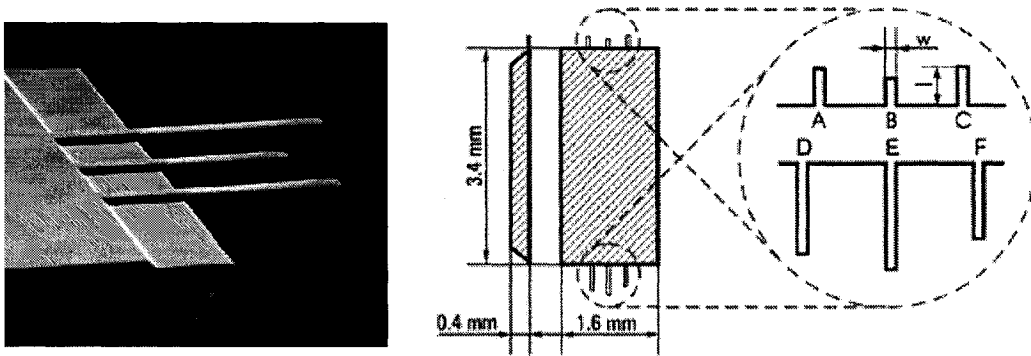


Figure 8: a) SEM image of the MikroMasch type CSC12/without Al/tipless cantilevers on the chip. b) Schematic of the chip holding 6 rectangular silicon cantilevers. Cantilever E are typically used. (SEM image by MikroMasch)

To perform electrochemical experiments, the surface of a silicon microcantilever was rendered electrically conductive by thermally evaporating [36] a 100 nm film of Au [37] on a 10 nm Ti [38] adhesion layer. The evaporation was conducted under a pressure below 5.0×10^{-6} Torr, at a rate of 0.14 nm/s for Au, and 0.04 nm/s for Ti. Radiative heating of the evaporation boat increased the microcantilevers temperature [39] to 130 ± 20 °C. The resulting film has an average grain size of 100 ± 60 nm with a RMS roughness of 1.0 ± 0.2 nm, on a $1 \mu\text{m}$ length scale as determined by STM imaging (Figure 9). X-ray diffraction revealed a strongly (111) textured Au film. The metal films were deposited on one side of the active microcantilever.

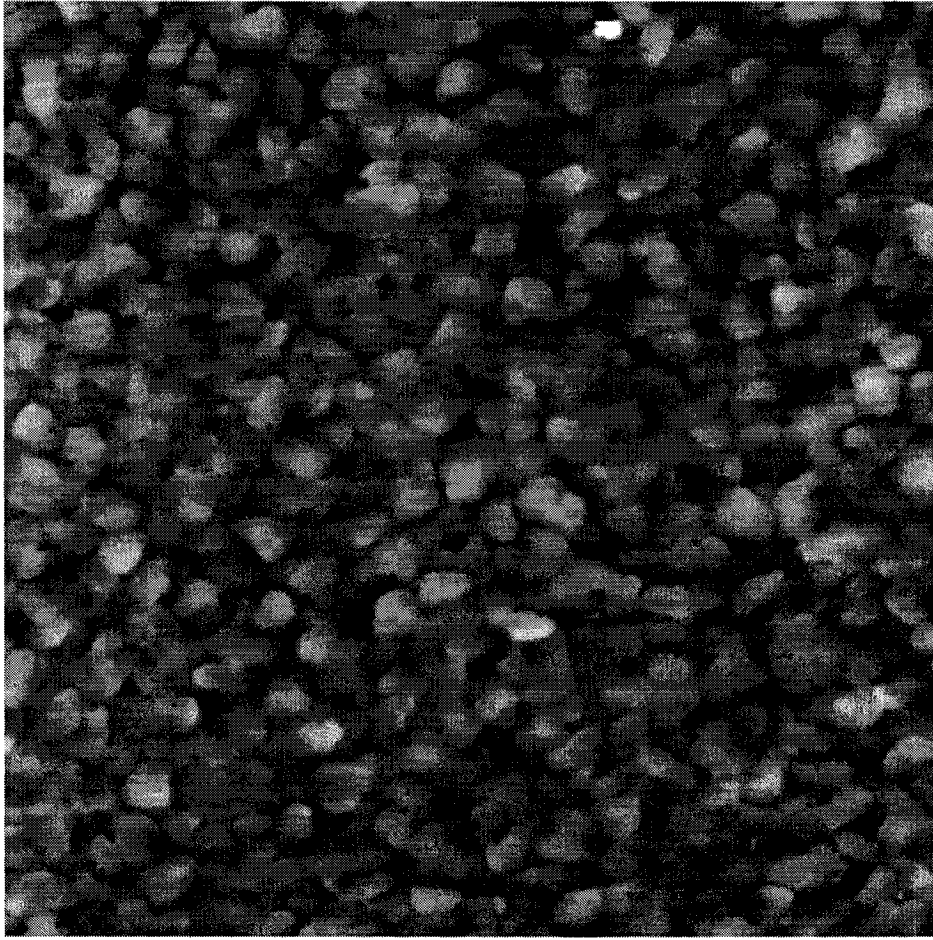


Figure 9: STM image ($3\mu\text{m} \times 3\mu\text{m}$) of the gold surface on the cantilever. Images were acquired in air with a tip bias of 600 mV and tunneling current of 35 pA. Height contrast scale is 14 nm.

Rectangular silicon microcantilevers were chosen for the WE for two principal reasons. Firstly, the rectangular shape makes for a simpler theoretical treatment [40] when converting the microcantilever deflection signal into a surface stress value. Secondly, the silicon surface of the microcantilever is reflective enough to allow the position-sensing laser light to reflect directly off it (opposite the metal-coated side where the potential is applied), as shown in Figure 6 and Figure 7. Hence, one does not need to reflect the laser light off the gold-coated side of the

microcantilever, as is the case for silicon nitride microcantilevers used in AFM and in many of the reported microcantilever-based surface stress experiments. This allows us to avoid artifacts in the deflection measurement resulting from changes in surface reflectivity that occur when applying a potential to a gold surface. A large change in the reflectivity can be expected due to electrochemical reactions, such as hydrogen or oxygen adsorption [93], and can contribute to an artificial microcantilever response if the detected signal is not independent of the laser intensity. This can also be of particular concern when studying conducting polymer films that change color as a function of the applied potential [126].

In many cases, knowledge of the working electrode area (i.e. the area of the microcantilever and chip immersed in the electrolyte) is of significant importance as it enables one to quantify the current density (amount of charge consumed per unit area) during an electrochemical reaction. In particular, to obtain a reproducible thickness of an electrochemically deposited polymer film (see section 5.1.2), it is important to control the surface area of the WE in contact with the electrolyte. Simply dipping the part of the microcantilever chip in the electrolyte solution makes it difficult to estimate the actual surface area in the solution due to the formation of a meniscus. A technique for delimiting the area of the WE in contact with the electrolyte was therefore implemented. The microcantilever chip was placed in an aluminium fixture, holding the chip securely in place while exposing an area on the microcantilever chip. This setup is shown schematically in Figure 10.

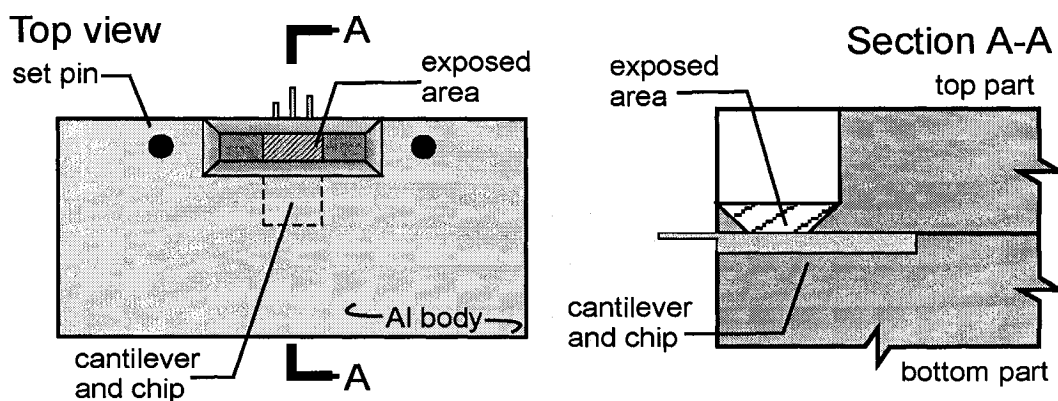


Figure 10: Schematic representation of the aluminum fixture used for the application of Apiezon wax to the gold-coated microcantilever chip. An area of the chip is exposed to the wax. The set pins allow for the precise positioning of the Al body on top of the microcantilever chip for a reproducibly exposed area. On the left is a top view of the assembly that shows how the chip is held while exposing a fixed surface area of 1.0 mm^2 at 0.7 mm from the base of the microcantilevers. On the right is a side view of the assembly.

A layer of Apiezon wax W , is then deposited on the exposed area of the microcantilever chip. The masked region gives an electrode area of 1.0 mm^2 . The precision of the electrode area measurement is hard to estimate and is mostly affected by the uncertainty in the adhesion between the wax and gold surface, at the masked region/gold surface boundary. The reproducibility of the electrochemically deposited PPy film thickness, found to better than 3% as shown in section 5.1.2, can give an appreciation for the uncertainty of the WE area. The Apiezon wax is partly dissolved in trichloroethylene (TCE) to facilitate its application. The solvent is then left to evaporate, leaving the wax to harden for a few minutes before using the microcantilever as an electrode. Other solvents such as chloroform and methanol were also tested but the best results were obtained

with TCE. Heating the wax was found to be inadequate as it would cool down and harden before being deposited. Note that we did not encounter any contamination issues (i.e. unusual peaks in the cyclic voltammetric data) with the presence of the wax in aqueous solution.

2.1.4 Deflection Sensing Scheme

The differential microcantilever-based sensor is operated in a static mode, where the microcantilevers deflections are monitored using an optical beam technique. A fiber-coupled laser diode [41] operating at a wavelength of 635 nm, mounted in an electrostatically shielded box and driven at constant current by a precision current source [42], is used as a light source. The laser light is fed into two singlemode optical fibers [43] by a 50/50 coupler [44]. The use of a single common light source effectively eliminates the effects of laser intensity noise on the differential measurement since both active and reference microcantilevers experience the same level of noise. The light is then focused onto the apex of each microcantilever using custom made commercial focusers [45] having a working distance of 25 mm with a measured (in air) spot size of 24.6 μm (measured at the maximum intensity/ e^2). Two micropositioners [46] are used to align the laser light on each cantilever. The laser spot positioning technique is shown schematically in Figure 11. This approach allows the laser spot to be reproducibly positioned at the same point of the cantilever, thus minimizing the error in the cantilever effective length and improving the precision in the deflection measurements (see section

3.1.2). The optical power hitting each microcantilever is set to less than 1 mW, to minimize heating of the microcantilevers.

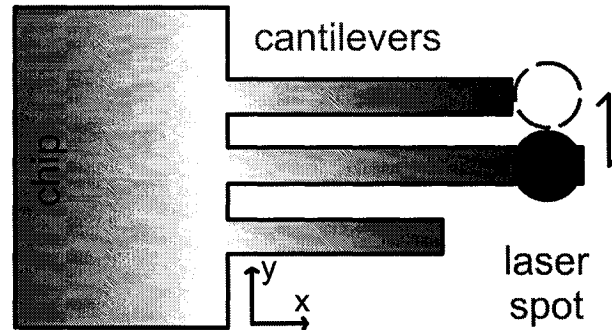


Figure 11: Positioning of the laser spot on the cantilever. The laser spot is reproducibly positioned at the same point on the length of the longest cantilever by aligning the laser spot with the second longest cantilever. The laser spot is aligned in the x-direction, over the edge of the second longest cantilever, by minimizing the PSD sum signal. The laser spot is then positioned on the longest cantilever, by moving it in the y-direction and maximizing the PSD sum signal.

The displacement of the reflected laser beams is monitored by two linear one-dimensional PSDs [47]. Each PSD is located 24 mm away from the microcantilevers. The photocurrents generated at the PSD terminals by the impinging light spot are converted into voltages, Y_1 and Y_2 , by a home built precision transimpedance amplifiers as shown in Figure 12. The output voltages are then processed by an analog dividing chip, giving a voltage, V_{pos} , which is directly proportional to the absolute position of the light spot (centroid) on the PSD,

$$S = 10 \cdot \frac{Y_2 - Y_1}{Y_2 + Y_1} = \frac{V_{pos}}{2} \quad \text{Equation 2-1}$$

Note that the intensity of the incident light spot does not affect the value of V_{pos} . In practice, however, a change in the spot intensity may induce an artificial change in V_{pos} because of a possible change in the overall diffused background intensity resulting from scattering at the microcantilever's edges and in the surrounding medium (i.e. the centroid shape). A 16-bit analog-to-digital converter (ADC) from National Instruments, card model # PCI-6035E, digitizes the signal which is finally stored on a computer interfaced with a LabView program.

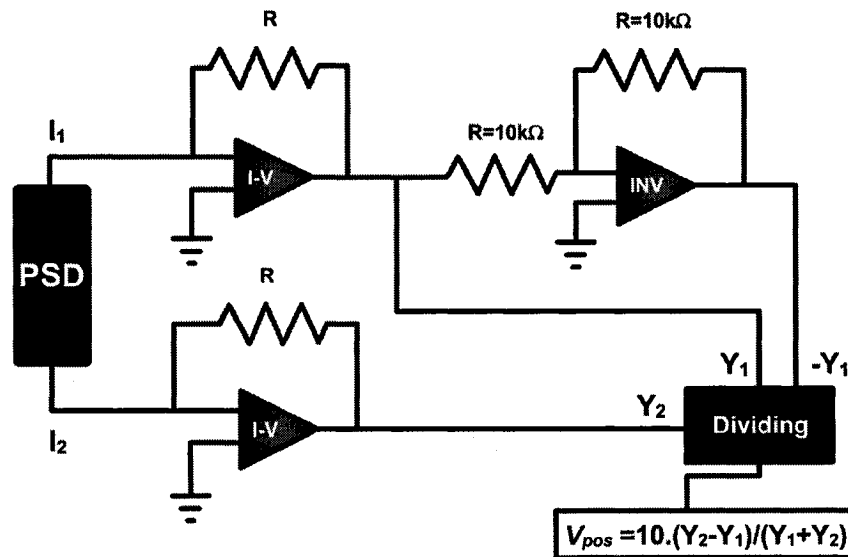


Figure 12: Schematic of the electronic circuit built to convert the PSD electrode photocurrents to a voltage proportional to the laser spot position on the PSD surface. The photocurrents, I_1 and I_2 are processed by current-to-voltage converters ($I-V$, [48]). The gain of the $I-V$ converter is determined by R , the feedback thin film resistor. The value of R can be selected between 100 k Ω , 220 k Ω , 470 k Ω , and 1 M Ω or a combination of these in parallel. The gain resistors, R , from the two electrodes were individually matched to 0.01% to ensure accurate deflection measurements. The Y_1 voltage is inverted by an inverting chip (INV , [49]). The signals Y_1 , Y_2 and $-Y_1$ are fed into a dividing chip [50], thereby producing a voltage directly proportional to the absolute position on the PSD.

2.2 Materials and methods for electrochemical experiments

All experiments are performed in the electrochemical cell described above. Prior to each experiment, the cell is rinsed three times with de-ionized water [51], followed by the electrolyte solution.

The surface stress measurements at the solid-liquid interface are performed on electrochemically cleaned gold surfaces. By sweeping the voltage from 0 to +1500 mV as shown in Figure 13, the gold surface is clean through gold oxide formation and removal.

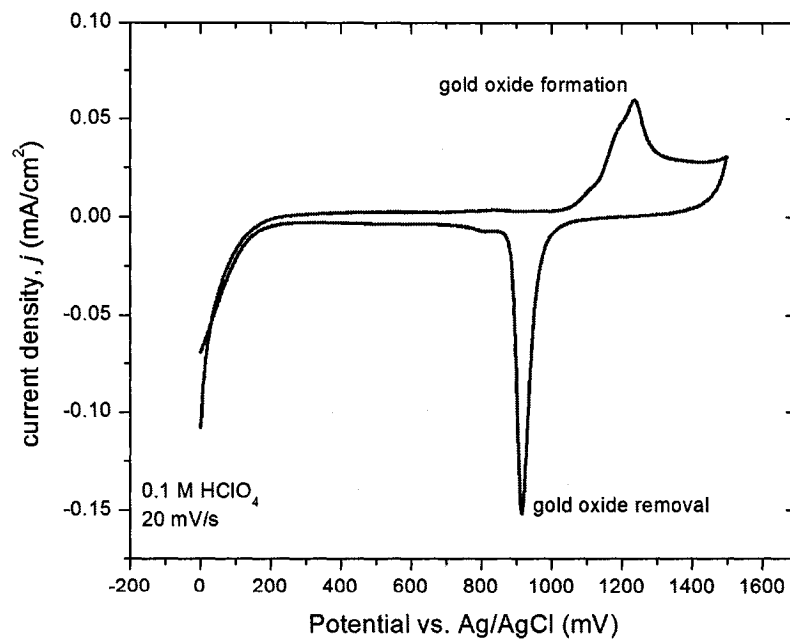


Figure 13: Cyclic voltammogram, recorded at a scan rate of 20 mV/s for a gold-coated cantilever in 0.1 M HClO₄ solution. The Au oxide formed at potential above 1100 mV is stripped off on the cathodic sweep (sharp peak at ~900 mV).

To demonstrate that the gold surface is clean and that electrochemical processes occurring on the microcantilever surface can be effectively detected, cyclic voltammetry (CV) is performed on the WE gold surface with the $\text{Fe}(\text{CN})_6^{3-/4-}$ redox couple. A peak separation of 71 mV (vs. Ag/AgCl) is observed (Figure 14). This value is acceptable compared to the theoretical peak separation of 59 mV. The discrepancy is probably due to the contact resistance. In addition the intensities of the cathodic and anodic peak are nearly equal which is indicative of a reversible process.

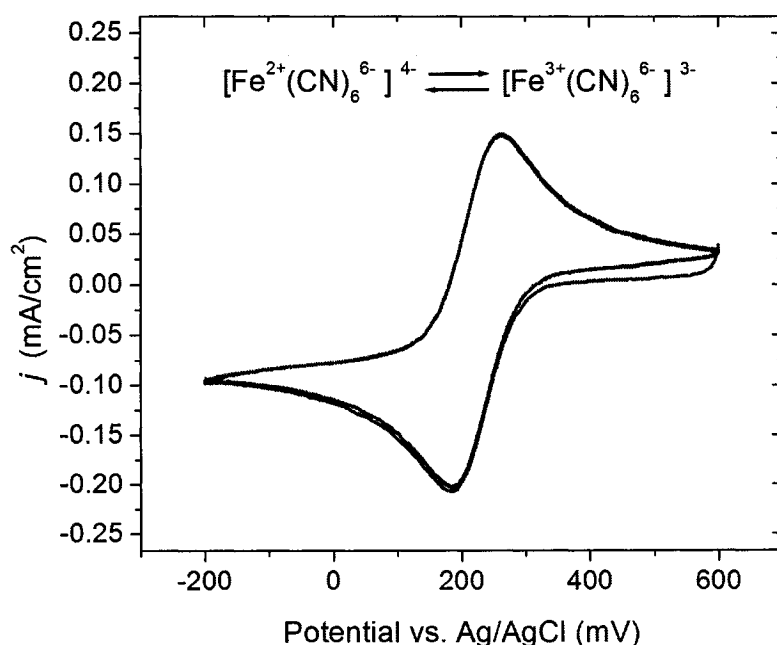


Figure 14: Cyclic voltammograms of a microcantilever's bare gold surface in an aqueous solution of 2mM $\text{K}_3\text{Fe}(\text{CN})_6$ and 0.2M KCl electrolyte. The one electron reduction and oxidation of $\text{Fe}(\text{CN})_6^{3-/4-}$ at the gold surface results in a cathodic peak at 187 mV and an anodic peak at 258 mV. The peak separation of 71 mV (which is close to the theoretical value of 59 mV), and equal cathodic and anodic peak current intensities are consistent with a reversible redox process.

For the experiments performed on conducting polymer actuators in Chapter 5, the pyrrole monomer liquid [52] is purified by passage through an alumina-filled column. The resulting liquid is clear and colorless in appearance, indicating that long pyrrole chains, from adventitious polymerization, are removed. The aqueous solution containing pyrrole and NaDBS [53] is protected from ambient light following its preparation to prevent polymerization of the monomer.

All other electrolyte solutions (except for the surfactant based solutions which produce foam) are purged for 1 hour with argon gas to remove oxygen contamination from the solution before use. During experiments a small positive pressure of argon is kept above the electrochemical cell.

3 Calibration

Calibrating the instrument is essential to achieve accurate, quantitative surface stress measurements. Foremost, the optical beam deflection technique needs to be calibrated in order to accurately translate the output voltage of the PSD, ΔS , into actual microcantilever deflection Δz . Subsequently, the microcantilever deflection must be converted into surface stress to allow comparison of experimental results obtained using different microcantilevers sensors and to test theoretical modeling aimed at understanding the origins of the measured surface stress.

It is common in the literature to see microcantilever results quoted in volts or in arbitrary units [54,55]. For practical sensing applications, requiring only a “yes” or a “no” output signal, this approach is often good enough. More often the results are quoted only in terms of cantilever deflections [22,30], without explicitly discussing the calibration procedure employed. In some cases the results are assigned a surface stress value, though using crude estimate of the conversion factor which can produce very large errors (>100%). It is therefore difficult to compare and interpret the origin of surface stress in most of the published work. In fact it is a non-trivial matter to accurately convert the acquired signal into surface stress, but it is compulsory if experimental results are to be matched up to

theoretical modeling. The methodologies developed to translate the PSD signal into an accurate surface stress value are described in this section.

3.1 Optical Beam Deflection Technique

For small deflections, the microcantilever deflection (Δz) is linearly proportional to the acquired PSD signal (ΔS).

$$\Delta z = C_{cal} \Delta S \text{ Equation 3-1}$$

Calibrating the optical beam deflection technique requires determining the value of C_{cal} . Two techniques were developed, an accurate methodology which requires the use of an interferometer [56] to simultaneously measure the cantilever deflection, and a simpler more rapid method based on geometrical arguments.

3.1.1 Interferometric Calibration

For accurate quantitative surface stress measurements the use of an interferometer, together with the optical beam deflection technique, to simultaneously measure the cantilever deflection, is recommended to obtain the value of C_{cal} in Equation 3-1.

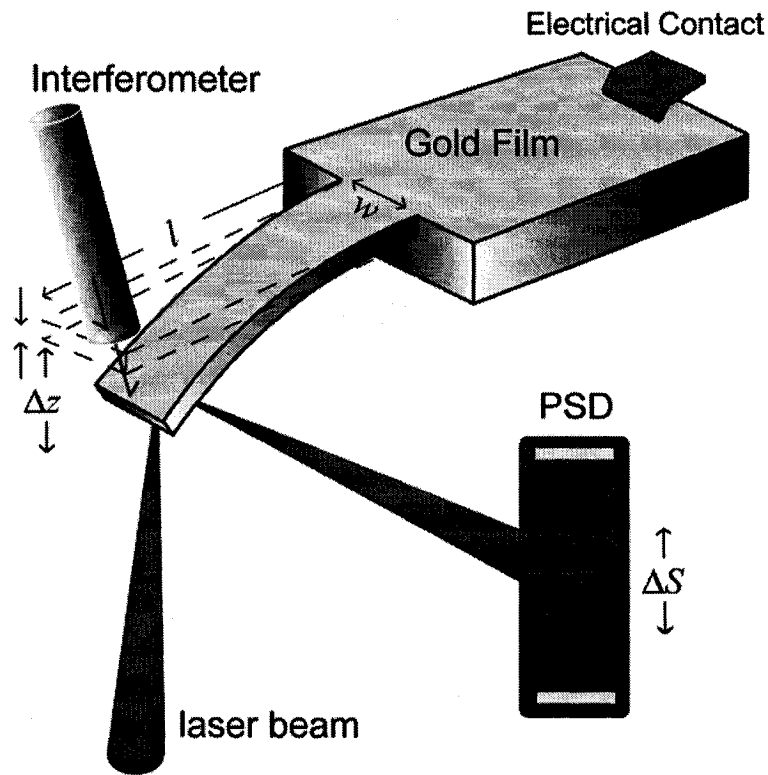


Figure 15: Schematic representation of simultaneous monitoring of the microcantilever deflection using the optical beam deflection technique on the Si backside and an interferometer on the opposite side.

In short, taking advantage of the bimetallic effect, a deflection is induced through heating by passing current in a $1.2 \text{ K}\Omega$ resistor mounted on the microcantilever chip. While cooling the PSD signal is acquired. Simultaneously, the deflection of the microcantilever is directly measured with a fiber-optic interferometer, which is positioned at the end of the microcantilever from the opposite side of the optical beam set-up. The interferometer signal consists of an interference pattern from which the microcantilever deflection (Δz) can be directly extracted through knowledge of the wavelength and the number of fringes travelled. Hence, the calibration constant comes to:

$$C_{cal} = \frac{K_{int}\lambda}{4\pi} \text{ Equation 3-2}$$

where, K_{int} is the frequency of the sinusoidal wave of interferometer signal as a function of the PSD signal, and λ is the laser wavelength.

For the instrument presented herein, I have found a value of $C_{cal-passive} = (3.42 \pm 0.07) \times 10^{-6}$ m/V and $C_{cal-active} = (3.21 \pm 0.06) \times 10^{-6}$ m/V for the passive and active cantilever respectively.

The implementation of this technique is described in M. Godin et al. Appl. Phys. Lett. 79, 551 (2001) as well as in greater detail in M. Godin PhD. Thesis [118]. Ultimately it can allow for the deflection measurements uncertainty to be kept under 2%.

3.1.2 Geometrical Calibration

The differential equation of the deflection curve of a cantilever beam can be written as follow [57,58]:

$$\frac{d^2z}{dy^2} \cong \frac{1}{R} = \frac{M}{E^*I} \text{ Equation 3-3}$$

where R is the radius of curvature; M the bending moment acting at the free end of the rectangular cantilever beam; E^* is the biaxial modulus, which is related to the Young's modulus E by $E^* = E/(1-\nu)$; I is the area moment of inertia. The first integration of Equation 3-3 produces the slope of the deflection curve at a position y along the cantilever length. For small deflections of the cantilever the small

angle approximation can be used to simplify the analysis. In which case the slope, dz/dy , and the deflection angle, θ , are equal:

$$\tan \theta \approx \theta = \frac{My}{E^*I} \text{ Equation 3-4}$$

The second integration of Equation 3-4 produces the deflection, δ , at position y along the cantilever length.

$$\delta = \frac{My^2}{2E^*I} \text{ Equation 3-5}$$

The area moment of inertia relative to the z axis can be calculated from [59]:

$$I = \int z^2 dA = \int_{-t/2}^{t/2} z^2 w dz = \frac{wt^3}{12} \text{ Equation 3-6}$$

where the differential element of area dA is taken in the form of a horizontal strip of width w and height dz , so that $dA=wdz$.

Therefore the maximum deflection angle θ_{\max} and the maximum deflection δ_{\max} (or Δz as we have previously labelled it), at the free end of the cantilever beam of length l , are:

$$\theta_{\max} = \frac{12Ml}{E^*wt^3} \text{ Equation 3-7}$$

$$\delta_{\max} = \frac{6Ml^2}{E^*wt^3} \text{ Equation 3-8}$$

Substituting Equation 3-8 into Equation 3-7 we obtain:

$$\theta_{\max} = \frac{2\delta_{\max}}{l} = \frac{2\Delta z}{l} \quad \text{Equation 3-9}$$

Equation 3-9 relates the deflection of the cantilever Δz to the deflection angle θ as depicted in Figure 16.

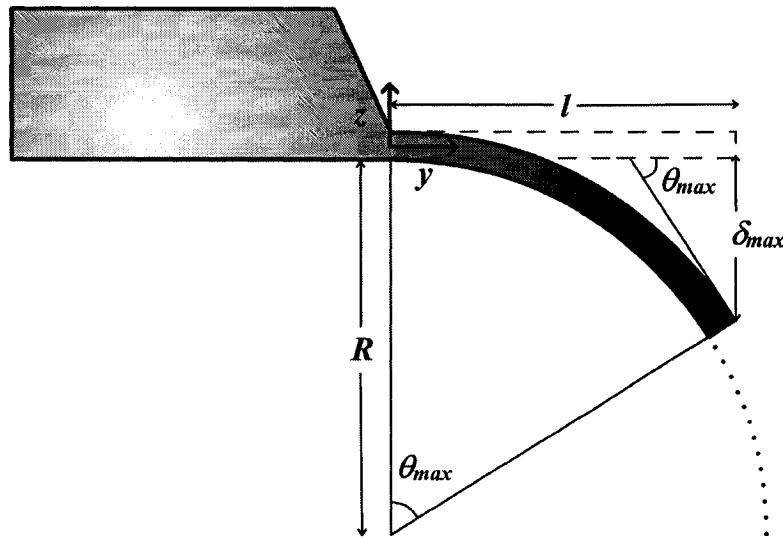


Figure 16: Schematic of cantilever bending when subjected to a bending moment. For small deflection δ , the radius of curvature R is assumed constant, so that the bending can be modelled by an arc.

Calibration of the optical beam involves correlating the displacement of the reflected laser beam on the PSD, ΔS , with the actual cantilever deflection, Δz .

From Figure 17 we can derive the following relationship:

$$\tan(2\theta_{\max}) \approx 2\theta_{\max} = \frac{\Delta S}{L} \quad \text{Equation 3-10}$$

where L is the distance between the cantilever and the PSD, and for small deflection $L \approx L \pm \Delta z$, since $L \gg \Delta z$.

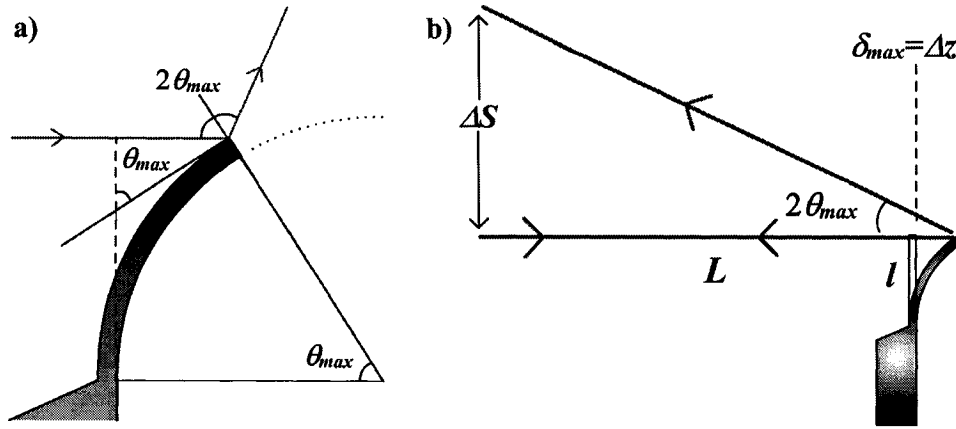


Figure 17: Schematic of optical beam deflection technique.

Substituting Equation 3-9 into Equation 3-10 we obtain the geometrical calibration formula:

$$\Delta z = \frac{l}{4L} \Delta S \quad \text{Equation 3-11}$$

To improve on the accuracy of this formula, l should be replaced by l_{eff} , the effective length of the cantilever. The microcantilever effective length is defined as the length at which the laser beam hits the microcantilever, $l_{eff} = 325 \pm 5 \mu\text{m}$. The level of precision in the effective length of the cantilever is achieved by the method depicted in Figure 11. For this particular system geometry with $L = 24 \pm 1 \text{ mm}$, a 6% percentage difference is found between the interferometer calibration constant and the geometrical calibration constant. A value of $C_{cal-geometric} = (3.4 \pm 0.2) \times 10^{-6} \text{ m/V}$ is found, for the system described herein.ⁱⁱⁱ

ⁱⁱⁱ By taking into account the fact that the response of the linear PSD, ΔS , has units of 10^{-3} m/V .

The major source of error in C_{cal} comes from the uncertainty in the measurements of the distance L . However, in the experimental set-up, L is fixed for all measurements, so that random errors in the experiments are associated with the determination of the effective length of the microcantilever, l_{eff} . (see Appendix)

Recently, our group have developed a working 3 dimensional model that accurately describes the way in which a position sensitive photodetector interprets the deflection of a cantilever [60]. This model exactly predicts the numerical relationship between the measured PSD signal and the actual cantilever deflection. In addition, the model is used to optimize the geometry of any laser deflection system which greatly simplifies the use of any cantilever-based instrument that uses a laser beam deflection system.

3.1.3 Index of Refraction

The value of the calibration factor C_{cal} derived up to now is only valid in the gas phase. When the cantilever is immersed in a liquid, the reflected laser path is modified according to Snell's law. Figure 18 represents the optical configuration of the experimental arrangement.

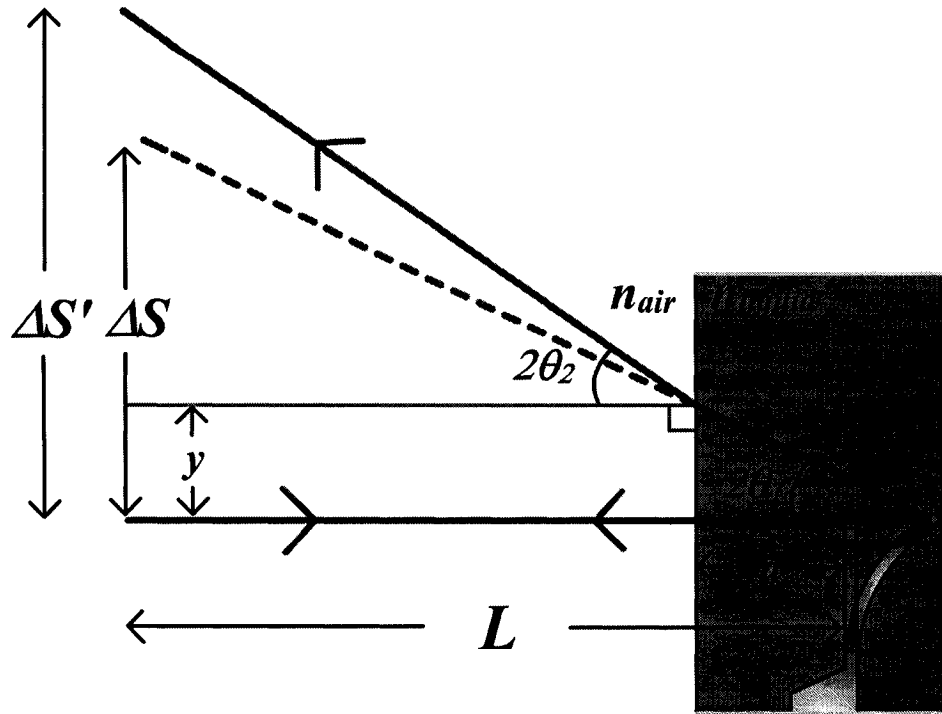


Figure 18: Schematic of the effect of the change of index of refraction on the PSD signal. $\Delta S'$ is measured whereas ΔS is needed to know cantilever deflection Δz .

The change in the index of refraction from liquid to air alters the deflection angle from θ_1 to θ_2 . The actual measured displacement of the laser spot on the PSD, $\Delta S'$, is therefore overestimated. $\Delta S'$ must be scaled back to ΔS in order for the cantilever deflection Δz to be accurately converted. According to Snell's law and from Figure 18 the following relationship can be established (see Appendix):

$$\Delta S = \frac{\Delta S'}{n_{liquid}} \cdot \frac{1}{\left(1 - \frac{d}{L} + \frac{d}{n_{liquid}L}\right)} \quad \text{Equation 3-12}$$

where n_{liquid} is the index of refraction of the electrolyte solution, d the distance between the optical window and the cantilever, and L the distance between the cantilever and PSD.

Therefore the values of C_{cal} previously found in air must be corrected by an amount proportional to the index of refraction of the electrolyte solution. For the optical beam arrangement of the instrument presented herein and taking the index of refraction of water we obtain:

$$\Delta S = \frac{\Delta S'}{1.24} \text{ Equation 3-13}$$

The value of C_{cal} corrected for the effect of refraction at the optical window by Equation 3-12 is valid as long as the cantilever to PSD length is not modified. However, the PSD can be required to move if for example an experiment is performed in a liquid with an index of refraction which alters the laser path to an extent where the reflected laser spot no longer impinges on the PSD.

The change in index of refraction effect could in principle be taken into account by the interferometric calibration technique if it was practical to perform the calibration technique in liquids.

3.2 Quantifying Surface Stress

The bending moment M acting on the cantilever can be written as follow [58,59]:

$$M = \frac{wt}{2} \Delta\sigma \text{ Equation 3-14}$$

Replacing Equation 3-14 into Equation 3-8 we obtain the so-called Stoney's formula [61]:

$$\Delta\sigma = \frac{Et^2}{3(1-\nu)l^2} \Delta z \text{ Equation 3-15}$$

Using the equation of the spring constant of a rectangular cantilever [57]:

$$k = \frac{Ewt^3}{4l^3} \text{ Equation 3-16}$$

we get an equation for the surface stress which is directly proportional to the microcantilever deflection, and contains only measurable parameters [56]:

$$\Delta\sigma = \frac{4}{3(1-\nu)} \cdot \frac{l}{wt} k_{rect} \Delta z \text{ Equation 3-17}$$

where ν , l , w , t and k_{rect} are the Poisson's ratio, length, width, thickness and spring constant the microcantilever, respectively. The $4/3$ factor takes into account the difference in the cantilever beam curvature resulting from a uniform surface stress, as opposed to a concentrated load applied at the tip. The microcantilever geometrical properties are all measurable parameters. A high resolution SEM was used to accurately determine each dimension to improve the accuracy of the surface stress measurements. Poisson's ratio is taken to be 0.064 [62], because the

single crystal Si microcantilever surface is in the $\{100\}$ plane and the microcantilever edges are along the $\langle 110 \rangle$ direction. The spring constant was obtained using Sader's method [40], which simply requires the measurements of the microcantilever length, width, and its fundamental resonant frequency and corresponding quality factor. A FFT network analyser [63] was used to acquire the power spectrum density of the microcantilever deflection signal.

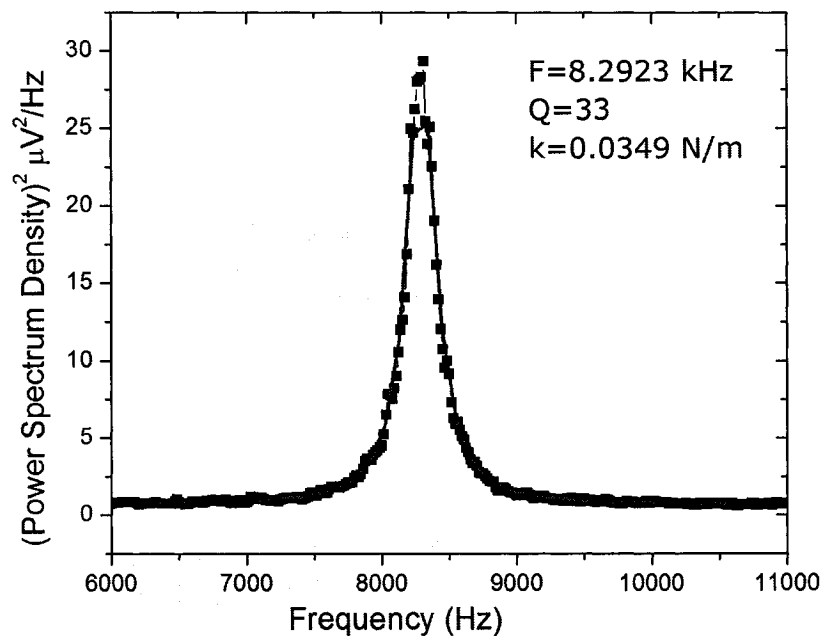


Figure 19: Power spectrum density versus frequency of a typical cantilever. The data is fitted to a Lorentzian (in red) from which the resonance frequency and Q-factor are extracted.

The consequences of the microcantilever gold coating ($t_{Au} = 100$ nm) on the mechanical properties of the microcantilever beam are taken into account by the measurements of the microcantilever beam thickness and of its spring constant. Its

effect on Poisson's ratio is assumed negligible in this case. Because the deflection of the apex of the cantilever is required in Equation 3-17, the Δz measured at the effective length of the cantilever by Equation 3-11 is corrected by a factor of $(L/l_{eff})^2$ [56].

By carefully determining the value of each parameter in Equation 3-17 we can measure surface stress values with an accuracy of 10% (see Appendix). The precision with which the spring constant, k_{rect} , and the thickness, t , can be measured are the major contributions of error in surface stress measurements, followed by the uncertainty in L . The advantages of using Equation 3-17 over Stoney's formula (Equation 3-15) is that it is not necessary to know the Young's modulus, E , of the microcantilever structure.

Equation 3-17 refers to a relative change in surface stress between both sides of the microcantilever. Therefore, for this microcantilever-based sensor technique to work, one side of the microcantilever must remain inert and non-reactive throughout the experiment. In such a case, the studied phenomenon only occurs on one side of the microcantilever and changes in surface stress measurements are obtained. Otherwise, competing reactions from both sides of the microcantilever may lead to results that are difficult to interpret. Methods for passivating the backside of microcantilevers often present a difficult challenge and are the subject of ongoing research (see section 1.1.2).

3.3 Instrument Sensitivity and Resolution

Our device can achieve a deflection sensitivity of 0.2 nm, in a 0-3 Hz bandwidth, by performing time-averaging on the acquired deflection signal, resulting in an ultimate surface stress sensitivity of 1×10^{-4} N/m. The surface stress sensitivity was calculated for the specific microcantilevers used here but can be improved with a lower spring constant (longer, thinner and narrower microcantilevers). The maximum detectable deflection signal of our PSD corresponds to a surface stress of 50 N/m, providing us with a dynamic range of 5×10^5 . The maximum surface stress value was calculated for the specific geometry of the experimental setup and is limited by the finite size of the PSD. In fact, as described by Equation 3-11, the dynamic range can be lowered or amplified by respectively increasing or reducing L , at the cost of inversely affecting the sensitivity of the instrument.

To perform accurate differential microcantilever-based sensor measurements, both active and reference microcantilever deflection signals should be converted into surface stress before the signals are subtracted. Indeed many parameters affect the magnitude of the deflection signals. Overall, in the system described herein, since both microcantilever-based sensors have almost identical L , it is the difference in spring constants between the active and reference microcantilevers that mainly affects the difference in magnitude of the deflection signals. In fact, from Equation 3-16 any small variations in the thickness or length of the microcantilever result in a significant change in the value of the spring constant. The microfabrication process involved in making single crystal silicon

microcantilevers inherently produces variation from chip to chip in the thickness of the beams. Differences in the spring constant of up to one order of magnitude have been observed for the microcantilevers used. It is therefore imperative to measure the spring constant of both active and reference microcantilevers independently, and transform the active and reference microcantilever deflection signals into surface stress to obtain a proper differential signal.

3.4 *Testing of the Instrument*

To ensure the instrument is properly calibrated and that the methodology presented above is valid, I have subjected the instrument to a set of control experiments and compared the measurements obtained to previously published results.

3.4.1 Validation of the Calibration

To verify the accuracy of the instrument, I have compared the surface stress induced during anion adsorption on gold obtained by the calibrated instrument presented herein with results obtain by Ibach et al. on a single crystal Au(111) surface using an electrochemical STM.

Electrochemical cycling between 0 to 700 mV (vs. Ag/AgCl), in a 0.1 M perchloric acid solution (HClO₄) at 20 mV/s, causes weak adsorption of ClO₄⁻

anions on the gold-coated surface of the microcantilever. In turn, the weak anion adsorption induces a surface stress change on the microcantilever (WE). A compressive surface stress of -0.58 ± 0.06 N/m is measured when the WE potential is changed from 0 mV to +700 mV, in excellent agreement with previously reported value by Ibach et al. [104]^{iv} (including a correction factor of 0.8260 which was later calculated using finite element analysis [64], because of the particular geometry of the clamped beam he used). Within this potential window the Au(111) surface stays in an unreconstructed state and the surface stress measured is entirely due to the charging of the double layer by the ClO_4^- adsorbate ions [104].

^{iv} The cantilever has a rectangular shape of 6 mm x 3 mm clamped at one end. In order to ensure that changes in the surface stress would occur only on one side, the lower face of the sample was covered with nail polish. The change in the vertical position of the sample is measured by the STM tip, which is at a distance $l = 4$ mm away from the edge where the crystal is clamped. Prior to the measurements, the Au single crystals were annealed at 800°C for 2 h in an oxygen atmosphere and for 1 h in an argon atmosphere. Afterwards, the crystals were allowed to cool in an argon atmosphere.

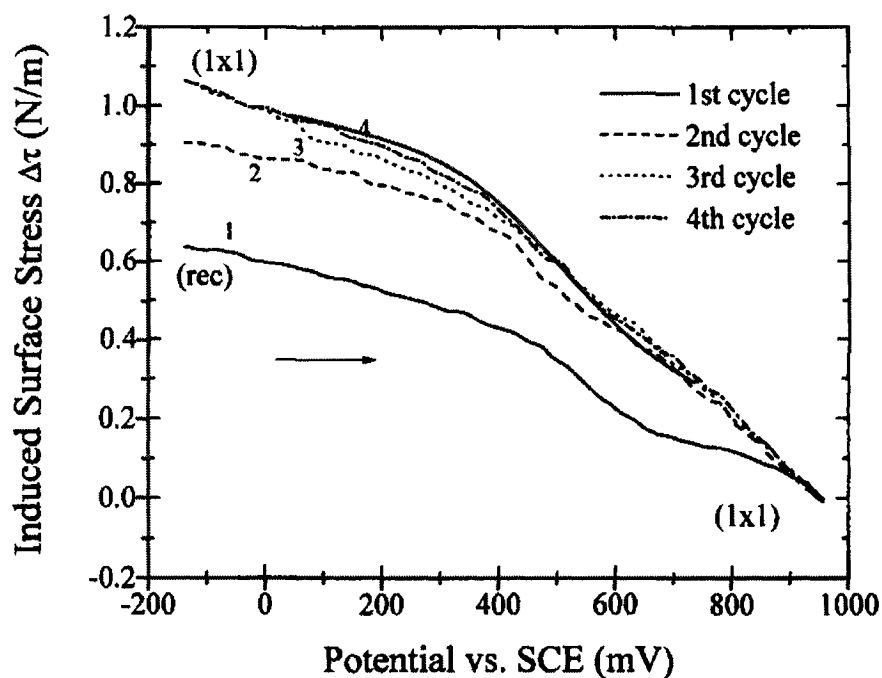


Figure 20: In back is the surface stress response [Data reproduced from Ibach et al. *Surface Science* 375, 107-119 (1997), reference 104] during ClO_4^- adsorption on Au(111). Effect of the reconstruction of the surface is visible on curve 1. However, on the subsequent cycling, curve 2-4, the surface remains in an unreconstructed state. Surface stress measurement obtained using the calibrated instrument presented herein and corrected for the missing correction factor in Ibach's original results is superimposed in red. Our data was shifted by -35 mV to convert the potential axis from 3 M Ag/AgCl to SCE.

Figure 20 is a reproduction of the surface stress data obtained by Ibach et al. superimposed with the induced surface stress acquired with the calibrated instrument presented herein. The data obtained is corrected to reflect the correction factor missing in Ibach's data. The overlap is striking and it clearly validates the calibration of the instrument.

It is nevertheless surprising that the result obtained on polycrystalline gold-coated microcantilevers matches the reported value on single crystal surfaces. Indeed,

parameters such as crystallographic orientation, grain size, film roughness or grain boundary are presumed to influence the induced surface stress. This issue is addressed in section 4.5.

Figure 20 also clearly demonstrates the passivity of the microcantilever silicon [65] backside during electrochemically-induced surface stress on the gold-coated side. Changes in the surface stress of the backside, if any, are deemed insignificant, since the two curves in Figure 20 superimpose exceptionally well. Therefore, the silicon backside remains passive while a surface stress is electrochemically generated on the gold-coated side, so that for this particular experiment no further treatment is required to passivate the silicon back surface. Nevertheless, for future applications, it may be necessary to perform differential measurements to reveal the specific electrochemical response from the gold side.

3.4.2 Differential Mode

The high sensitivity of the microcantilever-based surface stress sensors makes them extremely responsive to physical and chemical stimuli. For example, during an experiment, an *active* microcantilever will deflect as a result of the electrochemical reaction occurring on its surface, but it will also deflect due to other factors. These *parasitic* microcantilever deflections occur as a result of several effects such as temperature changes (bimetallic effect), turbulent flow around the microcantilever, environmental noise, or uncontrolled chemical reactions on the back side (opposite the sensing surface) of the microcantilever. It

is therefore imperative that such deflections be removed from the final measurements if the surface stress data are to be analyzed correctly. A *reference* microcantilever can be tailored to only be reactive to these parasitic stimuli and serve as an effective reference sensor. A subtraction of a reference signal from an active microcantilever signal will give a measurement of surface stress that is purely due to the electrochemical reaction in question [22,23,66,67].

In order to illustrate the effectiveness of the differential microcantilever-based sensor, an experiment was conducted in which both the reference and active microcantilever deflections were simultaneously monitored. Electrochemical cycling between 0 to +700 mV (vs. Ag/AgCl) of the gold-coated surface of the active microcantilever, in a 0.1 M perchloric acid solution (HClO₄) is performed. While the electrochemical reaction is carried out on the active microcantilever (WE), the electrolyte solution temperature is varied, with the use of thermoelectric element [68] in contact with the back of the cell. For the purpose of subtracting thermal fluctuations and/or environmental noises (such as mechanical vibrations) from the active microcantilever (WE) signal, the reference microcantilever is identically covered with a Ti and Au film to make it equally sensitive to temperature variations through the bimetallic effect. No electrical contact is made to the reference microcantilever.

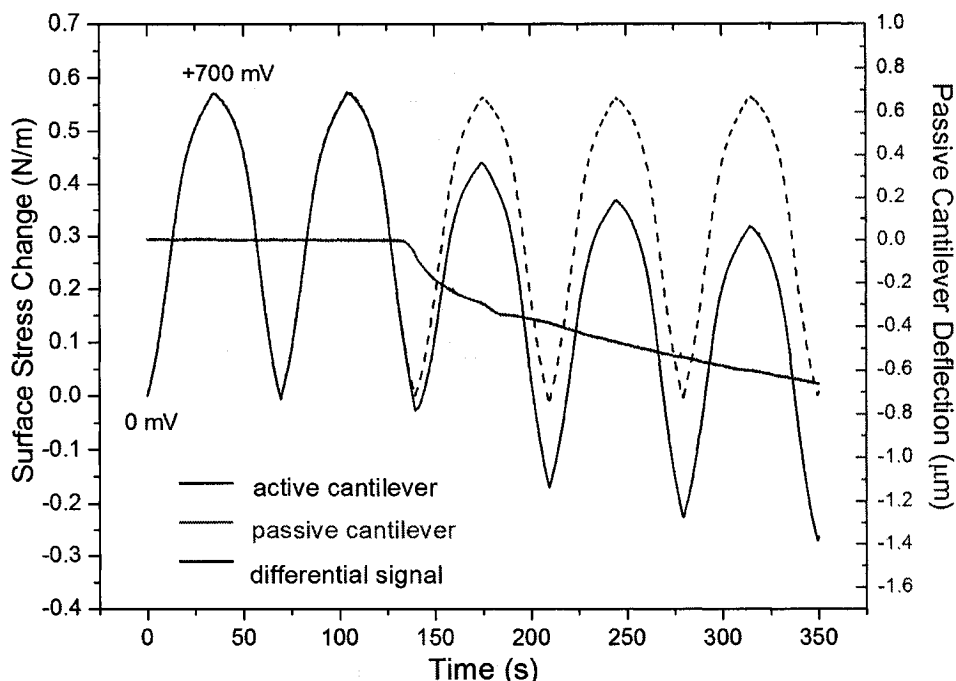


Figure 21: Active microcantilever (WE) signal, in black, during five cycles between 0 mV and +700 mV, and reference microcantilever signal, in red. At $t=130$ sec heat is induced and the reference microcantilever starts to drift. In the active microcantilever (WE) signal, sign of bending due to the bimetallic effect are also present. The reference microcantilever signal is subtracted from the active microcantilever signal. The resulting differential signal, in blue, shows no apparent sign of temperature variations.

Figure 21 shows the active microcantilever (WE) signal during five cycles of ClO_4^- anion weak adsorption on gold along with the reference microcantilever signal. Because no potential is applied to the reference microcantilever, no adsorption and no potential-induced surface stress takes place. At $t=130$ sec, the thermoelectric element starts to heat the electrolyte solution, as shown by the onset of the reference microcantilever deflection. While the electrochemical

reaction continues on the active microcantilever (WE) surface, sign of bending due to the bimetallic effect are also present. Figure 21 shows the differential microcantilever signal, where the reference microcantilever surface stress signal is subtracted from the active microcantilever (WE) surface stress signal. It is important to convert each individual cantilever deflection signal into a surface stress before subtracting them, as the spring constant from one cantilever to the next can be significantly different.^v It is clear from Figure 21 that the reference microcantilever acts like an effective reference sensor, and that temperature fluctuations can be properly eliminated (on the scale of the active microcantilever signal) from the active microcantilever (WE) signal.

Note that although the instrument presented herein is capable of differential measurements, most of the results reported in this thesis are single cantilever experiments. Indeed the focus of this present study is to investigate the surface stress response at the solid-liquid interface owing to all potential interactions occurring on the gold-coated surface during ionic adsorption. In addition, the large volume of the cell acts as a thermal bath so that typically for the duration of experiments the thermal fluctuations are negligible. Moreover, the passivity of the silicon backside to electrochemical processes induced on the gold-coated side is confirmed as observed in Figure 20. Therefore, the response of a single cantilever sensor is induced by a surface stress change on the gold side only.

^v In fact variation of up to one order of magnitude in the spring constant has been observed with the commercial MikroMasch type CSC12/without Al/tipless cantilevers.

4 Surface stress at the solid-liquid interface

In the past several decades, research in the field of surface science has been largely devoted to gain a deeper understanding of the structure of surfaces at the atomic scale. The advent of scanning probe microscopy techniques has been an important driving force in this now flourishing area of science. Recently, it has been recognized that surface stress, although being a macroscopic quantity, is important for the description and understanding of processes at the microscopic level. Recent studies have exposed the role of surface stress in some surface reconstruction, epitaxial growth, interfacial mixing, and self-organization phenomena [7,69,70,71,101,102,104, 112,113].

The bending beam method is generally used to measure changes in surface stress. A difference in surface stress between the two sides of the beam is determined by measuring the beam's curvature. However, if the initial surface stress of one surface is not known, this technique only gives relative changes in surface stress. The determination of absolute surface stress remains a challenge but can be evaluated in some cases. In fact, measurements of the lattice contraction of nanoparticles by electron diffraction have led to its absolute determination [72,73,74,75].

In electrochemistry, the bending of a beam has been used to investigate the electrode-solution interface and to study stress evolution in electrodeposited thin films [76,77]. A very attractive feature of studying surfaces in an electrochemical environment is that the surface stress change can be controlled by varying the electrode potential. The issue of surface stress has a long history in electrochemistry. Early experiments were performed on liquid mercury electrodes and were given the name of electrocapillary curves^{vi} [78,79]. The thermodynamics of electrochemical interfaces for liquid electrodes has been well understood for over 50 years [79]. However, its extension to solid electrodes has not been straightforward [80] primarily because of the debate as to whether the difference between surface energy and surface stress is of second order and hence negligible (see section 4.1.2) [81,99]. In fact, it is only recently that some form of consensus^{vii} has been reached in the electrochemical community with the publication in 1998 of a series of papers by Lipkowski et al. [100], Schmickler et al. [103] and Guidelli [88].

In this chapter, the relevant physical quantities related to this work will be defined and discussed. In Section 4.1 the concepts of surface stress and surface energy are presented and the debate on the difference between these two thermodynamic parameters is described. It is followed by a description of the solid-liquid

^{vi} The name is derived from the early measurements of this sort by Lippmann, who invented a device called a capillary electrometer. G. Lippmann *Compt. Rend.* 76, (1873) 1407

^{vii} A publication in 2005 by V.A. Marichev (*Surface Science Reports* 56 (2005) 277–324) continues to discuss certain thermodynamic problems of solid electrodes.

interface. Section 4.2 and 4.3 present experimental measurements of the surface energy and surface stress of gold-coated microcantilevers in perchloric acid. The effect of specific adsorption along with a simple qualitative model of the origin of the surface stress is discussed in section 4.4. Finally, in section 4.5 the effect of the sensing surface morphology on the surface stress response is considered.

4.1 Thermodynamic of the solid-liquid interface

4.1.1 Definitions

There are two fundamental thermodynamic parameters that characterize a surface: the surface free energy and the surface stress.

The reversible work per unit area (dw/dA) involved in forming a surface, for example by plastic deformation or cleavage, is the surface free energy, γ , which is a scalar quantity.

$$dw = \gamma dA \text{ Equation 4-1}$$

During plastic deformation of a surface, in the case of an expansion, atoms from the bulk move to the surface to maintain the equilibrium interatomic spacing. The surface free energy is a measure of the energy required to bring an atom from the interior of the bulk to the surface, i.e. a measure of the potential energy difference between bulk and surface atoms. The surface free energy must always be positive,

since otherwise a solid would gain energy upon fragmentation and would be unstable [82].

On the other hand, the surface stress, σ_{ij} , is a tensor representing the reversible work per unit area to elastically stretch a pre-existing surface. This process alters the density of atoms at the surface.

$$dw = A\sigma_{ij}d\varepsilon_{ij} \text{ Equation 4-2}$$

where the change in surface area, dA , is written in terms of $d\varepsilon$ the change in surface strain ($d\varepsilon = dA/A$). The relationship between the surface stress and the surface free energy is then described by the Shuttleworth equation [83,84,85] (see the appendix for full derivation):

$$\sigma_{ij} = \gamma\delta_{ij} + \frac{\partial\gamma}{\partial\varepsilon_{ij}} \text{ Equation 4-3}$$

where ε_{ij} is the surface strain tensor and δ_{ij} is the Kronecker delta. In most cases of interest the surface stress tensor can take on a simple form. By an appropriate choice of the coordinate system, the off-diagonal components can be set to zero. Additionally, surfaces possessing a 3-fold (e.g. the (111) surface of a face centered cubic, fcc, crystal) or higher symmetry (e.g. the four fold symmetry of the fcc (100) plane) the surface stress is isotropic and can assume a scalar form,^{viii} σ .

^{viii} Because $\sigma_{zz}=0$ and $\sigma_{xx} = \sigma_{yy}$.

By definition, a compressive (tensile) surface stress causes an expansion (contraction) of the stressed surface and bends the cantilever away from (toward) the stressed surface. It is assigned a negative (positive) sign.

A) Compressive surface stress B) Tensile surface stress

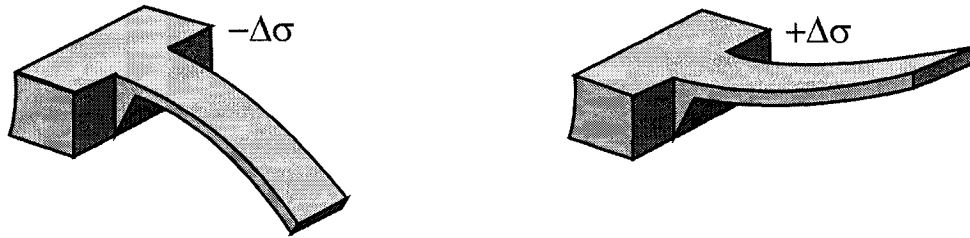


Figure 22: Convention for the sign of the surface stress. The stressed surface is the top surface and is represented in yellow. A) A compressive surface stress is assigned a negative value and bends the cantilever, depicted in the figure, downwards. B) A tensile surface stress is assigned a positive value and bends the cantilever, depicted in the figure, upwards.

For a liquid surface, the surface energy and the surface stress are equal since there is no resistance to plastic deformation because of the free movement of molecules to the surface, which means that the surface free energy does not change when the surface is strained. It is because of this equality for liquid surfaces that the surface energy and surface stress are sometimes referred to as surface tension, a term we will omit to avoid confusion.

The Gibbs adsorption equation (or the Gibbs-Duhem equation) for the interface at constant temperature, first obtained by Couchman and Davidson [86], is:

$$d\gamma = -qdE + 2(\sigma - \gamma)d\varepsilon - \Gamma_k d\mu_k \quad \text{Equation 4-4}$$

where q is the charge density on the metal electrode, E denotes the electrode potential, μ_k denotes the chemical potential of the species k in the electrolyte and Γ_k denotes the surface excess of the species k . The charge density q can be associated with the experimentally measured charge only when no charge transfer with the electrode takes place. This equation holds for ideally polarized electrodes, where the interface can be modeled by a double plate capacitor. Differentiating Equation 4-4 with respect to potential, E , and keeping the temperature and the chemical potential constant we obtain the generalized Lippmann equation:

$$\left(\frac{\partial\gamma}{\partial E}\right)_{T,\mu_k} = -q + 2(\sigma - \gamma)\left(\frac{\partial\varepsilon}{\partial E}\right)_{T,\mu_k} \quad \text{Equation 4-5}$$

For liquids, the second term on the right hand side vanishes, since $\sigma = \gamma$. For solids, the average electrostrictive term ($\Delta\varepsilon/\Delta E$) can be experimentally estimated, and as previously argued by Couchman and Davidson [86], is found to be a second order effect which can thus be neglected. Therefore for practical purposes, both liquid and solid electrodes obey the same Lippmann equation. Hence the surface energy (γ) can be obtained in the same way as liquid electrodes by measuring the variation of charge (q) with potential (E) at constant composition of the solution [100].

In the case of constant interfacial capacity, C , the surface energy (γ) is calculated from Equation 4-5 by replacing dE by dq/C , and is then equal to $q^2/2C$ or $CE^2/2$. The surface energy γ is therefore quadratic in q or E , and the electrocapillary

curve is parabolic with a maximum at the potential of zero charge (PZC). In contrast, the surface stress σ need not have an extremum at this potential. Detailed discussions on the thermodynamics of solid electrodes are reviewed in reference [100,87, 88].

4.1.2 Debate on the thermodynamics of solid electrodes

The development of microcantilever sensors to precisely measure surface stress changes at the solid-liquid interface in the late 90's, revived the debate about the difference between surface energy and surface stress and initiated a series of publications to clarify the current knowledge on the thermodynamics of solid electrodes [88,100,101,103,105,113]. To date, underpotential metal deposition [89,90,91] electrocapillary-type effects [90,91,92,93,94,95], doping/dedoping of a conducting polymer film [96,97] and redox reactions at a monomolecular organic film interface [98] have been investigated by employing an AFM cantilever as a surface stress sensor during electrochemical processes.^{ix}

Unfortunately, most electrochemical microcantilever sensor results are rather in contradiction to more recent surface stress results using other bending beam techniques. Some authors, using microcantilever-based sensors, reported a parabolic dependence of the surface stress on the potential. Motivated by a publication by Mohilner and Beck [99] which regarded surface stress and surface

^{ix} Most of these articles were published in between 1995-1997 before the publication in 1998 by Lipkowski et al. [100] which clarifies the current knowledge on the thermodynamics of solid electrodes.

energy as being approximately equal, the surface stress data were analyzed [90,91,92] as surface energy electrocapillary curves and the authors attributed the position of the maximum of the surface stress as the potential of zero charge (PZC). However, this interpretation was later shown to be erroneous both experimentally and theoretically [88,100,101,102,103]. In fact, for clean solid metal electrodes the surface stress cannot be approximated by the surface energy as it is the case of liquid electrodes (i.e. mercury).^x

The more recent surface stress results reported by Ibach et al. [104] and Haiss et al. [105] have a qualitatively different surface stress response at the solid-liquid interface than microcantilever-based sensors. These results on macroscopic Au (111) electrodes show a monotonic (i.e. no maximum) surface stress change as a function of potential as opposed to the parabolic shape which was observed on microcantilevers. These independent sets of results by Ibach et al. and Haiss et al., on well-defined Au(111) surfaces using an STM tip to measure the deflection (see page 49), yielded good although not quantitative agreement with one another. Inaccuracies in the conversion of the cantilever deflection into a surface stress are most probably responsible for their difference in magnitude. Nevertheless, these instruments have the ability to pre-treat the electrode surface by flame-annealing, to produce atomically flat single crystal surfaces or to use bulk metal electrodes. On the other hand, a microcantilever surface is made up of a polycrystalline evaporated thin film. This raises the possibility that the substrate morphology influences the surface stress response and thus explains the inconsistencies with

^x This fundamental point sometimes continues to be overlooked, as in reference 95 published in 2004.

the microcantilever results [102]. It remains to be shown if a microcantilever-based surface stress sensor can reproduce these macroscopic electrodes results both qualitatively and quantitatively.

This discrepancy in the results underlines the fact that up to now, the role played by the morphology of the sensing substrate in microcantilever surface stress sensors has been undervalued. In a recent study, work performed in our group has clearly shown that the substrate morphology plays a vital role in the response of microcantilever-based chemical sensors [106,118]. Parameters such as adhesion (i.e. adequately transferring the surface stress in the sensing film to the substrate), surface morphology (grain size, roughness, crystallographic orientation) and cleanliness (e.g. presence of contaminants, sulfur, oxides or adsorb hydrocarbons, on the metal surface) of the metal film can have both qualitative and quantitative effects on the measured surface stress. It is therefore essential to characterize and study these effects on the sensor response if microcantilever sensors are to become a useful technology.

4.1.3 Model of the double layer structure

Before presenting experimental results on gold-coated microcantilevers, a brief description of the solid-liquid interface is provided and some of the terms which characterize the interface are defined.

For potentials positive (negative) of the PZC (Potential of Zero Charge), the metal surface carries a net positive (negative) charge. The electric field, caused by these surface charges, attracts anions (cations) and their solvation shells to the metal surface. The layer of surface charges and counter ions is called the “electrical double layer”. Different models for the double layer structure exist with various degrees of refinement. The Stern layer model depicted in Figure 23 is a good model for the structure of many metallic surfaces in an aqueous medium. It combines the ideas of Helmholtz (counter-ions in contact with the surface) and that of a diffuse layer. The solvated counter-ions cannot approach closer to the metal surface than the length of a few water molecules, including those in their solvation shells. This gap is known as the outer Helmholtz layer (OHP). When specific adsorption^{xi} takes place the ions lose their solvation shell and bind to the gold surface. They determine the inner Helmholtz plane (IHP).

^{xi} The reference to specific and non-specific adsorption should not be confused with specific and non-specific adsorption of the sensing layer described in Chapter 1 which refers to the specificity of the selective chemical sensing layer. Here specific and non-specific refers to the strength of the interaction between the ions and the surface.

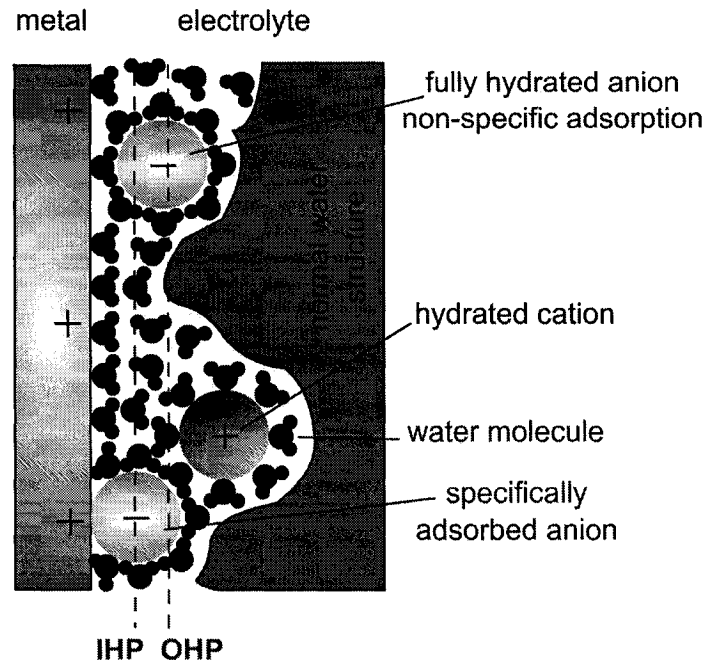


Figure 23: Stern picture of a positively charged metal/electrolyte interface. The inner (IHP) and the outer (OHP) Helmholtz planes are indicated. The double layer is divided into two parts: an inner part between the metal surface and the OHP called the Stern layer, and an outer part extending from the OHP into the bulk of the solution called the Gouy-Chapman or diffuse layer. In the first layer the bound water molecules have a distinct preferential orientation and thus a strongly reduced permittivity (typically $\epsilon \approx 6$). In the second layer of water it is of the order of $\epsilon \approx 32$. In the bulk water the permittivity is close to 80.

In the Stern picture described in Figure 23, the total capacitance per unit area is composed of the capacitors of the inner Stern layer (C_{St} , the inner part between the metal surface and the OHP) and the diffuse Gouy-Chapman layer (C_{GC} , the outer part extending from the OHP into the bulk of the solution) in series. The capacity of the interface can be written as:

$$\frac{1}{C^A} = \frac{1}{C_{St}^A} + \frac{1}{C_{GC}^A} \quad \text{Equation 4-6}$$

The capacity of the Stern layer can be estimated by $C_{St}^A = \epsilon_{St} \epsilon_0 / d$, where d is the radius of the hydrated ions for the inner layer. The capacity of the diffuse layer depends on the ionic strength (through the Debye length λ_D)^{xiii} and the electrode potential (E_0): $C_{GC}^A = \epsilon \epsilon_0 / \lambda_D \cdot \cosh(eE_0 / 2k_B T) \approx \epsilon \epsilon_0 / \lambda_D$ (to first order) [107]. Estimated values between 10-50 $\mu\text{F} \cdot \text{cm}^{-2}$ can be calculated for a 0.1 M monovalent salt in aqueous solution, which is in agreement with experimental values.

The capacity of the interface otherwise depends on the potential, as shown in Figure 24, and demands an even more detailed model to describe the structure of the metal-electrolyte interface to develop an appropriate relationship.

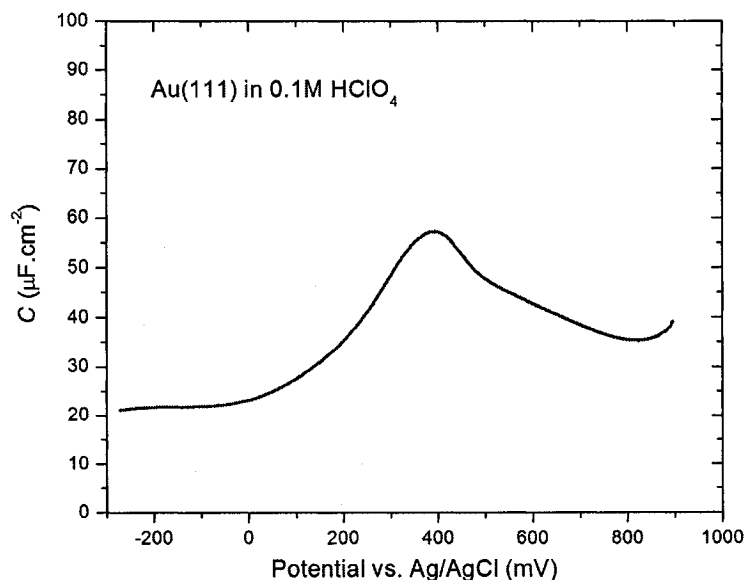


Figure 24: Differential capacity curve for a Au(111) electrode in 0.1 M HClO₄ electrolyte solution (unpublished experimental data used with the permission of I. Burgess, R. Nichols and J. Lipkowski).

^{xiii} For a monovalent salt in an aqueous solution at 25°C, $\lambda_D = 0.304 \text{ nm} / \sqrt{c_o \frac{\text{mol}}{\text{mol}}}$, where c_o is the salt concentration. For example, the Debye length of a 0.1 M aqueous NaCl solution is 0.96 nm.

4.2 Surface energy versus surface stress

A cyclic voltammogram (CV) in 0.1 M HClO₄ for the Au(111)-textured microcantilever is presented in Figure 25. The inset of the figure shows the CV during the charging of the electrical double layer interface. The weakly adsorbing perchlorate anions, ClO₄⁻, do not covalently bind to the WE surface. In the electric double layer region, the system is analogous to the charging of a capacitor. For non-specific adsorption, the interaction is dominated by long-range electrostatic effects as opposed to the very short range nature of specifically adsorbed species which are tightly bound to the electrode surface (i.e. charge transfer) as in the case of chloride anions, Cl⁻, for example. The current in the double layer region is referred to as capacitive current in contrast with the Faradaic current generated when charges are transferred between the WE and the electrolyte solution. The tail of the CV at negative potential is a consequence of hydrogen evolution (H⁺ reduction). The potential at which the hydrogen evolution appears is dependent on the pH of the solution. At the other end, when the CV is extended to more positive potentials, OH⁻ groups adsorb and oxidation of the surface takes place. The current peak above 1100 mV indicates the presence of an oxide film on the Au surface, although precursor oxide species start to form on the gold surface at around 800 mV [108]. The Au oxide formed during the anodic sweep (positive direction) is stripped off on the cathodic sweep (negative direction), as indicated by the presence of the sharp, negative peak at ~930 mV. The hysteresis between

the anodic and cathodic peaks on the CV arises from the electrochemical irreversibility of the oxide layer formation/dissolution. It should be noted that the shape of the CV is very sensitive to the cleanliness of the WE surface as well as the purity of the electrolyte solution and can be used to ensure the absence of contamination in electrochemical experiments.

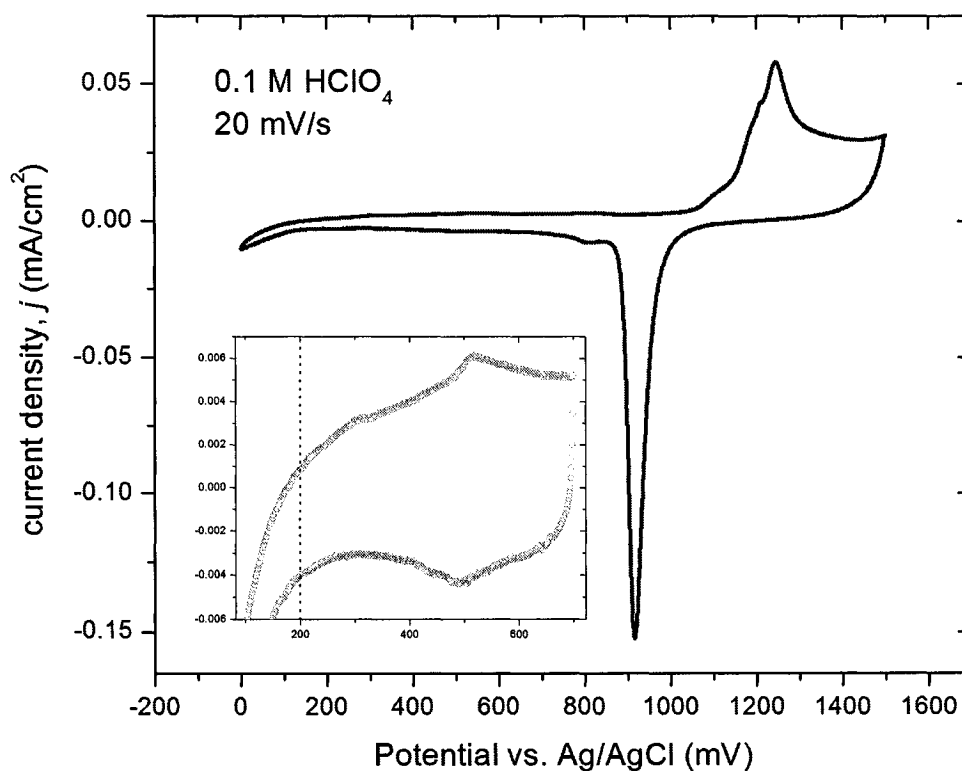


Figure 25: Cyclic voltammetry for the Au(111)-textured microcantilever in 0.1 M HClO₄ at a scan rate of 20 mV/s. The inset shows the current in the double layer region (the units are the same as in the figure).

It is possible to calculate the area of the WE by measuring the charge associated with the stripping of the oxide layer. This method is not extremely precise but it provides a good estimate of the WE surface area, taking into account the

roughness factor. The roughness factor is the ratio of the microscopic electrode area over the geometrical electrode area. Indeed, roughness at the microscopic scale can significantly increase the electrode area. The charge density associated with the oxide stripping voltammetric peak differs for the various crystallographic planes of gold, but it is considered to be $\sim 400 \mu\text{C}\cdot\text{cm}^{-2}$ for a polycrystalline (an average of all crystal faces) gold electrode.

The charge density on the surface can be obtained by integrating the current from Figure 25. The potential is linearly related to time since the potential sweep rate is constant. The relative charge density as a function of potential obtained is shown in Figure 26.

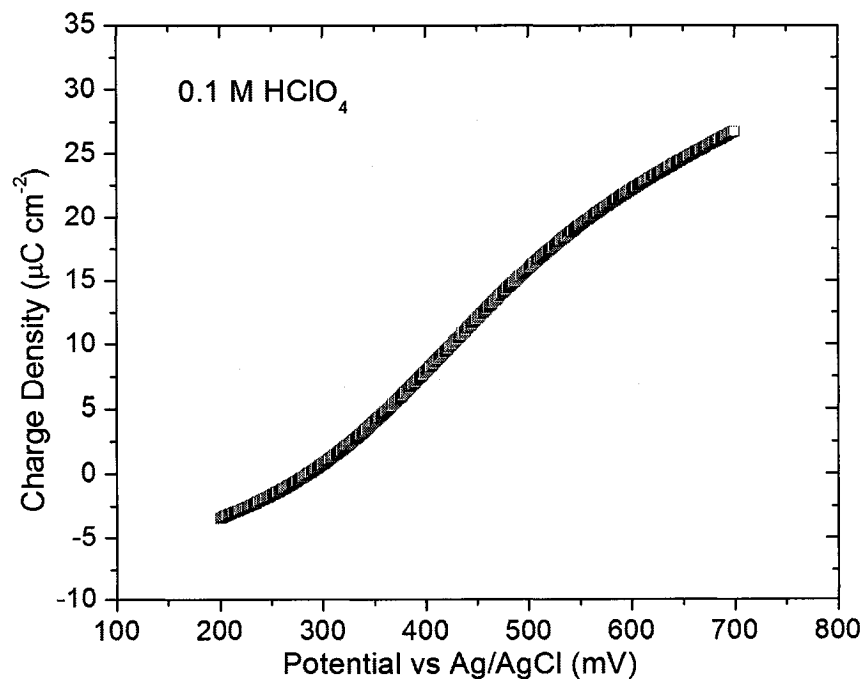


Figure 26: Charge density versus potential determined by integration of the CV of Figure 25 for the Au(111)-textured microcantilever.

The value of the potential of zero charge (PZC) was determined to be +250 mV vs. SCE using chronocoulometric measurements published by Lipkowski et al [109]. This corresponds to +285 mV vs. Ag/AgCl (immersed in 3M NaCl) since the potential of the type of reference electrode we use is approximately -35 mV relative to a saturated calomel reference electrode (SCE). The PZC for single crystal Au(111) in 0.1 M HClO₄ has also been previously measured to be +330 ±40 mV vs. Ag/AgCl. The value used is therefore in good agreement considering the microcantilever gold coating has polycrystalline contributions rather than being a single crystal. In fact different crystal faces exhibit different properties (e.g. PZC or work function) so that the behaviour observed at a polycrystalline electrode is an average of the number of different crystals faces or sites (which can carry different charge). In addition specific adsorption of anions (inevitable presence of some Cl⁻ anions of the Ag/AgCl reference electrode) will negatively shift the PZC.

The surface energy change in the double layer region can be calculated by integrating the charge density over the potential following Equation 4-5. Figure 27 shows the variation of the surface energy calculated from the Lippmann equation as a function of potential. The data was cut off at potentials less than 200 mV to prevent superfluous charge from hydrogen evolution from being included in the evaluation. The uncertainties associated with the surface area of the WE and with the magnitude of the current (unavoidable presence of oxygen in the electrolyte) produce an error on the evaluation of the surface energy which is

difficult to quantify. Nevertheless, it is informative to look at the magnitude of the surface energy change as well as its dependence on the applied potential to gain a better understanding of the different contributions of each term of the Shuttleworth equation, see Equation 4-3.

The surface energy change versus potential shown in Figure 27 is called an electrocapillary curve and has a maximum at the PZC.

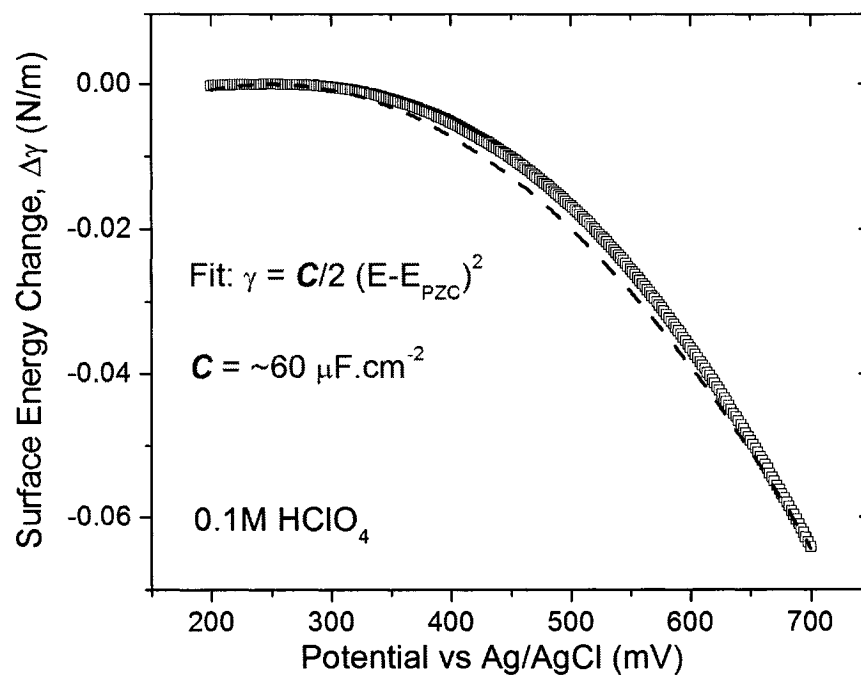


Figure 27: In blue, surface energy change, calculated from the Lippmann equation by integration of Figure 26. The electrocapillary curve reveals a parabolic shape. In red, a fit of the surface energy change assuming a constant double layer capacity.

The results for the change in surface energy correlate remarkably well with the simple model of the electric double layer discussed in section 4.1. The surface

energy curves reveal a parabolic dependence with potential and charge. Assuming a constant capacity of the interface, C , the surface energy (γ) curve can be fitted to an equation of the form $\gamma = (C/2)E^2$, or $\gamma = (1/2C)q^2$ as previously argued in section 4.1.1 and a value for the capacity of the double layer can be obtained. A capacity of $\sim 60 \mu\text{F}\cdot\text{cm}^{-2}$ is found which is in good agreement with previously reported values [110] and matches to first order the slope of Figure 26.

In Figure 27, the surface *energy* change measured over the potential range investigated is 65 mN/m. This is in agreement with previously reported values of surface *energy* change on a Au(111) electrode [111]. If we consider the relative changes observed compared to the absolute magnitude of the surface *energy* for Au(111), which is 1.25 N/m,^{xiii} the changes correspond to about 5% of the absolute value. Therefore, for the potential window investigated, the overall surface *energy* is weakly affected by changes in electrode potential.

In contrast, the results for the surface *stress* change as a function of potential are presented in Figure 28. Recall that the surface *stress* values are experimentally determined from the cantilever deflection experiments. Contrary to the surface *energy* change, the surface *stress* does not display a parabolic shape as a function of applied potential. In addition, the surface *stress* varies more strongly with potential than does the surface *energy*.

^{xiii} value for a clean, unreconstructed Au(111) surface from first-principles calculations, see table 2 from reference 102.

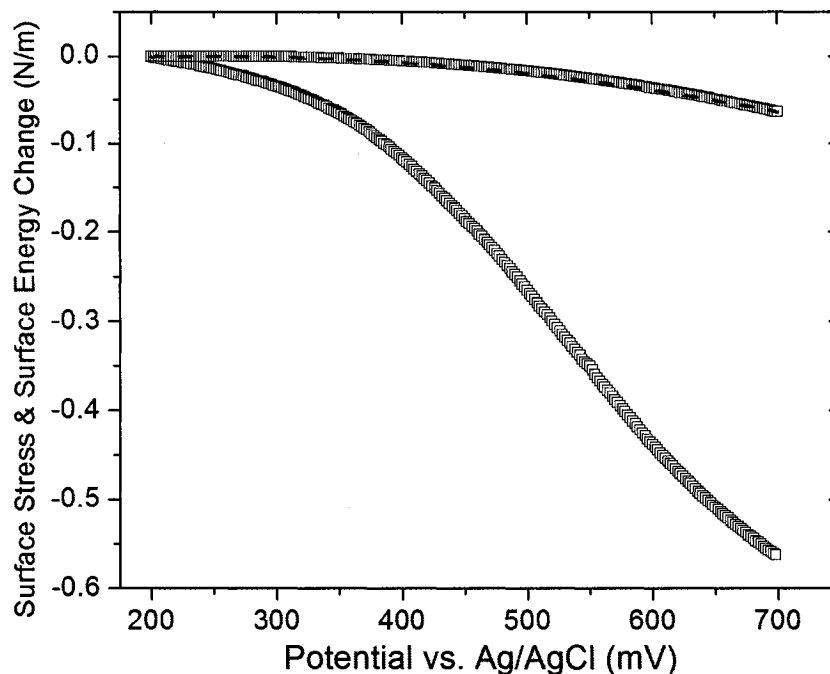


Figure 28: In black, change in surface stress as function of electrode potential for the Au(111)-textured microcantilever in 0.1 M HClO₄ electrolyte solution. Simultaneously measured is the surface energy change plotted in blue along with a parabolic fit shown in red, also shown in detail in Figure 27.

The surface *stress* change measured over the potential window investigated is on the order of 0.55 ± 0.06 N/m for a set of 20 independent experiments. The surface *stress* change is therefore one order of magnitude larger than the surface *energy* change for the case of a clean Au(111)-textured microcantilever surface in 0.1 M HClO₄ within the potential window investigated. In addition, the absolute value of the surface *stress* for Au(111) is about 2.77 N/m.^{xiv} This corresponds to a change of about 20% in the absolute magnitude. With this observation it becomes evident that for solid electrodes surface *energy* and surface *stress* differ significantly and

^{xiv} Native tensile surface stress value for a clean, unreconstructed Au(111) surface from first-principles calculations, see table 2 from reference 102.

this should help clarify some erroneous views which were based on the equality of the two parameters. The results shown in Figure 28 imply that the second term of the Shuttleworth equation $\partial\gamma/\partial\varepsilon$ is therefore certainly not negligible (see Equation 4-3). In fact, for a clean Au(111) surface in a HClO₄ electrolyte, it provides the largest contribution to the overall surface *stress* change.

4.3 Charge-induced surface stress

For a more intuitive analysis of the surface stress data, it is valuable to plot the surface stress change as a function of surface charge. Applying the chain rule to the derivative of the surface stress to the potential we obtain:

$$\partial\sigma/\partial E = (\partial\sigma/\partial q)(\partial q/\partial E) \text{ Equation 4-7}$$

where, σ , is the surface stress, E , the electric potential and q the charge. We can see from the above relation that in the potential representation (i.e. plotted versus potentials) the surface stress contains a contribution from the differential capacity, $\partial q/\partial E$, which can introduce some structure to the observed surface stress if the capacity is not constant over the range of potentials studied. Figure 29 shows the surface stress change as a function of the surface charge density of the gold-coated microcantilever. Interestingly, a linear relation between charge and surface stress is observed. This observation was previously reported by Haiss et al. [105]. The linear correlation is observed for positive surface charge densities where anions are attracted and interact with the surface. This is a very compelling

observation, since the measurement of the potential-induced surface stress provides direct knowledge of the charge density variation at the metal-electrolyte interface and vice versa. Indeed, this linear relationship is evident when comparing the results of Figure 26 and Figure 28.^{xv}

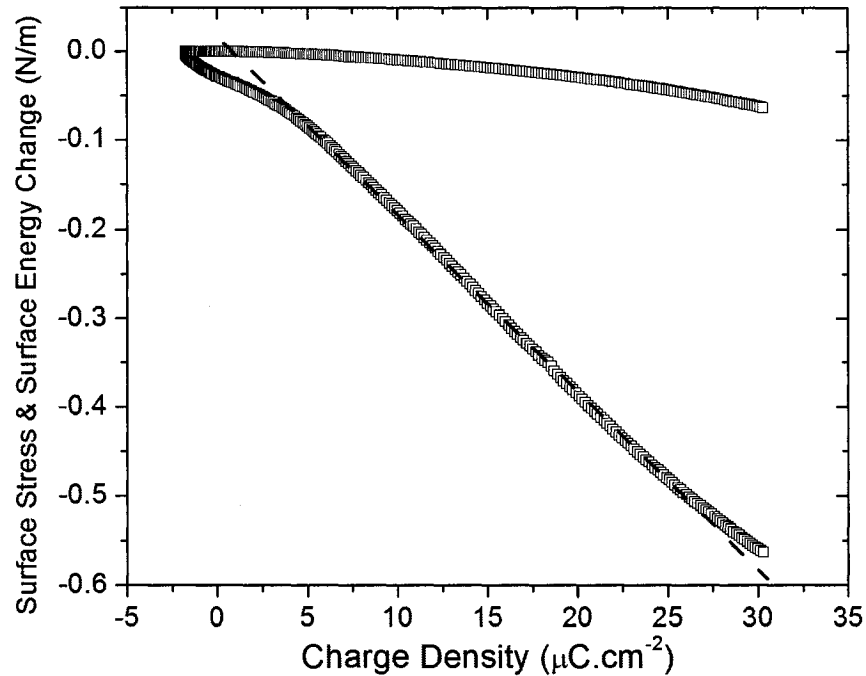


Figure 29: In black, the change in surface stress as function of charge density on the Au(111)-textured microcantilever electrode in 0.1 M HClO₄ electrolyte solution. Simultaneously measured is the surface energy change, plotted in blue.

The deviation from linearity observed at large, positive surface charge densities (high positive potential) can probably be attributed to the onset of oxide formation on the surface. At negative surface charge density and in the vicinity of the PZC, the surface stress is not linear. Two arguments can be put forward to explain this

^{xv} The results of Figure 26 multiplied by -1 mimic the results of Figure 28.

departure. The first explanation stems from experimental error. The surface charge density acquired in this potential window may not be accurate due to the presence of hydrogen evolution. Therefore, the purely capacitive current from the double layer charging may be superimposed with some Faradaic current. If the capacity is distorted, it will directly influence the slope of the surface stress versus charge density curve.

Alternatively, the linear relationship between surface stress and surface charge is caused by the specificity of ion adsorption which, in this case, occurs only for positive surface charge density (i.e. anion species). The linear relationship should therefore be observed for potentials positive of the PZC.

This is corroborated by the striking experimental observation of the parallelism between the cyclic voltammogram and the variation in first derivative of the surface stress, σ , with respect to the electrode potential, E .^{xvi}

$$\partial\sigma/\partial E \propto dq/dt = I \text{ Equation 4-8}$$

This was observed for a number of systems [105,112,113] and is shown in Figure 30.

^{xvi} Recall that $dE=vdt$, where v is the sweep rate.

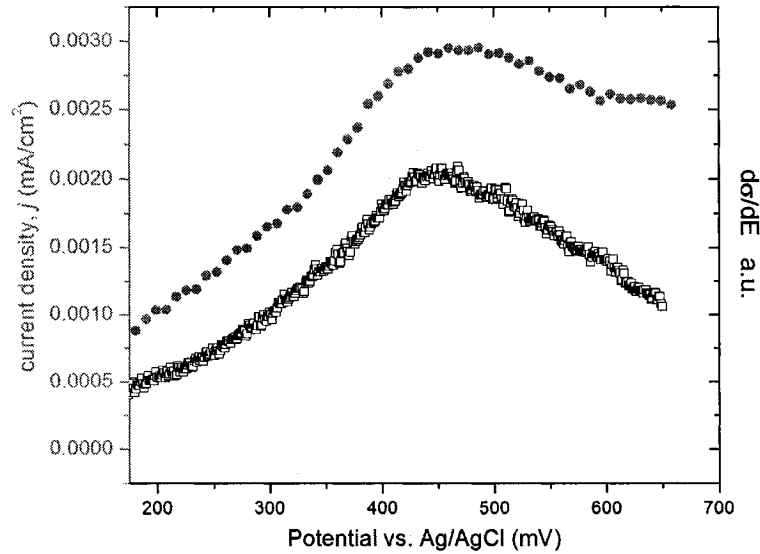


Figure 30: In green, current density during cyclic voltammetry of the Au(111)-textured microcantilever in 0.1 M HClO₄. In black, first derivative of the surface stress, σ , with respect to the electrode potential, E .

The data in Figure 29 were fitted to a straight line from 5 to 25 $\mu\text{C cm}^{-2}$. A value of the slope $\partial\sigma/\partial q \approx -2$ V is obtained. The value of the slope strongly depends on the capacity of the interface which relates potential and charge. This linear dependence on Au(111) was first reported by Haiss and Sass [105] who measured a slope of -0.91 V on flame annealed gold-coated glass cantilevers (15 mm \times 2.5 mm). This observation was later confirmed by Ibach [114], who obtained a slope of -0.83 V on single crystal gold cantilevers (4 mm \times 3 mm). The accuracy of this last result is somewhat questionable since the charge data was provided by another research group. Recall that the surface stress result shown in Figure 28 is in excellent quantitative agreement with the result of Ibach et al. [104] (see Figure 20). Only a smaller value (roughly by a factor a two) for the capacity of the interface can account for the discrepancy with the slope obtained from Figure 29.

On the other hand, the interfacial capacity obtained from Figure 26 is in good agreement with the values reported by Haiss et al. [105] and Lipkowski et al. [110]. However, the charge-induced surface stress change reported by Haiss et al. is approximately a factor of 2 smaller than the surface stress change observed in Figure 29. Consequently, these three entirely independent sets of data are in fair agreement, when one considers the uncertainty in the surface stress and in the surface charge density.

4.4 Specific adsorption and a simple model of the origin of surface stress

Up to now, the surface stress results presented were obtained in the presence of weakly adsorbed ions (ClO_4^-) on positively charged surfaces. To gain a better understanding of the origin of the measured surface stress at the solid-liquid interface it is valuable to study the surface stress response in a wider potential window to investigate the influence of the charge polarity of the electrode surface. In addition the effect of specific adsorption (i.e. charge transfer between anion the electrode) is examined.

Figure 31 shows the potential-induced surface stress in HClO_4 and NaCl electrolytes from -800 mV to +800 mV. The $\Delta\sigma$ values were set to be equal at the most negative potential investigated and the maximum in surface stress in each electrolyte was set to zero. This somewhat arbitrary procedure simply allows for a

convenient presentation of the results and does not affect the interpretation of the data.

The two curves in Figure 31 show an analogous dependence on the electrode potential. For potentials negative of the PZC, both surface stress curves vary smoothly and by a similar amount. The magnitude of the surface stress change remains relatively small compared to potentials positive of the PZC. Figure 31 reveals that most of the surface stress response takes place above the PZC where the surface is positively charged and anions interact with the electrode surface. In fact, the difference between these two curves relies on the specificity of the interaction of the anionic species. The surface stress curve in NaCl appears shifted with respect to the surface stress curve in HClO₄. This is because, in NaCl, the PZC is located at more negative potentials owing to the specific adsorption (i.e. charge transfer) of chloride on the electrode surface. Furthermore, in the potential representation (i.e. plotted versus potential), the surface stress change in chloride electrolyte is approximately twice as large as in the case of perchlorate.

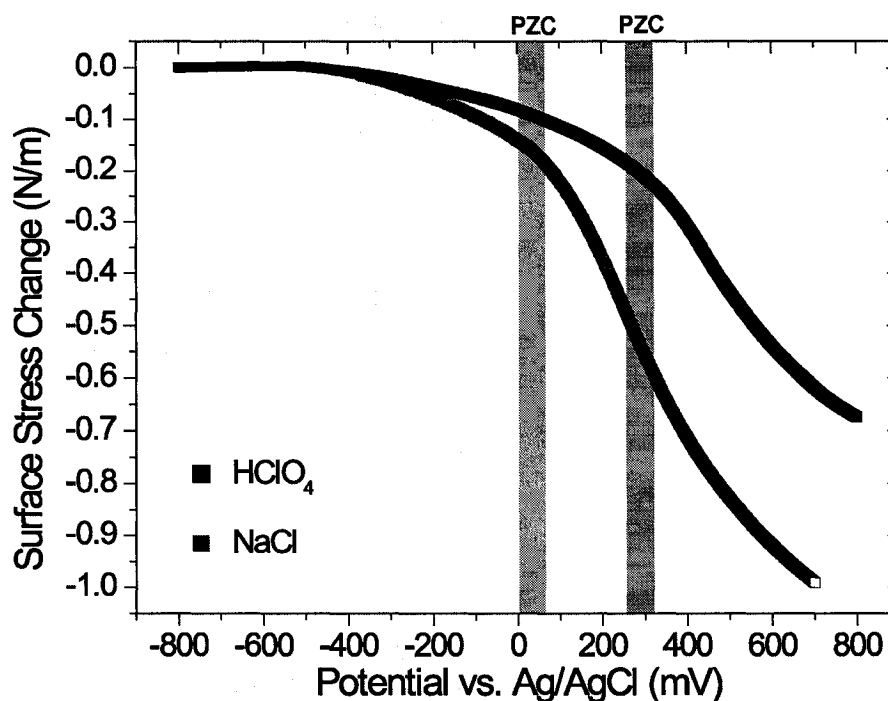


Figure 31: Change in the surface stress, $\Delta\sigma$, as a function of electrode potential for a Au(111)-textured microcantilever WE in 0.1 M solution of HClO₄ (black) and NaCl (blue).

The higher surface stress values obtained for chloride adsorption can be explained by the much larger capacity of the interface, so that many more charges are present on the metal electrode for the same variation in potential. In fact, in the double layer region, the differential capacity for a Au(111) electrode in a chloride electrolyte is three times larger than in a perchlorate electrolyte [110]. Consequently, if we were to plot the surface stress as a function of charge, the slope, $\partial\sigma/\partial q$, for chloride adsorption would be smaller than for the case of perchlorate. Haiss et al. [105] have previously reported this observation that the adsorbate-induced surface stress gets smaller with increasing bond strength. This interesting finding can be explained by a charge transfer between the adsorbed

anion and the metal surface [105].^{xvii} As a result, the charge density on the metal surface (q_{metal}) is significantly lower than the experimentally determined surface charge (q_{exp}); hence $q_{metal} = q_{exp} * c_{ct}$, where, c_{ct} is the charge transfer coefficient. It follows that the amount of charge transfer that takes place during adsorption processes can be estimated from the surface stress versus surface charge density plots as described in reference [102].

It is evident from Figure 31 that contrary to the surface *energy* change, the surface *stress* does not have a maximum at the PZC. Additionally, the surface stress change is clearly not symmetric about the PZC. The surface stress change is therefore governed by more than just electrostatic repulsion of charges at the interface.

In order to provide a clear picture of the physical origin of the surface stress from an atomistic point of view, let's first consider the basic example of the native tensile surface stress of clean metal surfaces. At a metal surface the coordination of the surface atoms will differ from their bulk counterparts because of the missing atoms above the surface. As a consequence, the electrons at the surface are redistributed so that the charge distribution near the surface will be different than in bulk. As pointed out by Ibach, a part of the bond charge at the surface is expected to flow into the space between the surface atoms, as depicted schematically in Figure 32. Consequently, there is an increase in charge density between the surface atoms, which effectively strengthens the inter-atomic bonds

^{xvii} This result can also be understood by saying that Cl⁻ adsorption produces a tensile surface stress (since it is an electron donor) competing with the compressive change in surface stress due to the double layer charging (i.e. positive charging of the electrode surface).

between surface atoms. Since the surface atoms are forced to stay in registry with the bulk, a tensile surface stress develops [115,116,117].^{xviii}

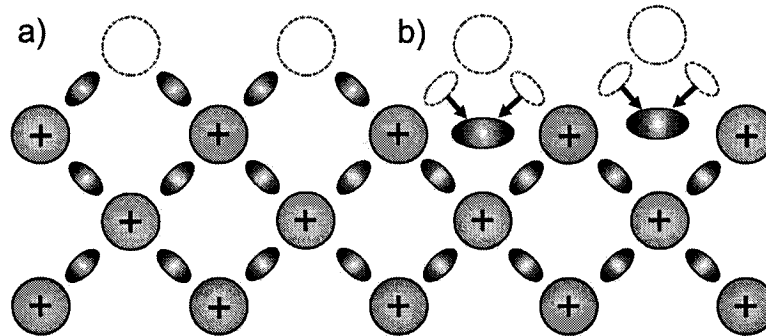


Figure 32: Simple model of the charge redistribution to explain the native tensile surface stress of many clean metals surface. The bond charges are depicted in grey and the positively charged ion cores in orange. a) Bond charges at a newly formed surface before redistribution. b) Bond charges flow into the space between the first layer of atoms and increase the bond strength between surface atoms.

If the surface charge density would remain the same as in the bulk, no surface stress would build up. In some instances, the tensile surface stress is large enough to initiate surface reconstruction to relieve some of the native tensile surface stress, as in the case of Au(111) which accommodates an extra Au atom in a $(23 \times \sqrt{3})$ reconstructed unit cell [102]. This simple model will be used to obtain a qualitative understanding for the sign of the surface stress at the metal-electrolyte interface.

^{xviii} This effect depends on the type of metals and electrons involved. For d metals, the surface stress originates in the competition between sp and d bonding and how the balance is modified at the surface. More specifically, for a $5d$ metal such as Au, the tensile surface stress is the result of a competition between the repulsive interactions between the filled d shells and an electron gas attraction from the mobile sp electrons. See references [115,116,117].

At the PZC, no excess charge resides on the microcantilever surface. When scanning the potential in the negative direction, the electrode becomes negatively charged and the microcantilever experiences a tensile surface stress. This observation can be understood by the additional increase in electron density at the surface which further strengthens the inter-atomic bonds between surface atoms. On the other hand, when the electrode is positively charged the microcantilever experiences a compressive surface stress. Electrons are now removed from the space between the first layer of atoms and the bond strength between surface atoms decreases. The surface stress generated is therefore in the compressive direction.

The repulsive interaction between adsorbates at the interface does not directly contribute, through electrostatic forces, to the observed surface stress change as the surface stress would otherwise be symmetric about the PZC.^{xix} While the variation of the surface stress is mainly caused by the response of the metal, the specificity of the adsorption is responsible for the structure of the potential-induced surface stress curve. For specific adsorption, the ions are in direct contact with the metal electrode and because of the greater dielectric constant due to the high polarity of the bond compared to water, the capacity of the interface is larger and the surface stress is more pronounced. For non-specific adsorption, the ions remain fully hydrated and the surface stress varies smoothly as the capacity is reduced. This reduction stems from water molecules separating the adsorbates and the surface. Hence the change in surface stress with electrode potential is caused

^{xix} Note that an electrostatic repulsion model similar to the one described in M. Godin PhD. thesis [117], predicts a parabolic dependence of surface stress with surface charge. In opposition, the experimental results revealed a linear relationship between charge and surface stress.

by the change in electronic structure in the substrate surface owing to the specificity of adsorption of ions and charging of the interface. This simplified view of the electronic structure at the surface enables an effective qualitative description of the induced surface stress at the metal-electrolyte interface.

4.5 Effect of Morphology, Adhesion and Cleanliness of the Au surface on the measured surface stress

To what extent is the absolute magnitude and form of the surface stress versus potential curve affected by the “*quality*” of the metal film? To conclude this Chapter, the role played by the morphology of the sensing substrate on the measured surface stress is examined. Possible sources of the somewhat dramatic difference between some published results, obtained under similar or apparently identical experimental conditions, are discussed (see section 4.1.2).

To obtain reliable and reproducible surface stress results it is important to control and characterize the gold surface morphology of the microcantilever. It was observed in Figure 20 that the results obtained on evaporated gold of the type shown in Figure 9 and Figure 33A agree exceptionally well with the single crystal results of Ibach et al [104]. However, to get a sense of the role of grain boundaries and grain sizes, on the measured surface stress, surfaces with different morphologies were produced and are shown in Figure 33.

4.5 Effect of Morphology, Adhesion and Cleanliness of the Au surface on the measured surface stress 87

Surface A has an average grain size of 100 ± 60 nm, as already described in section 2.1.3. The grains are flat and connected. The surface possesses no apparent discontinuities. Surface B has a much wider distribution of grain sizes. The grains remain flat, but the surface contains a few voids between the grains. Overall the gold film is still continuous. This is in contrast with surface C, where the gold film is discontinuous and composed of isolated flat islands. Lastly, surface D is a completely discontinuous gold film with totally isolated islands. The film contains no grain structures and possesses a very high surface roughness.

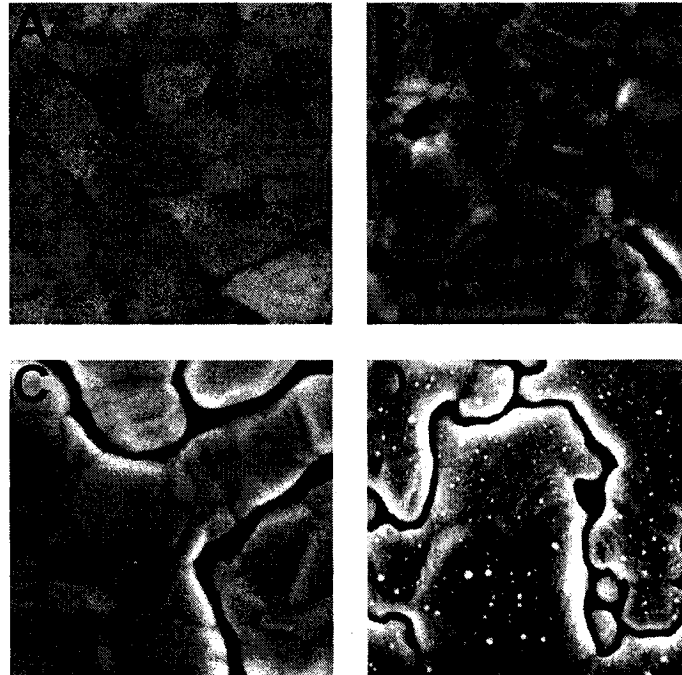


Figure 33: SEM images of various gold surface morphologies used in Figure 34. Surface A: evaporated gold film on a Ti adhesion layer under condition described in section 2.1.3, image size 500×500 nm². Surface B: sputtered gold film at 300°C grown on a Nb adhesion layer, image size 500×500 nm². Surface C: sputtered gold film at 400°C grown on a Nb adhesion layer, image size 500×500 nm². Surface D: evaporated gold film at 250 °C without an adhesion layer, image size 1×1 μm².

Each of these gold films was subjected to a potential scan from 0 mV to +700 mV, in 0.1 M HClO₄, while recording the induced surface stress. The results are shown in Figure 34. The inset of the figure shows the surface stress change for surface A, together with surface B and C which were scaled by a constant factor. The surface stress response between the evaporated and sputtered gold film are qualitatively similar. The smaller surface stress value generated on the sputtered film is most probably caused by the presence of voids and channels between the grains. It is envisaged that the discontinuities between the grains prevent the strain from propagating along the entire surface so that some stress is lost at the boundaries between discontinuous islands. The different grain size distributions do not appear to have a dramatic impact on the surface stress response, as revealed by the inset of Figure 34. The negative shift in potential of the surface stress curve observed for surface B and C can be attributed to the different PZC value of each surface. Surface D, which represents an extreme case of very rough and discontinuous surface, has a completely different surface stress response. The surface stress curve varies linearly with potential. This observation may be understood by the absence of crystallites on the surface so that all the features of the surface stress curve disappear.

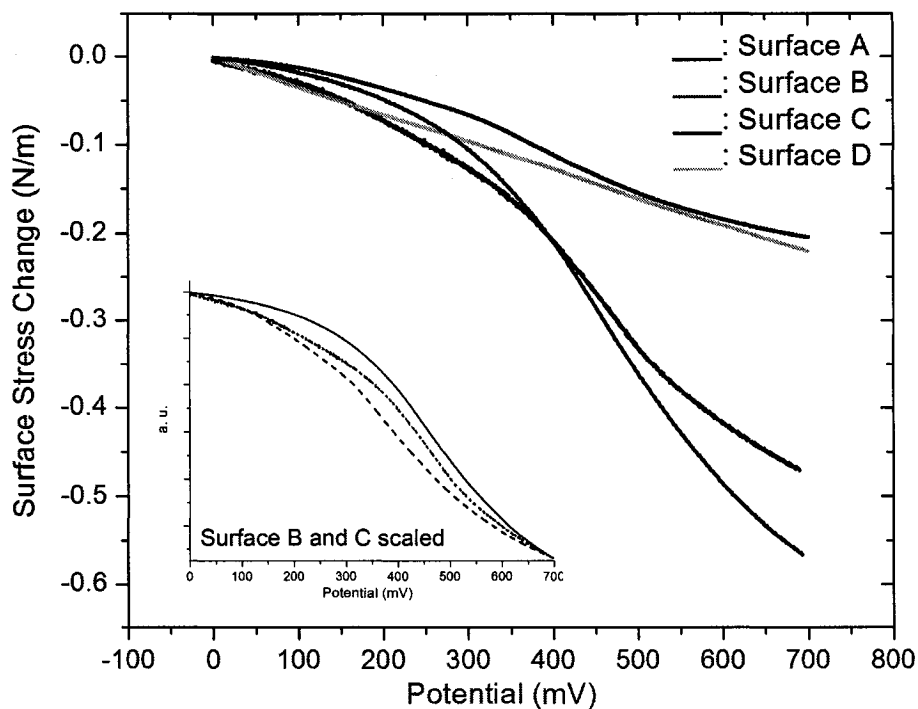


Figure 34: Potential-induced surface stress for various gold surface morphologies. SEM images of surface A, B, C and D are shown in Figure 33. The inset represents data from surface B and C scaled by a constant factor and surface A.

The results reported above do not constitute a complete investigation of the effect of the surface morphology on the surface stress response at the metal-electrolyte interface. Nevertheless, we have gained an insight into the role played by stress in the grain boundaries. Figure 20 and Figure 34 suggest that the magnitude of the surface stress is more affected by the presence of discontinuities in the gold film than by the size of the grain boundaries. It should be mentioned that the fact that the gold grain size has a negligible effect on the induced surface stress stems from the particularity of anion adsorption. It is known, for example, that surface stress during alkanethiol self-assembled monolayer formation depends strongly on the

gold grain size [106,118] due of the ordering of the alkyl chains and the size of domains of ordered thiol molecules.

Another important condition for obtaining reliable surface stress measurements is that the surface stress must be completely transferred to the underlying substrate. This condition is certainly fulfilled for results obtained on single crystal cantilevers. However when thin metal films are evaporated onto a substrate, is the adhesion adequate to ensure proper surface stress results?

Figure 35 presents the surface stress response of two Au(111)-textured microcantilevers in 0.1 M HClO₄ as a function of potential. The surface stress response of a gold film deposited on top of a Ti adhesion layer is shown in black. As previously demonstrated by Figure 20, since identical results were obtained on single crystals, the adhesion is good enough to transfer the potential-induced surface stress completely to the underlying silicon microcantilever. The surface stress response of a gold film deposited directly on a silicon microcantilever is shown in blue. The adhesion of the gold film to the silicon substrate is now significantly reduced. The film can be easily scratched or peeled off the surface. Care was taken when immersing the gold-coated microcantilever without an adhesion layer into the electrolyte solution to prevent the surface tension of the liquid from stripping off the film.^{xx}

^{xx} Note that the quality of the adhesion layer depends on the background pressure and the deposition rate during evaporation. See section for 2.1.3 details.

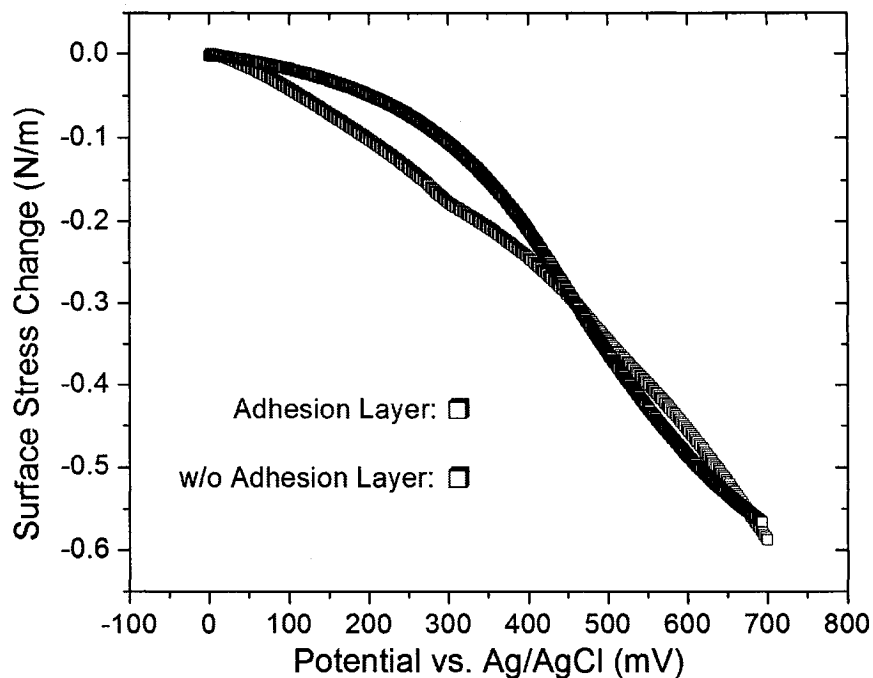


Figure 35: In blue, potential-induced surface stress acquired on an evaporated gold film without a Ti adhesion layer. For comparison, the surface stress acquired on an evaporated gold film with a Ti adhesion layer is plotted in black.

Interestingly, Figure 35 reveals a monotonic change in surface stress for both surface stress curves. On the film without an adhesion layer, the potential-induced surface stress curve has a slightly altered shape which can be explained by a somewhat different surface morphology of the gold film. In spite of this and most importantly, the magnitude of the surface stress change is not affected by the loss in adhesion. The adhesion of the metal film must therefore be exceptionally poor to not properly transfer the surface stress to the underlying substrate.

Lastly, the impact of the cleanliness of the gold surface on the potential-induced surface stress is examined. It should be highlighted that all of the surface stress

results on gold-coated microcantilevers presented hitherto were performed on electrochemically cleaned surfaces. By sweeping the voltage from 0 to 1500 mV as shown Figure 25, the gold surface is cleaned through gold oxide formation and removal, thus exposing a *new* gold surface.

To produce the *dirty* surface, a freshly evaporated gold surface was simply exposed to the lab environment for about week. X-ray Photoelectron Spectroscopy (XPS) performed on gold surfaces having been exposed to ambient laboratory air for days revealed the presence of contamination species containing carbon and oxygen. The *dirty* gold working electrode is scanned from 0 to +700 mV while recording the potential-induced surface stress. The WE potential is then swept between 0 and 1500 mV to electrochemically clean the gold surface. The freshly exposed gold is once again scanned from 0 to +700 mV.

In Figure 36 the surface stress response of clean and unclean gold-coated microcantilever in 0.1 M HClO₄ is shown as function of the electrode potential. The potential-induced surface stress response of the dirty surface reveals a dramatically different profile than that obtained from a clean gold surface. The surface stress versus potential curve, for the *dirty* gold, describes an exact parabolic shape. This surprising observation demonstrates that not only the absolute magnitude but also the shape of the surface stress versus potential curve can change when the electrode surface is not cleaned prior to the start of the experiment. This parabolic behaviour is reminiscent of the change in surface energy calculated from the Lippmann equation. The resemblance between Figure 28 and Figure 36 is striking. The finding that the surface stress versus potential

4.5 Effect of Morphology, Adhesion and Cleanliness of the Au surface on the measured surface stress 93

curves, obtained in previous microcantilever studies, resembles more or less the change in surface energy may therefore be linked to the cleanliness of the sample.

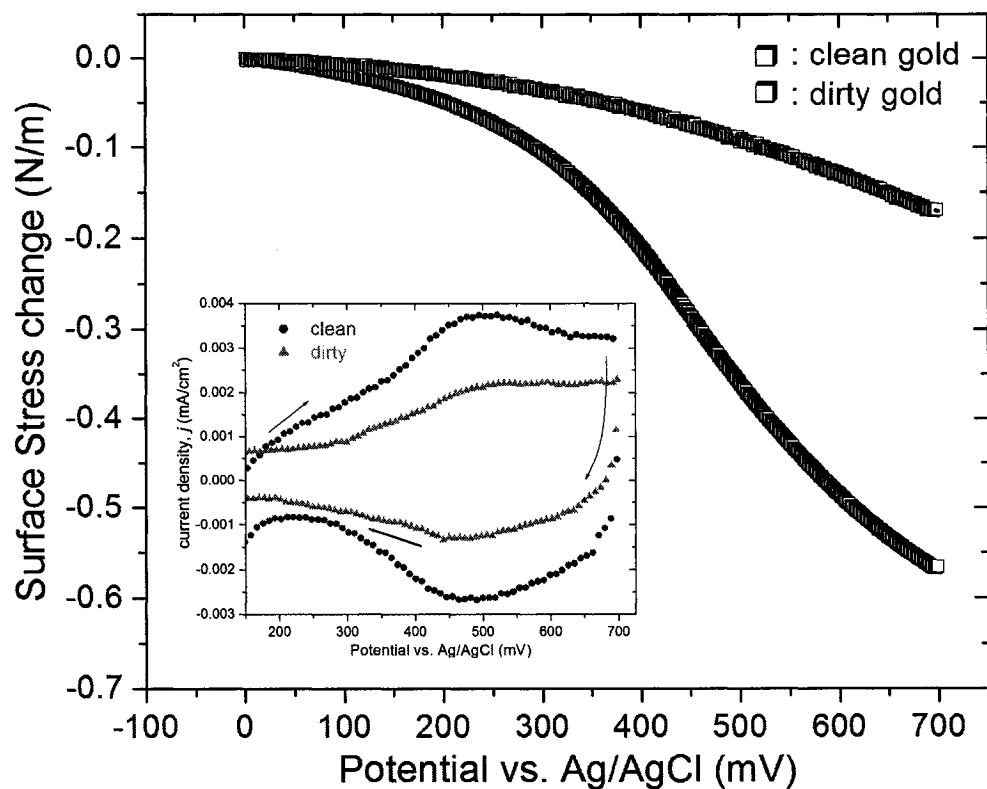


Figure 36: Potential-induced surface stress in 0.1 M HClO₄. In black the surface stress response of the freshly cleaned gold surface is shown. In blue, the surface stress of an unclean gold surface. In red, a parabolic fit. The inset is the corresponding CV for both clean gold (circles-higher current values) and unclean gold (triangles-lower current values) surfaces. The surface stress results represent the anodic sweep (positive direction).

It has been shown in section 4.3 that the surface stress change mimics the surface charge density variation. This linear relationship between charge and surface stress is compelling since it enables one to predict the potential-induced surface

stress profile from the cyclic voltammetric measurements. Therefore, to understand the parabolic shape of the surface stress curve obtained for the *dirty* gold surface, we can tentatively make use of the previously developed relationship $\partial\sigma/\partial E \propto I$ (see Equation 4-8). This relation predicts that the parabolic surface stress curve, $\Delta\sigma(E)$, ought to be associated with a linear variation in current, I . Unfortunately, for the *dirty* gold surface it is evident that I is not a linear function of E as revealed by the inset of Figure 36. Interestingly, the CV data for both clean and dirty surfaces are similar. For the latter, the onset of hydrogen evolution is kinetically hindered due to the presence of contaminants on the surface. In addition, the current value is approximately 30% lower but follows a parallel trend. As expected, the capacity is also smaller than for a clean gold surface, since $I \propto C \cdot \nu$, where I is the current, C the capacitance, and ν the CV scan rate. Therefore, despite the qualitative similitude between the surface stress and the surface energy curves, the two parameters still differ quantitatively.

The following conclusion can be drawn from the above observation. The linear relationship between surface charge and surface stress apparently holds only for a clean surface.^{xxi} This is not a real surprise, since it was argued in section 4.3 that this result is most likely due to adsorption of ions on the metal surface. Hence, for a *dirty* gold surface, the effect of ion adsorption does not contribute to the measured surface stress since the presence of contaminants protects the surface from specific adsorption. Therefore, it can be argued that the parabolic

^{xxi} It has only been experimentally verified on Au(111). It remains to be seen on other metal surfaces or other crystallographic orientations.

4.5 Effect of Morphology, Adhesion and Cleanliness of the Au surface on the measured surface stress

dependence on potential is the contribution from the metal to the surface stress (i.e. a redistribution of its surface electronic structure), whereas the features in the surface stress curve are due to adsorption of ions (i.e. specificity of the adsorption – amount charge transfer with the surface and adsorbate-adsorbate interactions). This means that the difference between the shapes of the two curves in Figure 36 is due to the specificity of adsorption of anions with the surface.

This finding is supported by the theoretical work of Schmickler and Leiva [103] who pointed out that in the absence of specific adsorption the surface stress varies smoothly with surface charge or potential and any fine structure is caused by specific adsorption. This was later confirmed by Xie et al. [119] who also indicated that the surface stress at the metal-electrolyte interface is mainly caused by the response of the metal, which varies smoothly, while the contribution of specific adsorption is important for the shape of the surface stress curve.

Evidently, further experimental work is required to confirm these initial observations and assessments. A more defined system, which would provide better control of the interface, must be investigated. A gold-coated electrode modified with an alkanethiol self-assembled monolayer (SAM) may be a suitable analogous system to dirty gold. A defect free alkanethiol SAM forms a well oriented and ordered film which effectively blocks any electrochemical reactions between the gold surface and the electrolyte solution. In addition, within the so-called double layer region of potentials, self-assembled monolayers display a

constant capacity indicating very stable (i.e. no electrodesorption) molecular films.

A gold coated microcantilever was incubated into 1mM dodecanethiol ethanol solution for a week, to form a highly ordered SAM. The microcantilever was then scanned in a 50 mM NaCl electrolyte from -200 to +400 mV while recording the potential-induced surface stress. The -200 mV mark represents the onset of hydrogen evolution. Results on the alkanethiol SAM system are shown in Figure 37. The change in surface stress measured in NaCl within the potential window investigated is only -9 mN/m compared to approximately -700 mN/m on bare gold (see Figure 31 for comparison). The very small value of the surface stress change is attributed to the low capacity of a dodecanethiol-modified gold electrode which is approximately $1 \mu F \cdot cm^{-2}$ [120].

This experiment reveals a parabolic potential-induced surface stress which qualitatively resembles the change in surface energy obtained for a SAM-modified gold electrode [120]. This observation is consistent with the description provided above. The contribution to the surface stress by anion adsorption is excluded so that only the contribution from the metal is measured. This finding is again in agreement with the prediction of Schmickler and Leiva [103].

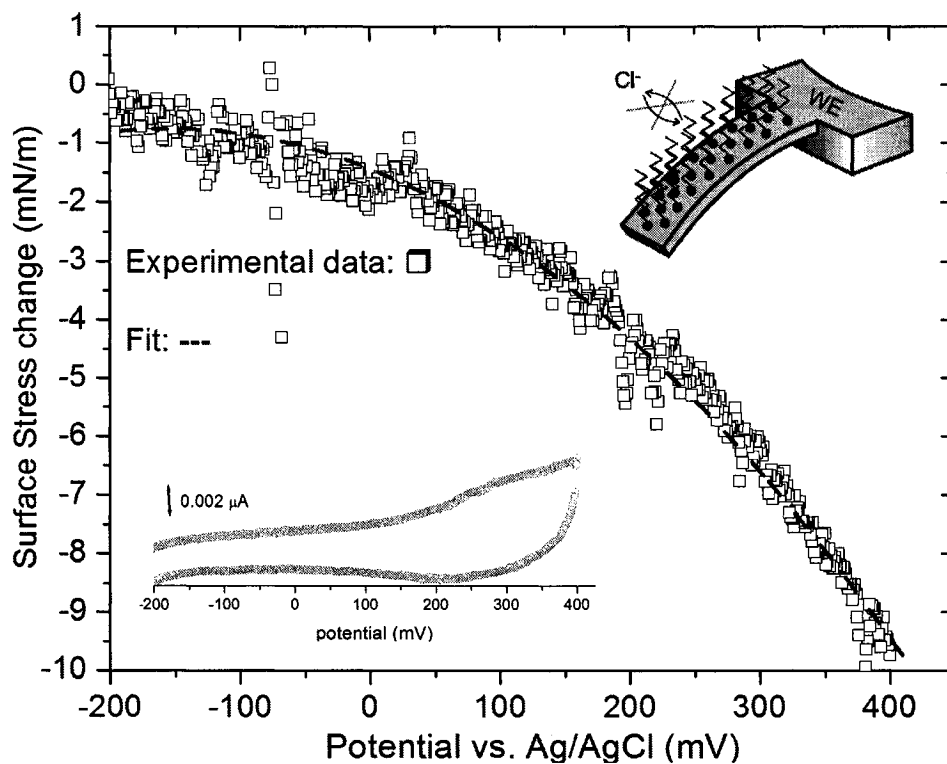


Figure 37: Potential-induced surface stress of an alkanethiol self-assembled monolayer covered gold-coated microcantilever in 50 mM NaCl electrolyte. For comparison the potential-induced surface stress on a bare gold coated microcantilever in NaCl is shown in blue in Figure 31. The corresponding CV is shown as an inset. The variation in the current is most probably due to a compression of the SAM layer exerted by the anions, modifying its thickness and affecting the capacity of the interface. (Data obtained in collaboration with T. Monga)

4.6 Summary

Simultaneous measurements of the surface stress and surface energy change at the solid-liquid interface were presented. For solid electrodes, the two thermodynamic quantities were shown to be significantly different. The change in surface stress of

a clean Au(111)-textured microcantilever was found to vary more strongly than the surface energy. The surface stress results are in an excellent agreement with other single crystal results [104,105]. In addition, the thermodynamic parameters obtained, such as the capacity of the interface, compare exceptionally well with previously reported values [110]. A linear correlation between surface stress and surface charge was reported. This important result enables the prediction of the potential-induced surface stress profile from cyclic voltammetric measurements. Consequently, in the potential representation the surface stress is dominated by the differential capacity of the interface.

The role played by the sensing surface morphology on the surface stress response was examined in an attempt to elucidate the controversial results previously obtained with microcantilever sensors. For the types of surfaces studied, in contradiction to an earlier report [121], there is no evidence of a parabolic shape of the surface-stress-potential curve for rough or sputtered films. Furthermore, the adhesion of the metal films was found to be adequate in completely transferring the surface stress to the underlying substrate. Conversely, the cleanliness of the metal electrode was found to significantly influence both quantitatively and qualitatively the surface stress response at the solid-liquid interface. Interestingly, it was found that in the particular case where the gold surface is protected from specific adsorption, the surface stress response qualitatively resembles the change in surface energy calculated from the Lippmann equation, so that the difference between the two quantities is not as evident.

Finally, the surface stress results acquired on alkanethiol SAM modified electrodes revealed that the surface stress signal is extremely sensitive to defects

in the SAM layer. These defects leave gold exposed to ions in the electrolyte solution. The total capacity of the interface is therefore increased since the capacitance of the thiol layer must be taken in parallel with that of the uncoated part of the gold surface. It is observed that the surface stress profile is very sensitive to changes in capacity of the interface. This is actually an ongoing research project in our group where the change in surface stress is being correlated to a specific type of defects (point or extended defects) in the SAM layer.

5 Redox-induced Surface Stress of Polypyrrole-based Actuators

The development of tools to manipulate biological entities is of major importance for tomorrow's medicine particularly in genomics, where one of the goals is to be able to characterize and control single cells in a massively parallel fashion. To actuate micromanipulators, micro-artificial muscles are needed, which would operate under physiological conditions. Conjugated polymers such as polypyrrole (PPy) are well suited for these types of biomedical applications [122]. They are compatible with aqueous media and operate at low voltages, unlike conventional piezoelectric actuators. Moreover, microfabrication techniques and materials can be used for their deposition and patterning to produce micrometer-size structures for laboratory-on-a-chip devices [123].

Such microactuators are based on a reversible volume change of the conjugated polymer upon oxidation and reduction [124]. By sweeping the film's potential in an electrolyte solution, polypyrrole can be electrochemically switched between its oxidized (PPy⁺) and reduced (PPy⁰) states [125]. In a bilayer configuration, such

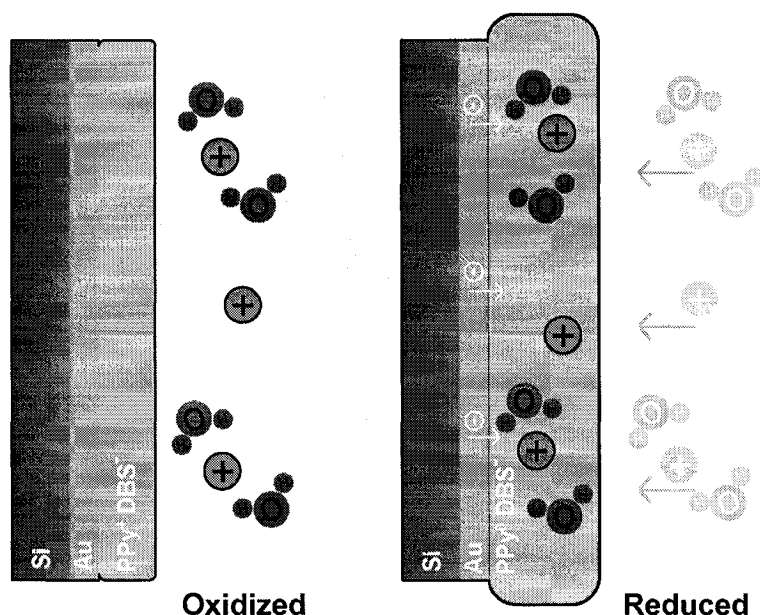


Figure 38: Schematic representation of the mechanism of actuation of a PPy(DBS) film. When electrochemically switched from its oxidized (PPy⁺, doped) to reduced (PPy⁰, neutral) state the PPy(DBS) film swells owing to the incorporation of Na⁺ ions (plus signs) and their solvation shell (H₂O molecules surrounding the plus signs). The bulky DBS anions are trapped inside the polymer and do not diffuse in and out of the polymer matrix.

In this chapter, I present surface stress results for dodecyl benzenesulfonate-doped polypyrrole (PPy(DBS)) films actuated by cyclic voltammetry in aqueous solutions. The bending response of the PPy(DBS)/Au-coated silicon microcantilever is measured as a function of the applied potential, simultaneously yielding real-time, in situ, electrochemical and surface stress information. The surface stress sensor's response during the anomalous first reductive scan as well as the effect of long term cycling on the mechanical transformation ability of PPy(DBS) actuators in both surfactant (NaDBS) and halide (NaCl) based electrolyte are discussed.

5.1 Sample Preparation

5.1.1 Pre-treatment of the WE gold surface

The gold surface is electrochemically cleaned in 0.1 M HClO₄ solution preceding the deposition of the conjugated polymer onto the gold-coated microcantilever. The voltage is swept from 0 to 1500 mV (all potentials quoted are versus Ag/AgCl) at a scan rate of 20 mV/s (Figure 39). This procedure cleans the gold surface through gold oxide formation (oxidation peak at 1220 mV) and removal (reduction peak at 934 mV), but also surprisingly passivates the silicon back side of the gold-coated microcantilever. Indeed it is found that if this step is omitted prior to PPy electropolymerization, the conjugated polymer gets electrodeposited on both sides of the microcantilever. In such a case, interpretation of the sensor's response becomes extremely difficult, since competing surface stress changes are generated on both sides of the microcantilever.

From the value of the oxide stripping charge [132] we can determine the relative roughness of the gold surface. A rougher surface enhances the adhesion (mechanical interlocking) between the polymer and the gold film [133]. In the present case, this stripping charge did not significantly change between gold surfaces used in different experiments, indicating that the adhesion between the PPy film and the gold surface remained very similar in all of our experiments. Additional information can be extracted from the CV measurements. The shape of

the oxidation peak can be indicative of the crystallographic texture of the gold film. The presence of a relatively sharp oxidation peak at 1220 mV indicates a {111} textured gold [134] which is corroborated with X-ray scattering results, which show a predominance of a polycrystalline Au(111) surface.

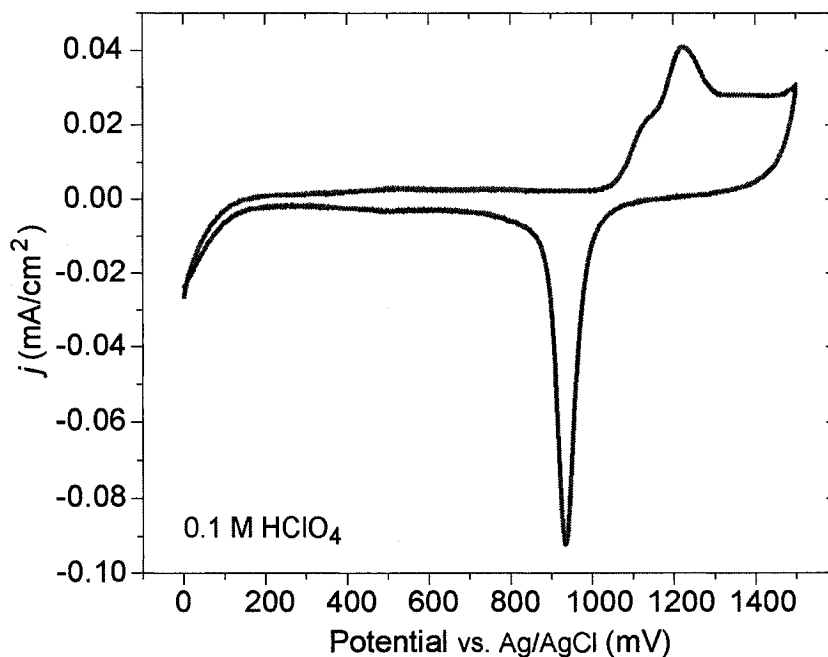


Figure 39: Cyclic voltammogram, recorded at a scan rate of 20 mV/s for a gold-coated microcantilever in 0.1 M HClO₄ solution. The Au oxide formed at potential above 1100 mV is stripped off on the cathodic sweep (sharp peak at 934 mV).

5.1.2 Deposition of PPy

Following the gold surface cleaning procedure, the PPy film is electropolymerized from an aqueous solution containing 0.1 M Py and 0.1 M NaDBS at a constant potential of +550 mV (vs. Ag/AgCl). This value of the potential is chosen to

ensure a more uniform film thickness [126]. The final PPy film thickness depends on the charge associated with electropolymerization. The polymerization current has a steady state value, so that the deposition rate of the PPy film is constant and the PPy film thickness depends linearly on time, or in other words, on the total charge consumed.

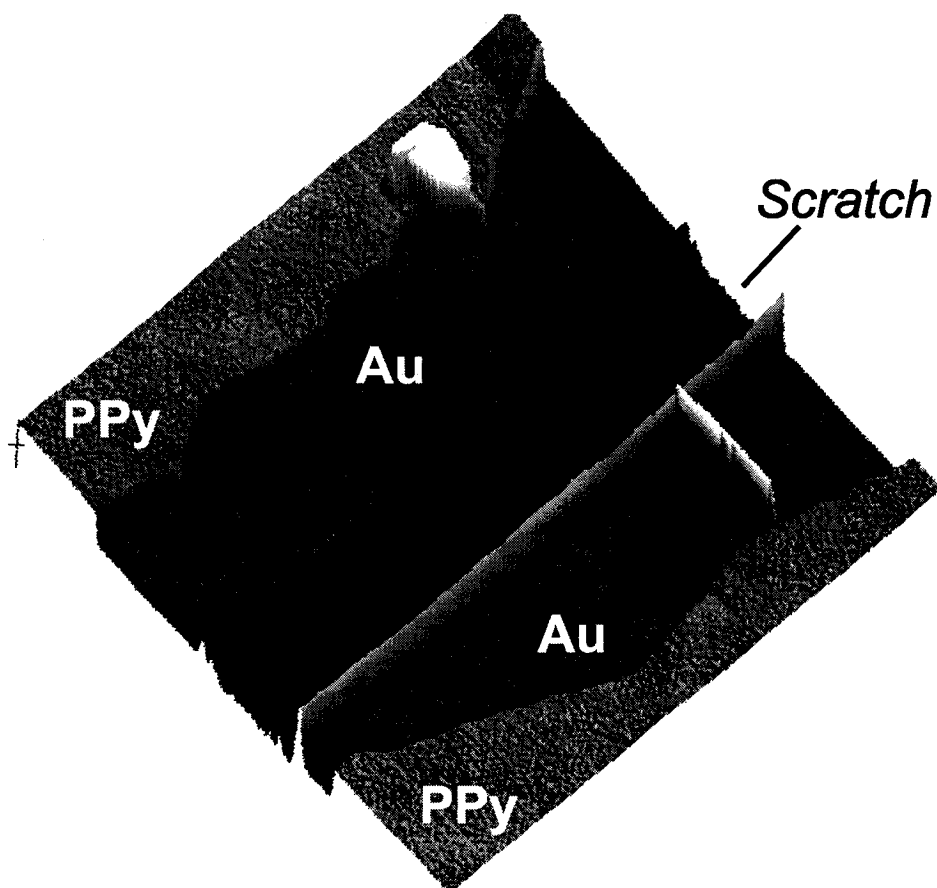


Figure 40: AFM contact mode image of a step made by the scratching the PPy film with a razor blade to determine its thickness. The light brown and the dark brown regions are the PPy film and the gold substrate respectively, as indicated in the image. The image size is $70\ \mu\text{m} \times 70\ \mu\text{m}$ and the height scale is 500 nm.

For the data presented here, the potential was applied for 200 seconds. To verify the reproducibility of the PPy film thickness on the WE and to develop a constant of proportionality between the PPy film thickness and the charge consumed, direct AFM imaging of steps made in PPy films by scratching the surface with a razor blade was performed. AFM measurements were done on freshly polymerized PPy film (oxidized state). Figure 40 shows the resulting AFM image. Prior to imaging, the AFM instrument was calibrated in the vertical direction by a grid sample with fixed depth.

Imaging was done in both contact and tapping mode to investigate the effect of tip loading in the height analysis. No significant step height differences were revealed by comparing the two imaging modes. In addition, following a simple Hertz model, the possible indentations produced by the tip are only on the order of the a few nm. The bearing analysis of the NanoscopeIII software (version.4.43r8, Veeco instruments, USA) was used to measure the height difference between the PPy film and the gold substrate and is shown in Figure 41.

The bearing analysis gives a statistical distribution of the different heights in the image. The width of the height distribution in the bearing analysis is used to estimate the precision of a measurement.

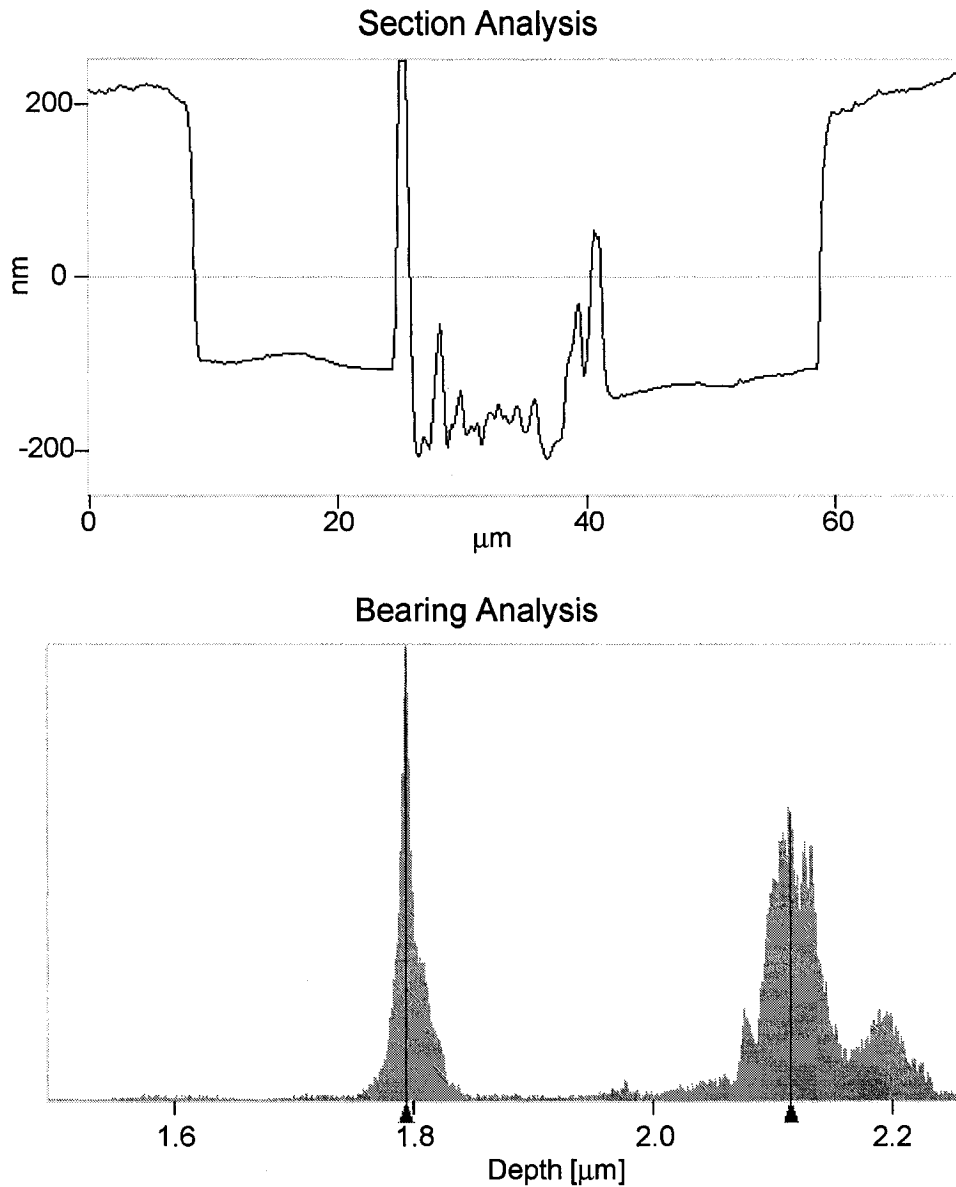


Figure 41: the top image is a cross section analysis and the lower image is a bearing analysis to measure the height difference between the polymer and the gold surface.

The average value obtained for a series of five PPy films on microcantilevers gives a consistent PPy film thickness of 304 nm with a standard deviation of 9 nm. This result shows the consistency of the implemented method for defining the

WE area, with a reproducibility of 3% in the PPy film thickness. In addition, the green color of the PPy(DBS) film on gold resulting from light interference matches the reported color for a 300 nm thick film which confirms the accuracy of the measured film thickness. The reproducibility of the PPy film thickness is mostly affected by the variability of the polymerization current, and by the error of the AFM measurements. In fact, the non-uniformity of the PPy film, although minimized, increases the error in the AFM measurements [126].

Therefore, for the system presented herein, I have empirically found a constant of proportionality between the PPy film thickness and the charge consumed of:

$$t \text{ (nm)} = 2.8Q \text{ (mC.cm}^{-2}\text{)} \quad \text{Equation 5-2}$$

Different charge-thickness relationships have been used by various groups, from experimentally determined constants to more sophisticated equations involving the film density and the molecular weight of the film and of the dopant (in proportion to the doping degree) [135]. Due to the variability associated with these parameters it is difficult to compare the value we have found with previously reported relations. Therefore, to obtain an accurate film thickness, the charge-thickness relationship should be calibrated for individual systems.

Figure 42 shows polymerization current simultaneously with microcantilever deflection during the electrodeposition of PPy onto the Au-coated microcantilever surface. After a time, $t = 200$ s, the polymer films obtained and used during this study have an average thickness of $304 \text{ nm} \pm 9 \text{ nm}$ [126]. Note that monitoring the microcantilever deflection during electrodeposition of the PPy film induces some local polymerization initiated by photoexcitation on the microcantilever Si

backside. This was observed later with an optical microscope and is manifested as a slight kink in both the current and the deflection data at about 140 seconds. Therefore, the study of the PPy actuation properties is performed on PPy-coated microcantilevers for which the deposition-induced deflection was not monitored. The PPy(DBS) films were smooth and uniform in color when observed under an optical microscope. The AFM image, shown in Figure 43 of the film morphology revealed the presence of nodules (~ 100 nm in diameter), which are characteristic for such thin films [136].

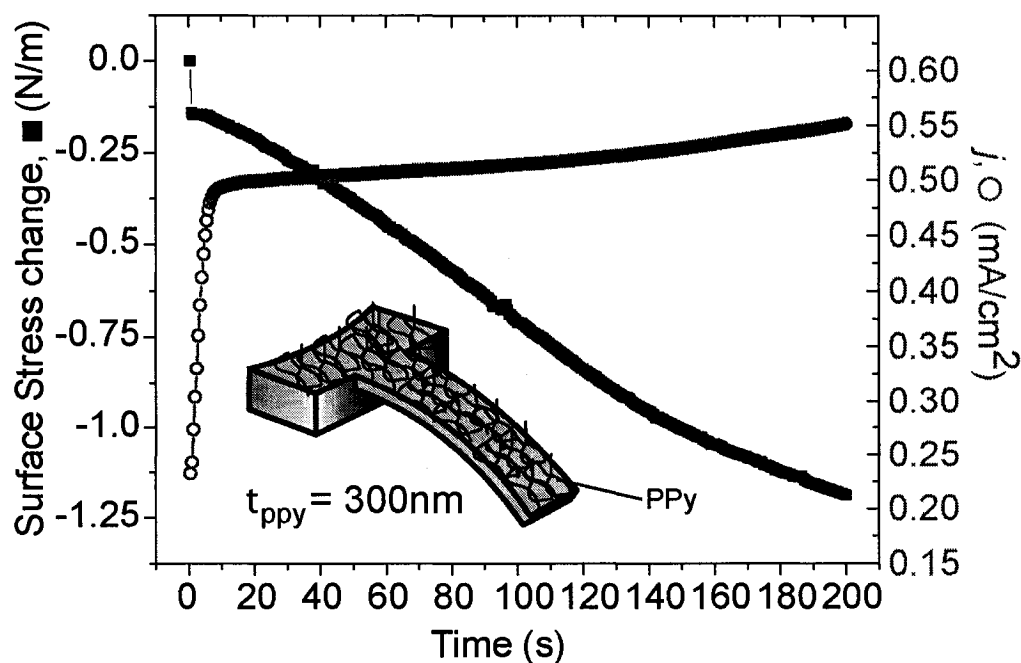


Figure 42: Simultaneous polymerization current (green circle) and surface stress (black square) during PPy electropolymerization at constant potential, $E = +550$ mV, for $t = 200$ s. The sudden jump at $t = 0$, is due to the change of potential of the gold surface, from the rest potential to +550 mV.

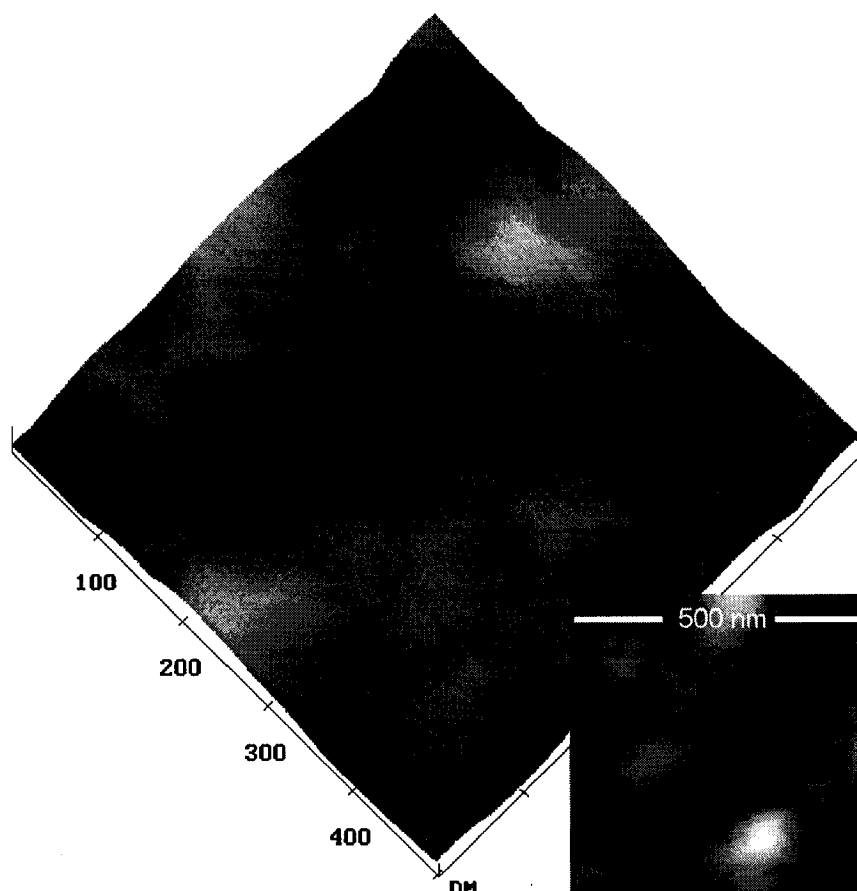


Figure 43: AFM image of the electrodeposited PPy(DBS) film on a gold-coated cantilever. The surface plot image size is $500 \times 500 \text{ nm}^2$, height contrast is 30 nm. As an inset, the top image view is shown, height contrast is 60 nm. The film morphology revealed the presence of nodules approximately 100 nm in diameter.

5.2 Redox-induced Surface Stress

5.2.1 Actuation Principle of conducting polymers

The reversible oxidation and reduction of a conducting polymer film can be associated with a considerable volume change of the polymer [137]. It has been

proposed that mechanisms of actuation in conducting polymers can be divided into two contributions [138]: First, an intrinsic part originates from changes in conformation and in carbon-carbon bond lengths of the polymer induced by changes in the charge density in the polymer backbone and second, a swelling part arises from the insertion of ions from the electrolyte solution to maintain electroneutrality in the polymer film. The latter part is composed of an osmotic expansion due to insertion of ions, and their solvation shells (e.g. water molecules) inside the polymer matrix, changing the ionic concentration in the polymer and creating an osmotic pressure difference between the polymer and the electrolyte solution. This increase in osmotic pressure forces additional water molecules to enter the polymer phase and thus produces an additional increase in polymer volume.

5.2.2 Surface stress during redox reaction in PPy(DBS)

Mechanical changes in the PPy film are actuated by cyclic voltammetry in a 0.1 M NaDBS^{xxii} while monitoring the microcantilever deflection. The electrode potential is initially swept from its rest potential to -850 mV, and back to +300 mV at a scan rate of 100 mV/s. Within this potential window, the PPy film is cycled between its oxidized and reduced states, as shown in Equation 5-1 and Figure 38.

^{xxii} In most cases, to prevent exchange of ionic species between the polymer phase and the electrolyte, and to facilitate the interpretation of the CVs, the same solution is used during polymerization and actuation. NaDBS is therefore often employed as a supporting electrolyte during actuation applications.

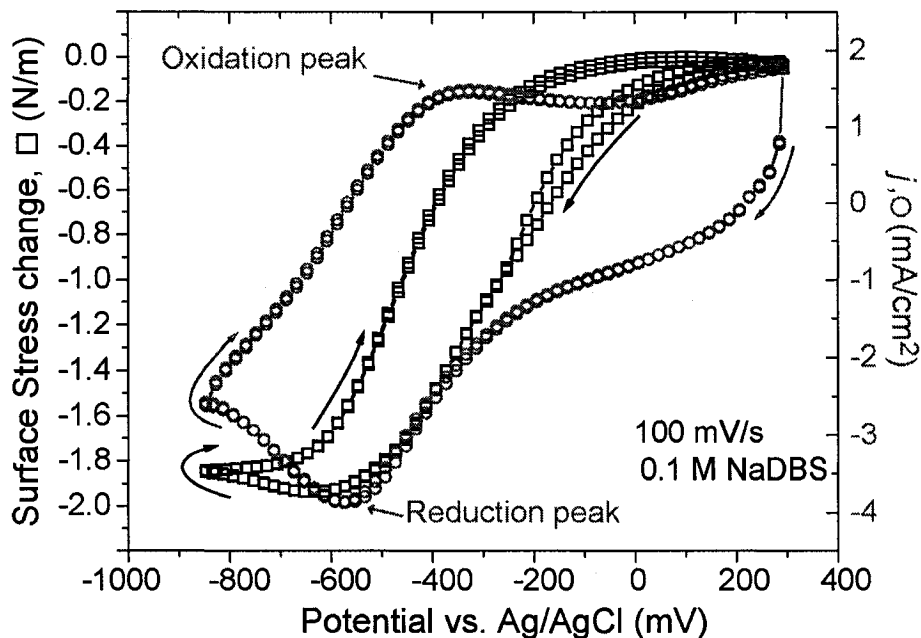


Figure 44: Surface stress (black square) and current (green circle) versus potential measured simultaneously during two consecutive cyclic voltammetric scans in 0.1 M NaDBS solution. The potential is swept at 100 mV/s between -850 mV and +300 mV. A change in surface stress of about -2 N/m is observed when going between the anodic and the cathodic peaks.

The reduced state is characterized by a change in charge of the polymer backbone (neutral) and a swelling of the polymer matrix, causing a bending of the microcantilever beam. Figure 44 shows the current and surface stress changes for a PPy-coated microcantilever during two oxidation/reduction cycles. Maximum microcantilever deflections are achieved when going between the anodic (oxidation) and the cathodic (reduction) peak potentials so that most of the bending is achieved within a 400 mV potential window. The correlation between the surface stress change and the redox potentials of the polymer film is in accordance with the mass changes observed by Bay et al. [139]. A surface stress

change of -2.0 ± 0.2 N/m is obtained between these two states, for the particular studied PPy(DBS) film in 0.1M NaDBS under the specific conditions used here.

5.2.3 Passivity of the backside

To demonstrate that the PPy(DBS) film is only deposited on the gold-coated side of the cantilever, the laser spot intensity reflected off the silicon back side of the cantilever beam was monitored. If the conducting polymer film is also located on the backside of the cantilever, the intensity of the reflected laser spot should change as a function of the electrochemical state. Indeed the PPy(DBS) film's color varies when electrochemically switched between its oxidized and reduced state. To get an appreciation of the expected intensity variation the intensity on the PPy(DBS)/gold-coated side was separately measured. Figure 45 shows the intensity fluctuation of both sides of the cantilever during redox reaction of the conducting polymer. On the PPy(DBS)/gold-coated side the change in intensity closely tracks the deflection of the cantilever (i.e. electrochemical state of the PPy(DBS) film).^{xxiii} However on the backside the intensity remains constant during electrochemical switching. Hence, it is inferred that the PPy(DBS) film only resides on the gold-coated side of the cantilever.

^{xxiii} The structure observed in the intensity plot is not fully understood. No systematic studies of the intensity change on the PPy(DBS) side were performed. The (what appears to be a) two step process may tentatively be associated with the intrinsic and extrinsic part of the swelling process discussed in section 5.2.1.

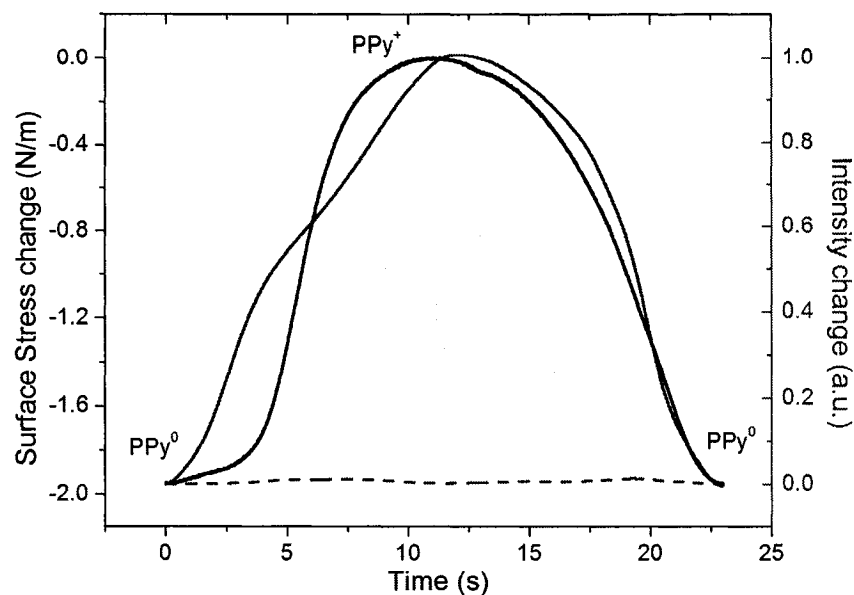


Figure 45: Surface Stress (in black) and intensity changes (in red) versus time measured during cyclic voltammetry in 0.1 M NaDBS. In red the variations in the reflected laser intensity off the microcantilever silicon back side (dash line) and off the PPy(DBS)/gold-coated side (solid line measured separately). These data indicate that the PPy(DBS) film is present only on the gold-coated side, since the variation in the reflected light intensity is not observed on the silicon side when the polymer is electrochemically switched between its reduced and oxidized states.

5.2.4 Redox inhibiting electrolyte

To ensure that the above measured surface stress is indeed due to a volume change of the polymer phase, a control experiment was performed. The PPy film was actuated by cyclic voltammetry in a redox inhibiting electrolyte while monitoring the surface stress response. The microcantilever deflection signal was studied under a 0.1 M TBABr, tetrabutylammonium bromide aqueous solutions.

TBA⁺ is a bulky cation, which will not incorporate into the polymer matrix to maintain electroneutrality in the film; hence preventing the redox process from occurring [140,141].

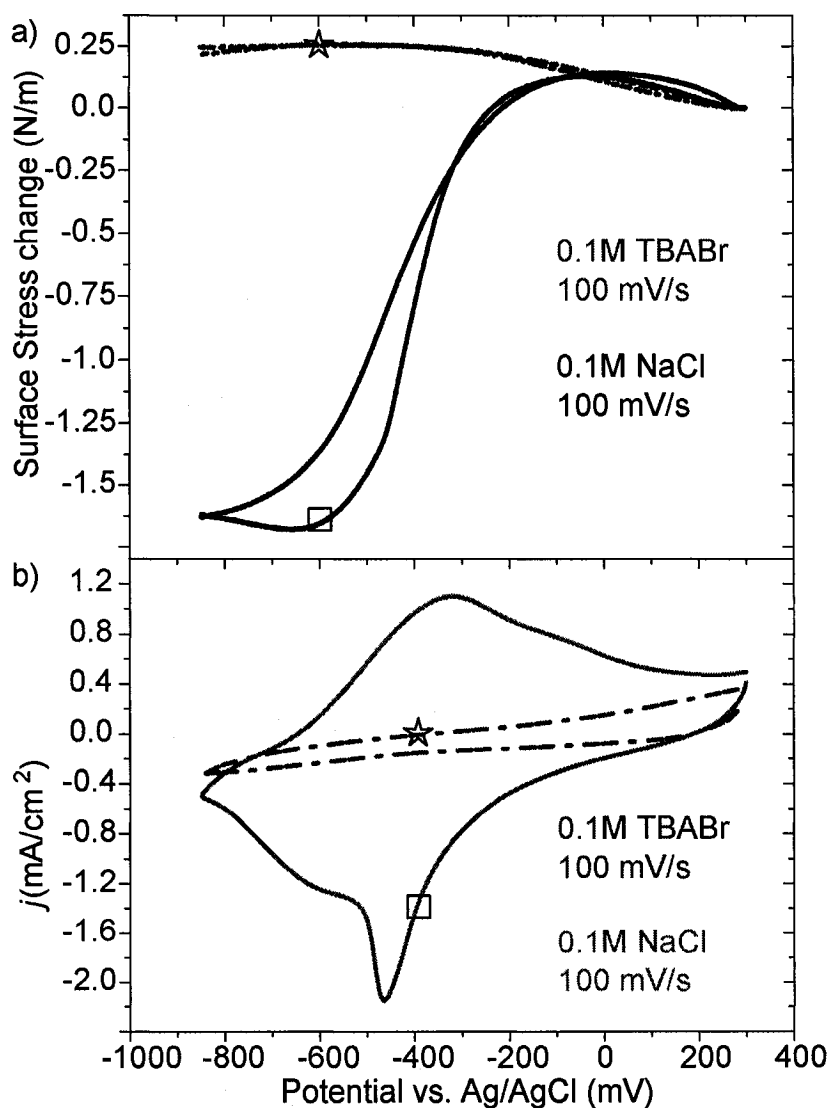


Figure 46: Control experiment. a) Initially the PPy film is actuated in 0.1 M NaCl (square), showing a compressive change in surface stress during swelling of the polymer. The same PPy(DBS) film is subsequently immersed in a *redox inhibiting* electrolyte, 0.1 M TBABr (star). No compressive stress is observed. b)

The CV in 0.1 M NaCl (square) shows the presence of the oxidation and reduction peaks, whereas in 0.1 M TBABr (star) the redox reaction is clearly suppressed.

Figure 46a shows the surface stress response of a PPy(DBS) film during potential cycling, between -850 mV and +300 mV at a scan rate of 100 mV/s, successively in 0.1 M NaCl (square), and 0.1 M TBABr (star). At first, the film is cycled in a 0.1 M NaCl electrolyte (square) showing a typical compressive change in surface stress of about -1.9 N/m, in phase with the oxidation and reduction peak potentials of the PPy(DBS) film as previously shown in Figure 44. Subsequently, the same film is immersed in a 0.1 M TBABr electrolyte. It is now unable to undergo reduction as shown by the disappearance of the redox peaks in the CV of Figure 46b(star). The swelling of the PPy(DBS) film is therefore inhibited and the microcantilever sensor does not experience a surface stress change as shown in Figure 46a(star). From this observation it can be asserted that the surface stress change measured during redox switching of PPy is indeed due to a change of volume of the conducting polymer matrix.

Nevertheless, the microcantilever is not completely motionless during potential cycling in TBABr electrolyte. As aforementioned, for potentials below -200 mV the microcantilever can be considered static. However, above that value it experiences a compressive change in surface stress of about -0.25 N/m. This motion, which is not believed to be related to a volume change of the polymer phase, can be attributed to the interaction between the Br^- anions and the gold substrate, underneath the PPy film. Indeed, the interaction of anions with a bare gold surface results in a charge-induced surface stress, as discussed by Haiss

[102] and Ibach [101]. Figure 47 shows the surface stress change of a bare gold-coated microcantilever when cycled in 0.1 M TBABr between -850 mV and +300 mV at a scan rate of 100 mV/s. A significant microcantilever deflection response is detected when a potential is applied to its surface. We observe that the surface stress curve is qualitatively similar to the one obtained for the PPy(DBS) film in TBABr. In fact, the two curves superimpose when scaled appropriately. The variation in magnitude is therefore attributed to the different surface areas of gold exposed in the two systems.

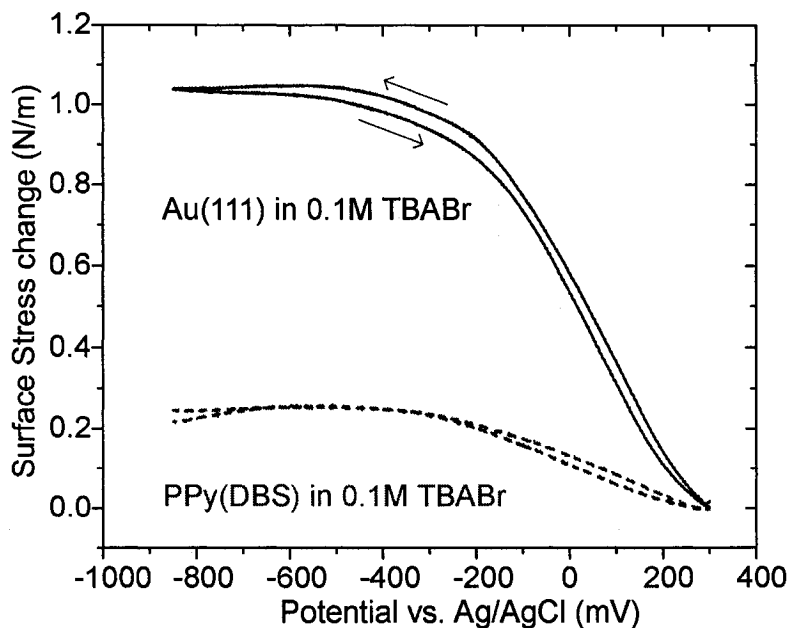


Figure 47: Surface stress measurement during Br^- anion adsorption (black straight line) on a bare gold-coated microcantilever in 0.1 M TBABr. A change in the surface charge density of the gold surface owing to the nature of the interaction with the anions is responsible for the compressive change in surface stress observed when going towards positive potentials. This graph elucidates the behavior of the PPy(DBS) bending response in 0.1 M TBABr (red dotted line, reproduced from Figure 46a)

The paths by which the anions reach the gold-coated microcantilever substrate remain indeterminate. The underlying gold substrate may be exposed to anions rendering the system sensitive to charge-induced surface stress through defects in the polymer matrix and/or at microcantilever edges where the PPy(DBS) film does not properly adhere to the microcantilever. Hence, in a PPy-gold coated microcantilever structure, one should expect a competing contribution to the measured surface stress from the gold substrate if it is exposed to the electrolyte.

Note that the mechanism of the redox process is more complex when small mobile anions, such as Br^- or Cl^- are present in the electrolyte and may be governed by both cations and anions of the supporting electrolyte [125]. Nevertheless, previous results of freestanding PPy(DBS) films [125,139,141] (i.e. no underlying gold) in small anion electrolytes indicate mainly cation motion and no apparent volume change associated with potential insertion/ejection [142,143] of the mobile anions. The small compressive change in surface stress observed above 0 mV in Figure 46(square) is therefore attributed to a charge-induced surface stress owing to anions interacting with the gold surface and not to a swelling of the PPy(DBS) due to insertion of Cl^- .

5.2.5 1st Reduction Scan

It is interesting to examine the first reduction scan in both the CV and the surface stress data of a freshly polymerized (uncycled) PPy film, as shown in Figure 48.

Before any electrochemical actuation takes place, the freshly prepared PPy⁺(DBS⁻) film is in its oxidized (doped) state. During a usual reduction process, the PPy film swells and the microcantilever experiences a compressive surface stress, i.e. bends away from the PPy-coated side. This is experimentally verified (see Figure 44) except for the very first reductive scan where the PPy-coated microcantilever experiences a significant tensile surface stress. This discrepancy is also observable in the CV (Figure 48b) as a shift in magnitude and potential of the first reduction peak. A tensile surface stress for the first reductive scan for two independent experiments performed in different electrolyte solutions (0.1 M NaDBS and 0.1 M NaCl) is shown in Figure 48a and Figure 49, with a similar value of about +1.5 N/m. There exists some variability in the tensile surface stress values obtained. Nonetheless, I have found an average value for 20 experiments of $+1.0 \pm 0.5$ N/m, irrespective of the electrolyte solution. It is the first time, to my knowledge, that such an observation has been quantified. In fact, other groups have observed little or no movement during the first reduction cycle on thicker PPy films [127,143,144] which implies that this tensile surface stress may be a function of the film thickness.

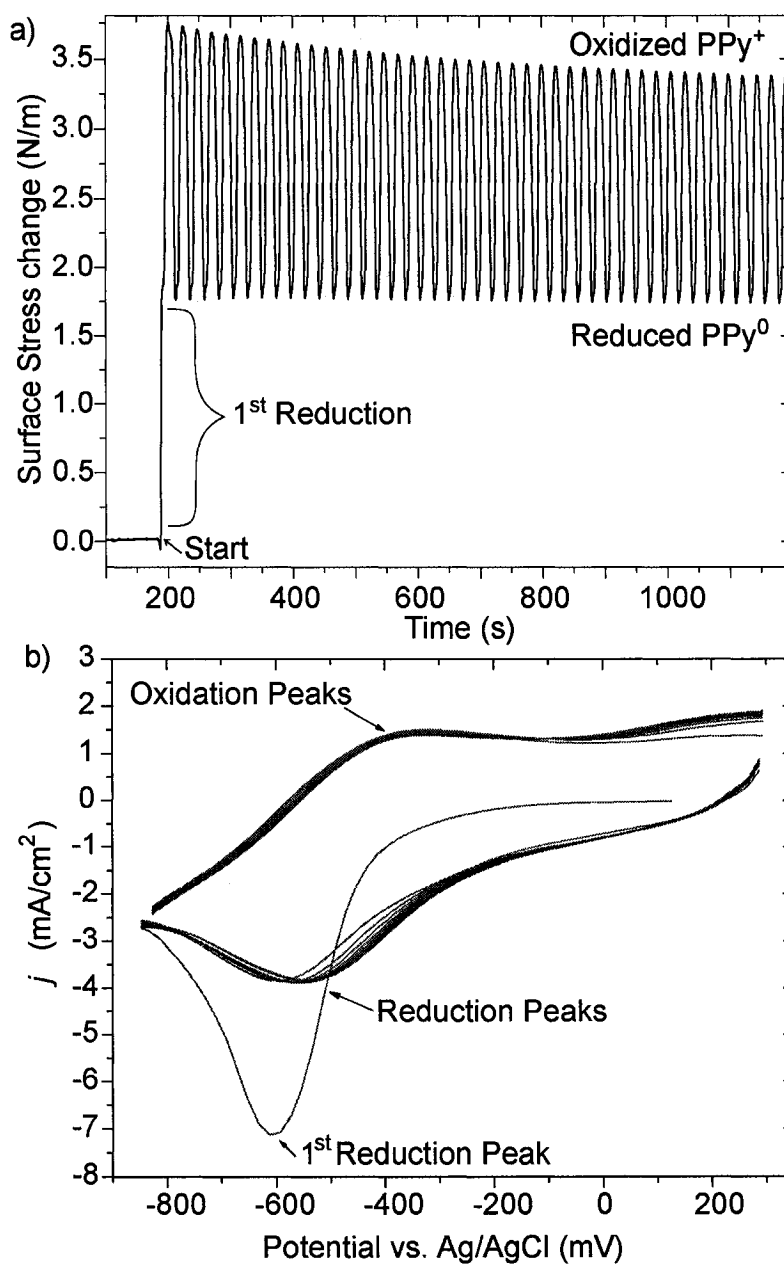


Figure 48: a) PPy-coated microcantilever deflections during the first 50 cycles in 0.1 M NaDBS, at a scan rate of 100 mV/s. The first reductive scan gives rise to a significant tensile surface stress. The subsequent reductive scans produce a compressive change in surface stress as expected from the swelling of the film. During multiple cycles, the peak to peak amplitude of the surface stress gradually decays. b) Corresponding cyclic voltammogram showing the anomalous first reduction peak and the subsequent oxidation and reduction peaks where the polymer is oxidized (PPy⁺DBS⁻) and reduced (PPy⁰DBS⁻Na⁺) respectively.

This anomalous first cathodic peak has been previously investigated, but its origins are still not completely understood. It is suggested that uncycled PPy films are irreversibly changed during the first reduction cycle. One hypothesis [127] is that channels are opened in the polymer matrix for the first time to allow diffusion of the cations (Na^+ and its solvation shell in this case). With our observation of a tensile surface stress we envisage that the fresh $\text{PPy}^+(\text{DBS}^-)$ film undergoes a non-reversible structural change on the microcantilever surface in which the polymer chains reorganize to accommodate the diffusion of cations. The PPy film thus shrinks and generates the observed tensile surface stress. Note that the magnitude of the tensile surface stress is comparable to the compressive surface stress observed during polymerization, so that during the first reduction cycle the system could be relieving some of its initial stress.

5.2.6 Life Time: Multiple Cycles

To study the lifetime of the microdevice, the long term actuation capability of the PPy film was examined over multiple cycles. Cyclic voltammetry experiments were conducted in two different electrolyte solutions, 0.1 M NaDBS and 0.1 M NaCl on more than 20 samples while monitoring the microcantilever deflections as a function of number of cycles.

Figure 48a shows a freshly polymerized PPy film actuated through 50 cycles from +300 mV and -850 mV (vs. Ag/AgCl) at a scan rate of 100 mV/s in 0.1 M NaDBS. Figure 48b is the corresponding cyclic voltammetric data, from which we

can identify the oxidation and reduction current peaks. The PPy(DBS)-coated microcantilever actuator reveals a decrease in its actuation capabilities. Indeed, the peak to peak surface stress amplitude, between the PPy⁺ and PPy⁰ states, decays with increasing cycle number as shown in Figure 50. This loss in actuation amplitude is quite severe and is indicative of a delamination of the polymer film as will be discussed later.

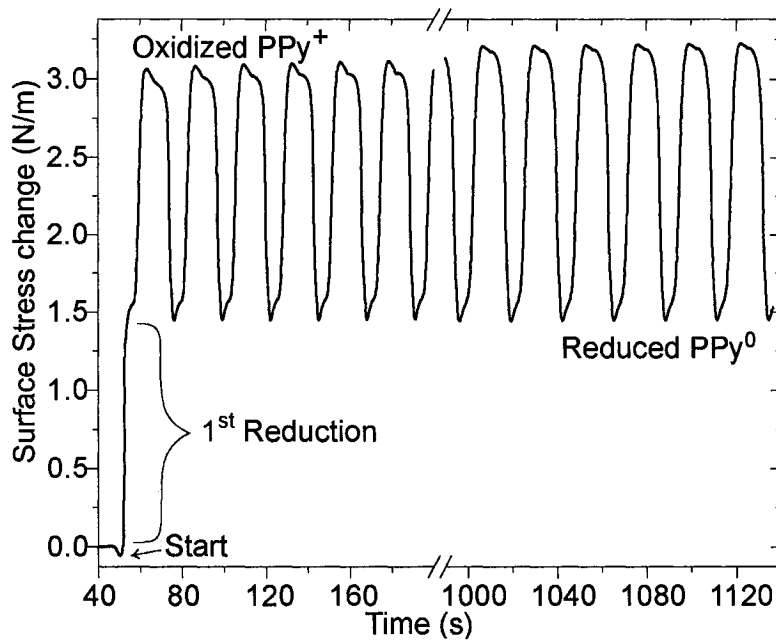


Figure 49: PPy(DBS)-coated microcantilever deflection during multiple cycles in 0.1 M NaCl at 100 mV/s. The first reductive scan also gives rise to a significant tensile surface stress. During multiple cycles, the peak to peak amplitude of the surface stress is stable over 500 cycles.

Similar experiments were conducted in 0.1 M NaCl. Figure 49 shows the microcantilever deflections for a series of actuations between +300 mV and -850

mV at a scan rate of 100 mV/s. In this case, the peak to peak surface stress amplitude does not gradually decay but rather slightly increases before stabilizing. The surface stress reaches a value of about 1.9 N/m which is relatively stable over more than 500 actuation cycles. This value is comparable in magnitude with the initial surface stress observed in NaDBS electrolyte. However, for this microcantilever-based actuator system there is an obvious difference in the long term actuation capabilities of PPy(DBS) films cycled either in NaDBS or NaCl electrolytes as shown by Figure 50.

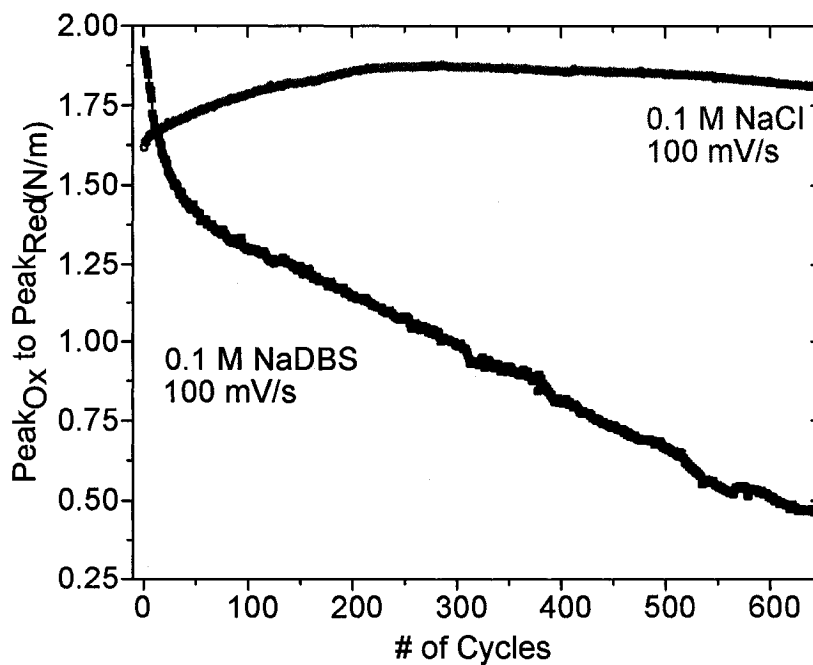


Figure 50: Surface stress peak to peak amplitude between the oxidized and reduced state of the polymer taken from the data of Figure 48 and Figure 49. In black, the PPy(DBS) film in 0.1 M NaDBS shows a gradual loss in amplitude. In grey, the PPy(DBS) film in 0.1 M NaCl shows a slight increase and stabilization of the actuation amplitude.

To examine in more depth the impact of the nature of the electrolyte on the long term actuation capabilities of the PPy(DBS) film, additional experiments were conducted in another surfactant (0.1 M NaDS - sodium dodecyl sulfate) and halide (0.1 M LiCl) based-electrolyte. Cycling the film in NaDS revealed a similar loss in actuation amplitude as in the NaDBS case. However, contrary to the results obtained in surfactant-based electrolytes, the actuation amplitude of the PPy(DBS) film cycled in LiCl displayed no sign of instant decline. Consequently, the surfactant property of the electrolyte is likely responsible for the degradation and loss in actuation amplitude of the polymer film. It is well established in the literature that for a PPy(DBS) film in 0.1 M NaDBS only the Na⁺ ions and their hydration shells participate in the redox process of the polymer [127]. The bulky DBS⁻ ions within the polymer are trapped and cannot diffuse in or out of the polymer matrix. Similarly the DBS⁻ ions of the NaDBS supporting electrolyte cannot enter the PPy(DBS) film [143]. Nevertheless, their presence in the solution has a clear impact on the actuation capabilities of PPy(DBS) films. DBS anions are amphiphilic molecules which greatly reduce the surface tension of the aqueous electrolyte. The NaDBS electrolyte is therefore envisioned, as the film continuously swells and shrinks, to progressively insert itself in between the PPy film and the gold surface. As a result, the film gradually delaminates from the microcantilever structure generating the observed weaker actuation. This delamination effect can be seen in Figure 51 where the evolution of the PPy-coated microcantilever actuator responses, under multiple cycles in 0.1 M NaDBS, is presented.

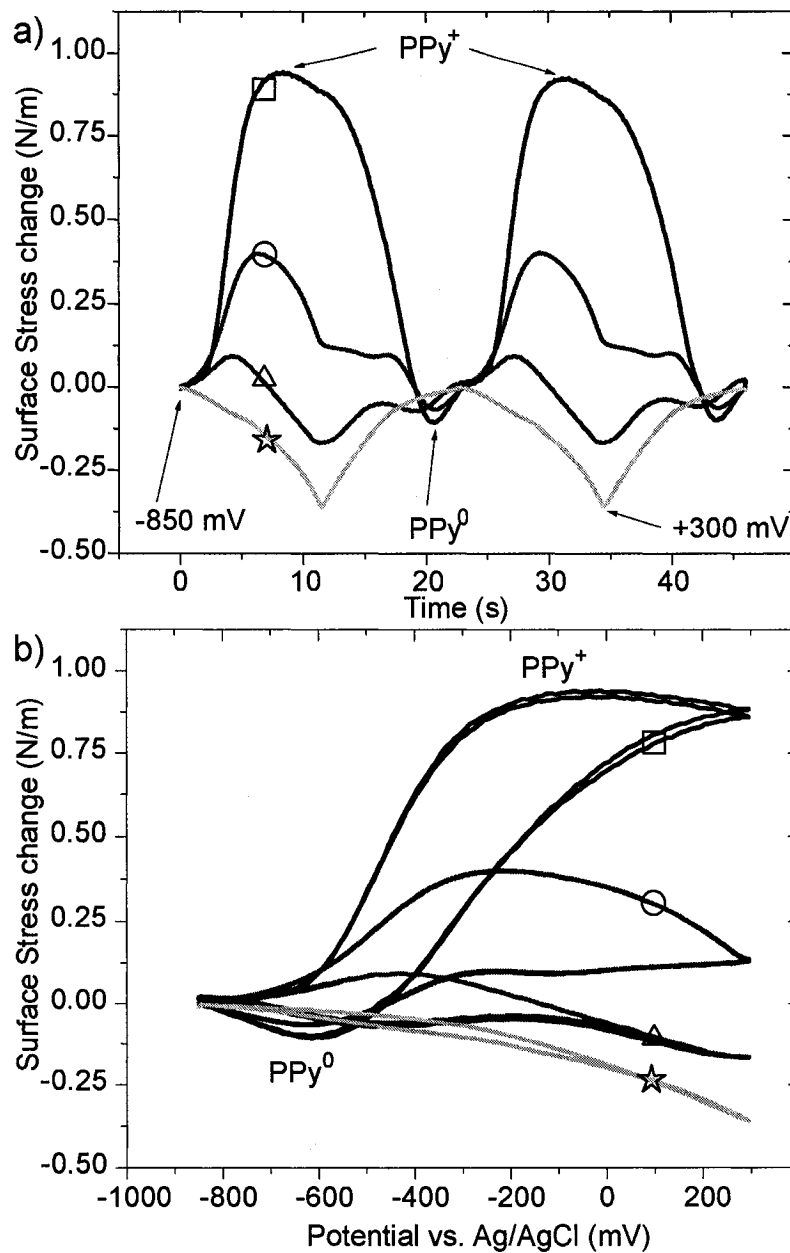


Figure 51: Microcantilever deflection in 0.1 M NaDBS at 100 mV/s. a) Bending response of the PPy-coated microcantilever actuator for a polymer film cycled 100 times (square), after 500 cycles (circle), after 800 cycles (triangle) and for more than a 1000 cycles (star). Ultimately the PPy film is completely delaminated from the gold-coated microcantilever. b) Bending response as a function of potential. The square, circle, triangle and star labels represent the same data as in a). As we are only measuring a change in surface stress; the zero of the y-axis was arbitrarily chosen at -850 mV.

Figure 51 shows the PPy film actuation for increasing number of cycles. Figure 51(square) represents a PPy film within the first 100 cycles, Figure 51(circle) is after 500 cycles, Figure 51(triangle) after 800 cycles and Figure 51(star) more than a thousand cycles. We can observe from these graphs that not only the amplitude of actuation decreases with increasing cycling, but also that the qualitative nature of the deflection data evolves. Indeed, after only a few hundred cycles the maximum surface stress signal is no longer in phase with the oxidation and reduction current peaks. As the PPy film starts to delaminate with repeated cycling, a greater gold surface area comes in contact with the electrolyte. The interaction between the electrolyte and the gold surface begins to be more noticeable and eventually dominates. Ultimately excessive cycling results in a complete delamination of the PPy film from the microcantilever. When the charge-induced surface stress generated by a bare gold-coated microcantilever is subtracted from the degraded response of the PPy-coated microcantilever of Figure 51(circle), we obtain the original bending response of a fresh PPy-coated microcantilever actuator as shown in Figure 52. Hence an extensive cycling of a PPy(DBS) film in 0.1 M NaDBS gradually delaminates the PPy film from the microcantilever, exposing the underlying gold substrate to the electrolyte.

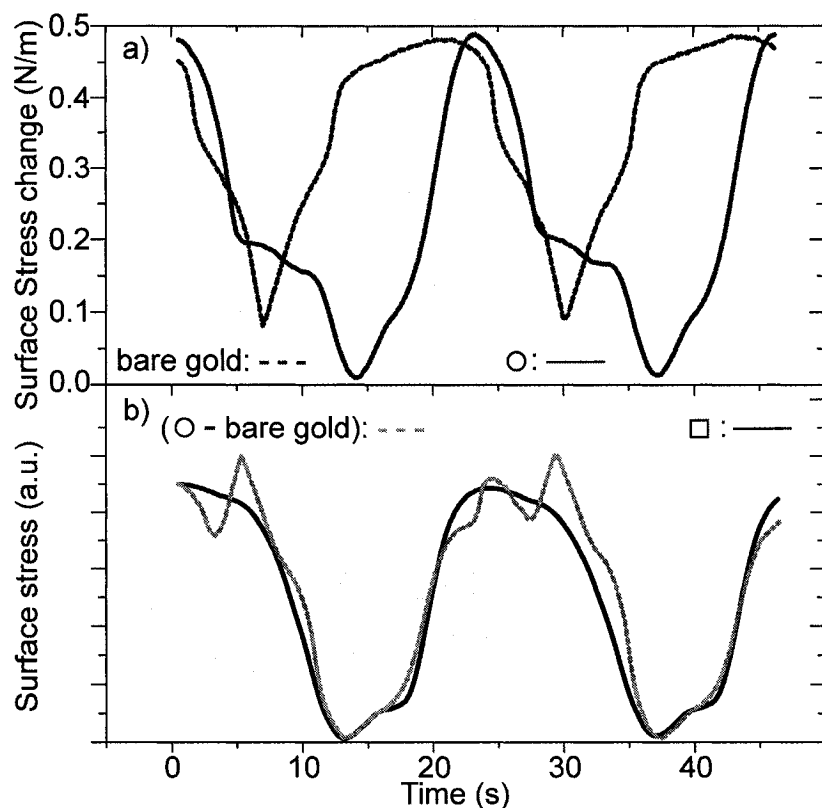


Figure 52: a) The surface stress induced on a bare gold coated microcantilever (red dotted line) in 0.1 M NaDBS is superimposed with the degraded bending response of a PPy(DBS) film cycled 500 times (blue full line, taken from Figure 51circle). b) Bending response from a fresh PPy(DBS) film (black full line, taken from Figure 51square) superimposed with the differential signal of a degraded PPy(DBS) film and a bare gold coated microcantilever in 0.1 M NaDBS. The overlap is striking, so that the degraded signal is a combination of fresh PPy(DBS) film actuation and charge-induced surface stress owing to the interaction of the electrolyte and the gold substrate.

To determine the contribution of this competing surface stress generated by the gold substrate to the loss in actuation, I have subjected the PPy(DBS) film to a narrowed potential window. As it was previously shown, in the potential window where the polymer is in its oxidized state, any gold surface exposed generates an

opposing surface stress owing to its interaction with anions. To take away this effect, I have therefore performed cyclic voltammetry from -850 mV to -200 mV in 0.1 M NaDBS at a scan rate of 100 mV/s on freshly polymerized PPy(DBS) films. The PPy(DBS) films, despite exhibiting a slower decay rate, showed a similar immediate loss in actuation amplitude. This establishes that anion interaction with the gold substrate is not the driving force of this instant shortfall in actuation in NaDBS electrolyte, but only a consequence of the delamination.

To improve the lifetime of the PPy(DBS) microactuator, the adhesion of the polymer film with the metal substrate needs to be enhanced. Several approaches are being considered such as chemically attaching the PPy film to the gold surface via thiol-modified pyrrole units [145] more adapted electrochemical switching techniques [146], electrolyte solutions, and roughening the gold to increase the mechanical interlocking [133,147]. Note, however, that a rougher surface will render the device more sensitive to charge-induced surface stress in the metal [148].

5.3 Summary

A microactuator device was constructed by electrodepositing a PPy(DBS) film onto one side of a gold-coated AFM microcantilever. I have demonstrated that the volume change of the PPy(DBS) film with respect to the gold-coated microcantilever is responsible for the mechanical motion observed. A

compressive change in surface stress of about -2 N/m was measured when the conducting polymer was electrochemically switched between its oxidized (PPy⁺) and neutral (PPy⁰) state by cyclic voltammetry. Interestingly, the presence of a substantial tensile surface stress was observed during the first anomalous cathodic scan which was attributed to a non-reversible structural change of the freshly polymerized PPy film. The lifetime of the microactuator device was examined in both 0.1 M NaDBS and 0.1 M NaCl electrolytes. The surfactant nature of the electrolyte (DBS molecules) was likely responsible for the degradation and delamination process of the PPy film. Most importantly I have identified two main competing origins of surface stress acting on the PPy(DBS)/gold-coated microcantilever. For the most part a purely mechanical source, due to the volume change of the PPy(DBS) polymer with respect to the gold-coated microcantilever, strains the gold surface. Additionally, there is a charge-induced surface stress from the interaction of anions with gold exposed to the electrolyte. These findings should be considered in the design and performance optimization of future conducting polymer-covered microcantilever-based actuator devices.

6 Summary and Outlook

6.1 Summary

The mechanisms responsible for the mechanical motion of microcantilever sensors during *adsorption* and *absorption* processes were the focus of the present study. Surface stress changes generated by sub-monolayer ionic *adsorption* on gold surfaces and by electromechanical-induced *absorption* in thin polymer films were measured. The study of these simple model systems led to a general understanding of the sensor's response and provided an insight into the physical origin of the measured surface stress.

In chapter 2, this thesis reported the development of a differential microcantilever-based system capable of measuring surface stress changes at the solid-liquid interface under electrochemical control. The system is composed of two microcantilever sensors. The first *active* microcantilever serves as the working electrode (in a conventional three-probe electrochemical cell configuration) and as the mechanical transducer (bending of the microcantilever)

yielding simultaneous, real-time, *in situ* measurements of the current (charge) and interfacial stress changes. The second *reference* microcantilever serves as a reference sensor to detect any unwanted cantilever deflection resulting from temperature variations, mechanical vibrations and/or uncontrolled chemical reactions. This micromechanical cantilever sensor instrument achieves a deflection limit of 0.2 nm, which translates to a surface stress sensitivity of 1×10^{-4} N/m and a dynamic range of 5×10^5 .

A fast, simple and clean technique for isolating the electrical contact made to the microcantilever from the electrolyte solution was presented. A method for creating a working electrode with a reproducible area of 1.0 mm^2 was also implemented which allowed for a quantitative measure of the current density, and therefore knowledge of the charge consumed per unit area. A 3% reproducibility in the thickness of electrochemically deposited polypyrrole films was achieved.

The following chapter developed a procedure to convert the instrument output signal into an actual cantilever deflection. Two methodologies were presented and compared. The geometrical approach which provides a simpler more rapid calibration of the instrument was found to be only 6% off the interferometric calibration. When the cantilever to PSD distance is frequently modified for practical experimental needs it should therefore be the method of choice. In addition, a novel methodology used to convert the cantilever deflection into a surface stress was developed. This methodology overcomes some limitations encountered when using the more commonly used Stoney's formula by eliminating the need to know the cantilever material's elastic modulus and makes

use of readily measured parameters. Ultimately, this method allows for surface stress changes to be measured with an accuracy of 10%.

In Chapter 4, the surface energy and surface stress change of a gold-coated microcantilever, in an HClO_4 electrolyte, were simultaneously measured. These measurements revealed that for solid electrodes the two thermodynamic parameters are significantly different and should not be substituted. A potential-induced change in surface stress of -0.55 ± 0.06 N/m was measured when cycled from +200 mV to +700 mV (vs. Ag/AgCl), in a 0.1 M HClO_4 electrolyte solution. Over the same potential range, the surface energy variation was shown to be smaller by one order of magnitude. It was further shown that the surface energy versus potential curve revealed the expected parabolic shape whereas in the potential representation the surface stress was dominated by the change in differential capacity of the interface. This was corroborated by the observation of a linear relationship between surface stress and surface charge density. Interestingly, the entire interface, including the liquid part, was found to contribute to the measured surface stress. In fact, when the effect of anion adsorption was excluded, the sole contribution from the metal to the surface stress was observed to vary smoothly with potential and to qualitatively resemble the surface energy change.

The repulsive electrostatic interactions between adsorbed species alone cannot account for the observed surface stress. A simple model of bond charge redistribution provided an effective qualitative description of the surface stress change at the metal-electrolyte interface. The origin of the surface stress change

was understood by the variation in electron density at the surface which alters the inter-atomic bonds' strength between surface atoms, while the strength of the interaction of charged adsorbates with the surface was found to be mostly responsible for the fine structure of the surface stress curve.

Lastly, the surface stress measurements on polycrystalline gold-coated microcantilevers were found to compare exceptionally well with results obtained on single crystals by Ibach et al. and Haiss et al. This demonstrated that grain boundaries and grain size as well as the adhesion of the evaporated thin film had insignificant consequences on the surface stress change induced by anion adsorption. On the contrary, discontinuities in the gold film had a large impact on the magnitude of the measured surface stress. In addition, the cleanliness of the metal film significantly influenced both quantitatively and qualitatively the surface stress response at the solid-liquid interface, and possibly explained some previously reported controversial microcantilever results.

In the final chapter of this thesis, the surface stress change induced by cation absorption into a 300 nm thick electrodeposited dodecyl benzenesulfonate-doped polypyrrole film, PPy(DBS), was examined. The cantilever's mechanical motion was investigated during electrochemical switching of PPy(DBS) thin films by cyclic voltammetry. The volume change of the polymer phase with respect to the gold-coated microcantilever was demonstrated to be responsible for the mechanical motion observed. A compressive change in surface stress of approximately -2 N/m was measured when the conducting polymer was

electrochemically switched between its oxidized, $\text{PPy}^+(\text{DBS}^-)$, and neutral swollen, $\text{PPy}^0(\text{DBS}^-\text{Na}^+)$, state.

This study provided new insight into the actuation mechanism and in particular quantified for the first time the surface stress evolution during the anomalous first reduction scan. An average tensile surface stress change of $+1.0 \pm 0.5$ N/m was measured which was attributed to a non-reversible structural change of the freshly polymerized film. Finally, a competing interaction to the actuation mechanism of the cantilever was identified: the $\text{PPy}(\text{DBS})$ -covered gold-coated microcantilever is susceptible to charge-induced surface stress owing to the interaction of anions of the supporting electrolyte with any exposed underlying gold. This observation revealed that the actuation response of $\text{PPy}(\text{DBS})$ -covered cantilevers is very sensitive to defects in the film as well as delamination of the polymer from the cantilever.

Overall, from the experimental data on the variation of the surface stress with electrode potential presented in this thesis, it was revealed that:

- During adsorption processes at the solid-liquid interface, the surface stress change is mainly governed by the change in electronic structure of the metal substrate surface atoms (similar as in the gas phase). The repulsive interaction of adsorbed species cannot qualitatively account for the measured surface stress. However the strength of the interaction of the adsorbates with the surface is responsible for the structure of the surface stress response.

Conversely,

- During absorption it is the swelling of the polymer phase with respect to the gold-coated substrate that accounts for the mechanical motion of the cantilever-based sensor.

6.2 Outlook

The advent of atomic force microscopy (AFM) and the advances in micro-electromechanical systems (MEMS) have allowed AFM cantilevers to emerge as a promising new class of biochemical sensors. Moreover, microfabricated arrays of cantilevers can easily and fully be integrated into laboratory-on-a-chip type devices for μ TAS (Micro Total Analysis Systems) applications. This unparalleled opportunity for the development and mass production of extremely sensitive, fast and low-cost sensors for real time in situ sensing of many chemical and biological species has engendered many commercial cantilever-based sensor platforms.

To date, several companies have commercialized cantilever-array sensor instruments. The first to offer a product on the market in March of 2002 was Veeco [149] with the Scenris[®] system, which consists of an instrument capable of monitoring the response of 8 cantilevers in parallel. Shortly after, Concentris [150] offered the Cantisens[®] research cantilever sensor platform, as well as Protiveris [151] who presented the VeriScan 3000 System[®] (offering the possibility of monitoring 64 cantilevers in parallel); both also equipped with optical read-out schemes. Furthermore, Cantion [152] proposed an instrument, the Canti-Chip-4[®] composed of four piezo-resistive cantilevers with an integrated

electrical read-out system. Other companies are interested in developing integrated cantilever-based sensing platforms, such as Luna Innovation [153], Exxon-Mobil, etc... This continually growing commercial development of cantilever-based sensors suggests that they might play an important role in the immediate future of nanotechnology. Unfortunately, each of these cantilever-based sensor instruments is faced with several difficulties, including the complexity of the sensor's response and lack of understanding of the origin of the measured surface stress. A potential end-user requires a reliable output signal from a "black box" instrument. However, in cantilever-based sensing measurements the sensor itself is often the subject of the experiment. For this reason, Veeco already withdrew its instrument from the market and other companies are increasing their collaboration with various university research groups to extend the range of successful applications with their patented technologies.

It is clear that if cantilever-based sensors are to become a viable technology for medical diagnostics or other practical applications, a better understanding of the origin of the measured surface stress must be developed. This will enable the optimization of sensor performance by suitably tailoring the properties of the sensing layer, favoring interactions that will generate the maximum surface stress response.

The experiments described herein aimed at understanding the mechanisms that provide a sensor response during adsorption and absorption sensing applications are essential in eventually improving the sensitivity and financial marketability of cantilever-based sensing technology. The adsorption results on gold-coated

cantilevers revealed that the measured surface stress signal is dominated by the response of the metal substrate. This interesting finding suggests that cantilever-based sensors should be tailored to take advantage of this effect. The sensing surface, during molecular adsorption experiments, should be designed to directly influence the substrate's electronic structure rather than relying on electrostatic repulsion or steric hindrance between adsorbates. From surface science studies it is known that adsorption of molecules onto a surface modifies the work function of the surface. Actually, the potential-induced surface stress experiments which were presented can be interpreted as varying the work function of the cantilever, since the electrode potential (E) and the work function (ϕ) differ only by a constant (i.e. $\phi = Ee_0 + c$, where e_0 is the elementary charge). These experiments therefore provided a direct indication that a work function modification can produce a significant surface stress change.

While most cantilever studies have focused on thiol chemistry to link the biomolecular probe to a gold-coated surface, this linkage is only structural and lacks an essential orbital conduit for electrons and/or holes [154]. An alkanethiol SAM is essentially a protecting, insulating layer between the metal substrate and the adsorbates. The potential-induced surface stress results on thiol-modified cantilevers demonstrated that the sensor response is significantly reduced when the electronic structure of the metal substrate is not directly influenced (because of the low capacity). Alternative strategies for tethering molecular probes on the sensor surface should be investigated which would be characterized by a strong electronic coupling between the metal substrate and the adsorbates. Inspired by

the field of molecular electronics, it is envisaged that a sensing layer can be designed based on ligands tethered to the cantilever sensor's surface which would effectively act as molecular switches to gate surface charge and only specific biomolecular recognition events would trigger electronic structure modifications of the sensor substrate. Such new sensing architectures will improve the sensitivity and performance of MEMS/NEMS devices for chemical and biological sensing applications.

Apart from being important for the future development of cantilever-based sensing technologies, the results of this thesis revealed that cantilever surface stress sensors combined with electrochemistry can be used to study fundamental aspects of the thermodynamics of the solid-liquid interface. The work presented in Chapter 4 confirmed that, for solid electrodes, surface energy and surface stress are two different thermodynamic parameters. However, it was observed that for thiol-modified gold electrodes (and for *dirty* gold), the surface stress change as a function of potential curve was parabolic which qualitatively resembled the change in surface energy. This interesting observation can be used to extract more fundamental understanding on the individual contribution, to the interfacial stress, of the metal and the liquid part of the interface. Certainly, more work dedicated to understanding the shape of the surface stress curve with potential will add to this comprehension.

In addition, the study presented in Chapter 5 revealed the actuation and failure mechanism of conjugated polymer-based actuators. These MEMS devices actuated by electroactive polymers are susceptible to loss of adhesion and to

defects in the polymer films which expose the gold substrate and render the actuator device sensitive to charge-induced surface stress (owing to the interaction of ions with the charged substrate). This effect can be somewhat evaded by a suitable choice of electrolyte and by electrodepositing better films. However, when the size of the device is scaled down to nanometer dimensions as in the case of NEMS actuators, the polymer film thickness will significantly decrease and the effect of the defects in the film will become more critical to the actuation response. In such a case, the role of defects (exposed substrate) should probably be integrated in the design of polymer-based nanoactuator devices.

Appendix

➤ *Error Propagation in the Surface Stress Calculation*

Recall the equation to convert the PSD signal into a surface stress change, $\Delta\sigma$:

$$\Delta\sigma = \frac{4}{3(1-\nu)} \cdot \frac{l}{wt} \cdot k \cdot \Delta z = \frac{4}{3(1-\nu)} \cdot \frac{l}{wt} \cdot k \cdot \frac{l_{eff}}{4L} \cdot \Delta S \cdot \left(\frac{l}{l_{eff}}\right)^2$$

The error in $\Delta\sigma$, $\delta(\Delta\sigma)$, can be estimated by calculating the following relation:

$$\frac{\delta(\Delta\sigma)}{\Delta\sigma} = \sqrt{\left(\frac{\delta k}{k}\right)^2 + \left(\frac{\delta t}{t}\right)^2 + \left(\frac{\delta L}{L}\right)^2 + \left(\frac{\delta l_{eff}}{l_{eff}}\right)^2 + \left(\frac{\delta w}{w}\right)^2 + 3\left(\frac{\delta l}{l}\right)^2 + \left(\frac{\delta \Delta S}{\Delta S}\right)^2 + \left(\frac{\delta(1-\nu)}{(1-\nu)}\right)^2}$$

Each error term in the above equation is sorted by decreasing order of importance.

The following precision is achieved in the measurement of next parameters:

- Spring constant, $k = 0.035 \pm 0.002$ N/m
- Thickness, $t = 1.2 \pm 0.05$ μm
- PSD-cantilever distance, $L = 24 \pm 1$ mm
- Cantilever effective length, $l_{eff} = 325 \pm 5$ μm
- Cantilever width, $w = 35.0 \pm 0.1$ μm
- Cantilever length, $l = 350.0 \pm 0.1$ μm
- PSD signal, $\Delta S = 1 \pm 0.0001$ V (in a 0-3 Hz bandwidth by performing time averaging, otherwise the raw PSD signal has a 1mV noise level, which ranks it just below the error on the width)

- Poisson's ratio, ν , can have a fixed known value for single crystal silicon cantilevers [62] or can represent the most significant source of error for silicon nitride cantilevers, where $\nu = 0.25 \pm 0.02$

Ultimately by substituting these values we obtain:

$$\frac{\delta(\Delta\sigma)}{\Delta\sigma} \sim 0.1$$

The surface stress change can therefore be measured with an accuracy of 10 %.

➤ *Refraction at the Optical Window*

From Figure 18 we can write:

$$2\theta_1 = \frac{(\Delta S - y)}{(L - d)} = \frac{\Delta S}{L} \quad \text{Equation A-1}$$

$$2\theta_2 = \frac{(\Delta S' - y)}{(L - d)} \quad \text{Equation A-2}$$

We have assumed small deflection so that $L \approx L \pm \Delta z$, since $L \gg \Delta z$.

According to Snell's law and using the small angle approximation we have:

$$\frac{\sin \theta_1}{\sin \theta_2} \cong \frac{\theta_1}{\theta_2} = \frac{n_{air}}{n_{liquid}} = \frac{1}{n_{liquid}} \quad \text{Equation A-3}$$

Replacing Equation A-1 and Equation A-2 into Equation A-3 we obtain:

$$\frac{1}{n_{liquid}} = \frac{\Delta S - y}{\Delta S' - y} \quad \text{Equation A-4}$$

$$y = \frac{d}{L} \Delta S \quad \text{Equation A-5}$$

Solving Equation A-4 for $\Delta S/\Delta S'$ and using Equation A-5 we get:

$$\frac{\Delta S}{\Delta S'} = \frac{1}{n_{liquid}} \cdot \frac{1}{\left(1 - \frac{d}{L} + \frac{d}{n_{liquid}L}\right)} \quad \text{Equation A-6}$$

Using $n_{liquid} = 1.33$ (water) and for the particular optical beam deflection arrangement of the instrument presented herein ($L = 24$ mm and $d = 7$ mm) we have:

$$\Delta S = \frac{\Delta S'}{1.24} \quad \text{Equation A-7}$$

Note that to simplify the derivation, a normal angle of incidence was assumed for the incident laser beam, which is approximately the case for the instrument presented herein. For a more general derivation see reference [155].

➤ *Derivation of the Shuttleworth equation [102]*

Shuttleworth equated the energy associated with the two reversible path depicted in Figure A.1. In the first path ($a \rightarrow b \rightarrow c$), the solid is cut into two unstrained pieces and subsequently these pieces are elastically strained. In the second path ($a \rightarrow d \rightarrow c$), the solid is first elastically strained and then the strained solid is cut. If the two paths are assumed to be reversible, the corresponding energies must be equal ($W^1_C + W^1_S = W^2_S + W^2_C$). Hence we can write:

$$W^2_C - W^1_C = W^1_S - W^2_S \quad \text{Equation A-8}$$

The left-hand side of this equation represents the difference in total surface free energy ($\gamma(\epsilon)A(\epsilon) - \gamma_0A_0$) whereas the right-hand side, by definition, represents the

work performed against the surface stress ($\int A_0 \sigma_{ij} d\varepsilon_{ij}$). For an infinitesimal elastic strain, Equation A-8 can be expressed in differential form as:

$$d(\gamma A) = A_0 \sigma_{ij} d\varepsilon_{ij} \quad \text{Equation A-9}$$

With $d(\gamma A) = \gamma dA + A d\gamma$ and $dA = A_0 \delta_{ij} d\varepsilon_{ij}$ (where δ_{ij} is the Kronecker delta), the Shuttleworth equation follows:

$$\sigma_{ij} = \gamma \delta_{ij} + \partial\gamma/\partial\varepsilon_{ij} \quad \text{Equation A-10}$$

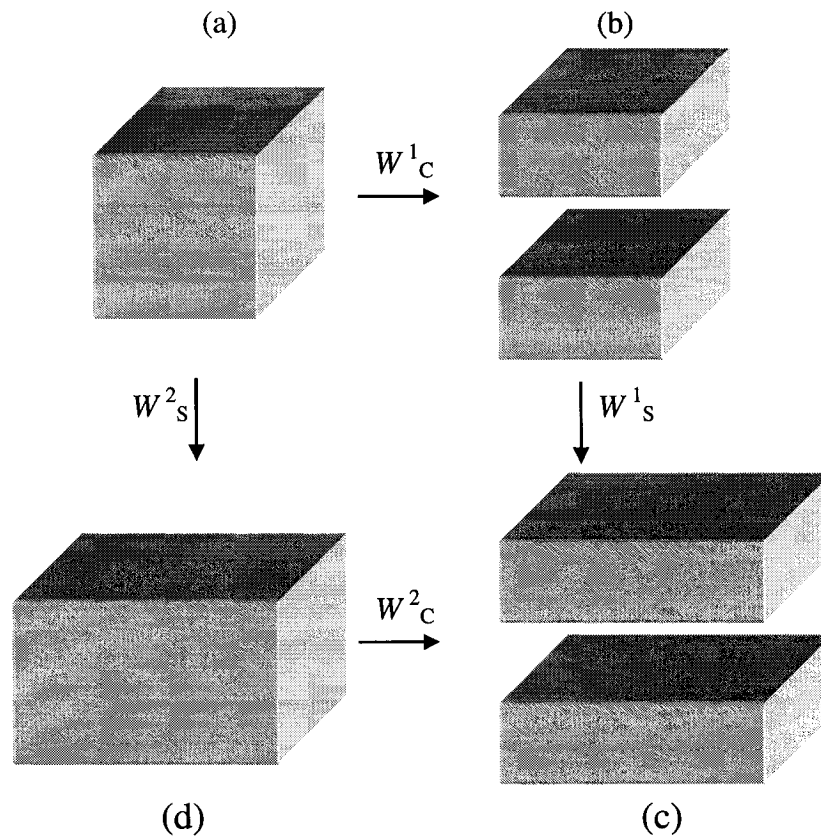


Figure A.1: Schematic illustration of two reversible paths to create strained surfaces with a total area A from an unstrained volume element. Path 1: $a \rightarrow b \rightarrow c$; path 2: $a \rightarrow d \rightarrow c$. [Reproduced from reference 102]

➤ *List of Refereed Publications*

- ❑ Beaulieu L. Y.; Godin, M.; Laroche O.; **Tabard-Cossa V.**; Grütter, P.; (2006) "*Calibrating laser beam deflection systems for use in atomic force microscopes and cantilever sensors*" Applied Physics Letters 88, 083108.
Supporting digital resources:
http://www.physics.mun.ca/beaulieu_lab/papers/cantilever_analysis.htm

- ❑ **Tabard-Cossa, V.**; Godin, M.; Burgess, I.; Lennox, R. B.; Grütter, P.; (2005) "*Redox-Induced Surface Stress of Polypyrrole-based Actuators*" Journal of Physical Chemistry B 109: 17531-17537.

- ❑ **Tabard-Cossa, V.**; Godin, M.; Beaulieu, L.Y.; Grütter, P.; (2005) "*A Differential Microcantilever-Based System for Measuring Surface Stress Changes Induced by Electrochemical Reactions*" Sensors and Actuators B. 107: 233-241.

- ❑ Godin, M.; Williams, P.J.; **Tabard-Cossa, V.**; Laroche, O.; Beaulieu, L.Y.; Lennox, R. B.; Grütter, P.; (2004) "*Surface Stress, Kinetics, and Structure of Alkanethiol Self Assembled Monolayers*" Langmuir. 20: 7090-7096. *Featured on the Langmuir journal cover.*

- ❑ Quist, F.; **Tabard-Cossa, V.**; Badia, A.; (2003) "*Nanomechanical Cantilever Motion Generated by a Surface-Confined Redox Reaction*" J. Phys. Chem. B. 107: 10691-10695.

- ❑ Godin, M.; Laroche, O.; **Tabard-Cossa, V.**; Beaulieu, L.Y.; Grütter, P.; Williams, P.J.; (2003) "*Combined in situ Micromechanical Cantilever-Based Sensing and Ellipsometry*" Review of Scientific Instruments. 74: 4902-4907.

- ❑ Godin, M.; **Tabard-Cossa, V.**; Grütter, P.; Williams, P.; (2001) "*Quantitative Surface Stress Measurements using a Microcantilever*" Applied Physics Letter. 79: 551-553.

References

- [1] A. Hulanicki, S. Geab, and F. Ingman, *Pure & Applied Chemistry*, 63, 1247-1250 (1991)
- [2] Brett J. Doleman and Nathan S. Lewis, *Sensors and Actuators B*, 72, 41-50 (2001).
- [3] M.K. Baller, H.P. Lang, J. Fritz, Ch. Gerber, J.K. Gimzewski, U. Drechsler, H. Rothuizen, M. Despont, P. Vettiger, F.M. Battiston, J.P. Ramseyer, P. Fornaro, E. Meyer, H.-J. Güntherodt, *Ultramicroscopy*, 82, 1-9 (2000).
- [4] C. Netti, J.R. Lincoln, *Microscopy and Analysis* 19 (AM), 9-11 (2005).
- [5] G. Binnig, C. F. Quate, and Ch. Gerber; *Physical Review Letters* 56, 930 (1986).
- [6] J.K. Gimzewski, Ch. Gerber, E. Meyer and R.R. Schlittler, *Chem. Phys. Lett.* 217, 589-594 (1994).
- [7] R. Berger, E. Delamarche, H.P. Lang, Ch. Gerber, J.K. Gimzewski, E. Meyer and H.-J. Güntherodt, *Science* 276, 2021-2024 (1997).
- [8] R. Berger, Ch. Gerber and J.K. Gimzewski, *Analytical Methods & Instrum.*, Special Issue μ TAS'96, 74-77 (1996).
- [9] B. Ilic, H. G. Craighead, S. Krylov, W. Senaratne, C. Ober, P. Neuzil, *Journal of Applied Physics*, 95, 3694-3703 (2004).
- [10] N. Nugaeva, K.Y. Gfeller, N. Backmann, H.P. Lang, M. Düggelin, M. Hegner, *Biosensors and Bioelectronics*, 21, 849-856 (2005).
- [11] J.R. Barnes, R.J. Stephenson, M.E. Welland, Ch.Gerber and J.K. Gimzewski, *Nature* 372, 79-81 (1994).
- [12] T. Thundat, S.L. Sharp, W.G. Fischer, R.J. Warmack and E.A. Wachter, *J. Appl. Phys.* 66, 1563-1565 (1995).
- [13] J. Varesi, J. Lai, Z. Shi, T. Perazzo and A. Majumdar, *Appl.Phys. Lett.* 71, 306-308 (1997).

- [14] S.R. Manalis, S.C. Minne, C.F. Quate, G.G. Yaralioglu and A. Atalar, *Appl. Phys. Lett.* 70, 3311-3313 (1997).
- [15] R. Budakian, S. J. Putterman, *Applied Physics Letters*, 81, 2100-2102 (2002).
- [16] D. Rugar, H.J. Mamin, R. Erlandsson, J.E. Stern, B.D. Terris, *Rev. Sci. Instrum.* 59, 2337-2340 (1998).
- [17] Rugar, D. Budakian, R.; Mamin, H.J.; Chui, B.W., *Nature* 430, 329-332 (2004).
- [18] R.G. Knobel and A.N. Cleland. *Nature* 424, 291 (2003).
- [19] R. Raiteri, H.-J. Butt and M. Grattarola, *Electrochem. Acta* 46, 157-163 (2000).
- [20] H.-J. Butt, *J. Colloid and Interface Science* 180, 251-260 (1996).
- [21] Hai-Feng Ji, K.M. Hansen, Z. Hu, T. Thundat, *Sensors and Actuators B* 72 233-238 (2001).
- [22] J. Fritz, M. K. Baller, H. P. Lang, H. Rothuizen, P. Vettiger, E. Meyer, H.-J. Guntherodt, Ch. Gerber, J. K. Gimzewski, *Science* 288, 316-318 (2000).
- [23] Rachel McKendry, Jiayun Zhang, Youri Arntz, Torsten Strunz, Martin Hegner, Hans Peter Lang, Marko K. Baller, Ulrich Certa, Ernst Meyer, Hans-Joachim Guntherodt, and Christoph Gerber, *Proceeding of the National Academy of Sciences, USA* 99, 9783-9788 (2002).
- [24] N. V. Lavrik, M. J. Sepaniak, P. G. Datkos, *Rev. Sci. Instrum.* 75, 2229-2253 (2004).
- [25] K.M. Hansen, T. Thundat, *Methods* 37, 57-64 (2005).
- [26] L.G. Carrascosa, M. Moreno, M. Alvarez, L.M. Lechuga, *Trends in Analytical Chemistry*, In Press (2005).
- [27] Karolyn M. Hansen, Hai-Feng Ji, Guanghua Wu, Ram Datar, Richard Cote, Arunava Majumdar, and Thomas Thundat, *Anal Chem.* 73, 1567-1571 (2001).
- [28] M. Alvarez, L. G. Carrascosa, M. Moreno, A. Calle, A. Zaballos, L. M. Lechuga, C. Martinez-A, and J. Tamayo, *Langmuir* 20, 9663-9668 (2004).
- [29] Hiromi Kimura-Suda, Dmitri Y. Petrovykh, Michael J. Tarlov, and Lloyd J. Whitman, *J. Am. Chem. Soc.* 125, 9014-9015 (2003).

- [30] Guanhua Wu, Haifeng Ji, Karolyn Hansen, Thomas Thundat, Ram Datar, Richard Cote, Michael F. Hagan, Arup K. Chakraborty, and Arunava Majumdar, *Proceeding of the National Academy of Sciences, USA* 98, 1560–1564 (2001).
- [31] M. Calleja, M. Nordstrom, M. Alvarez, J. Tamayo, L.M. Lechuga, A. Boisen, *Ultramicroscopy* 105, 215–222 (2005).
- [32] U. Rant, K. Arinaga, S. Fujita, N. Yokoyama, G. Abstreiter, and M. Tornow, *Nano Lett.* 4, 2441-2445 (2004).
- [33] Hye Jin Lee, Yuan Li, Alastair W. Wark, and Robert M. Corn, *Anal. Chem.* 77, 5096-5100 (2005).
- [34] contact strips type H, Laird Technologies, USA
- [35] model 9064-Z, NewFocus, USA
- [36] model VE90, Thermionics Laboratories, USA
- [37] 99.99%, Plasma Materials, USA
- [38] 99.99%, Alfa Aesar, USA
- [39] The temperature of the sample inside the vacuum chamber is determined with a thermocouple attached to the sample plate. The temperature of the sample is therefore at least at the temperature recorded if not hotter.
- [40] J.E. Sader, J.W.M. Chon and P. Mulvaney, *Rev. Sci. Instrum.* 70, 3967–3969 (1999).
- [41] Bluesky Research FiberMax™ 635 Fiber-Pigtailed Modules, model # FMXL112-00, the laser diode module was operated at a current of 43 mA, the threshold current being at 39 mA. A variable pigtailed attenuator (from OZ-Optics, model BB-500) is used to lower the output power. The laser diode in this module is a Hitachi HL6334MG with 10mW power.
- [42] ILX lightwave precision current source, model LDX-3412
- [43] Brimrose, fiber optic patch cord.
- [44] 50/50 coupler (F-CPL-S12635) by Newport
- [45] Brimrose, custom built pigtailed fiber optic focuser.
- [46] MT Series Compact Dovetail Linear Stages, model MT-XYZ, Newport, USA
- [47] model 1L10, ON-TRAK Photonics, USA

- [48] Burr-Brown OPA111
- [49] OPA627BP Burr-Brown
- [50] Burr-Brown MPY634
- [51] Millipore Simplicity 185 water system
- [52] 98% purity, Aldrich, Canada
- [53] Sodium dodecyl benzenesulfonate 98% purity, Aldrich, Canada
- [54] A. Subramanian; P. I. Oden; S. J. Kennel; K. B. Jacobson; R. J. Warmack; T. Thundat; and M. J. Doktycz; *Applied Physics Letters* 81, 385 (2002).
- [55] H. P. Lang; M. K. Baller; R. Berger; Ch. Gerber; J. K. Gimzewski; F. M. Battiston; P. Fornaro; J. P. Ramseyer; E. Meyer; and H.-J. Güntherodt; *Analytica Chimica Acta* 393, 59 (1999).
- [56] Michel Godin, Vincent Tabard-Cossa, Peter Williams, and Peter Grütter, *Appl. Phys. Lett.* 79, 551 (2001).
- [57] Sarid D. *Scanning Force Microscopy with Applications to Electric, Magnetic and Atomic Forces* (Oxford University Press, New York, 1994), Chap. 1
- [58] R. J. Roark; "Formulas for Stress and Strain", McGraw-Hill Book Company, (1965).
- [59] S. Timoshenko, and D. H. Young; "Elements of Strength of Materials, 4th Ed.", Van Nostrand, New York, (1962).
- [60] L.Y. Beaulieu, Michel Godin, Olivier Laroche, Vincent Tabard-Cossa, and Peter Grütter, *Appl. Phys. Lett.* 88, 083108 (2006).
- [61] G. G. Stoney; *Proceedings of the Royal Society of London, Series A* 82, 172 (1909).
- [62] W.A. Brantley, *J. Appl. Phys.* 44, 534–535 (1973).
- [63] model SR770, Stanford Research, USA
- [64] K. Dahmen, S. Lehwald, H. Ibach, *Surface Science* 446, 161–173 (2000).
- [65] There is most certainly a native oxide layer on the silicon surface.
- [66] H.P. Lang, R. Berger, F. Battiston, J.-P. Ramseyer, E. Meyer, C. Andreoli, J. Brugger, P. Vettiger, M. Despont, T. Mezzacasa, L. Scandella, H.-J. Guntherodt, C. Gerber and J.K. Gimzewski, *Appl. Phys. A: Solids Surf.* 66, S61–S64 (1998).

- [67] H. Jensenius, J. Thaysen, A.A. Rasmussen, L.H. Veje, O. Hansen and A. Boisen, *Appl. Phys. Lett.* 76, 2615–2617 (2000).
- [68] TE technology, USA
- [69] R. M. Tromp, A. W. Denier van der Gon, and M. C. Reuter; *Physical Review Letters* 68, 2313 (1992).
- [70] K. Pohl, M. C. Bartelt, J. de la Figuera, N. C. Bartelt, J. Hrbek, and R. Q. Hwang; *Nature* 397, 238 (1999).
- [71] U. Tartaglino, E. Tosatti, D. Passerone, and F. Ercolessi; *Physical Review B* 65, 241406 (2002).
- [72] C. W. Mays, J. S. Vermaak, and D. Kuhlmann-Wilsdorf; *Surface Science* 12, 134 (1968).
- [73] H. J. Wasserman, and J. S. Vermaak; *Surface Science* 32, 168 (1972).
- [74] H. J. Wasserman and J. S. Vermaak, *Surface Science* 22, 164-172 (1970).
- [75] P. Müller and R. Kern, *Surface Science* 301, 386-398 (1994).
- [76] R.A. Fredlein, J.O'M. Bockris, *Surf. Sci.* 46, 641 (1974).
- [77] C. Friesen, N. Dimitrov, R. C. Cammarata, and K. Sieradzki, *Langmuir* 17, 807-815 (2001).
- [78] A. J. Bard, L. R. Faulkner, *Electrochemical Methods Fundamentals and Applications*, 2nd edition, (John Wiley & Sons, 2001), Chap. 13
- [79] D.C. Grahame, *Chem. Rev.* 41, 441 (1947).
- [80] R.G. Linford, *Chem. Rev.* 78, 81 (1978).
- [81] G. Lang, K.E. Heusler, *J. Electroanal. Chem.* 377, 1 (1994).
- [82] A simple way to obtain an estimate for the surface free energy of covalently bonded crystals is to determine the number of bonds which needs to be broken in order to expose a surface and multiply it with the energy per bond.
- [83] R. Shuttleworth; *Proceedings of the Physical Society A* 63, 444 (1950).
- [84] A. Sanfeld, A. Steinchen, *Surface Science* 463, 157–173 (2000).
- [85] D. J. Bottomley and T. Ogino, *Physical Review B* 63, 165412 (2001).
- [86] P. R. Couchman and C. R. Davidson, *J. Electroanal. Chem.* 85, 407-409 (1977).
- [87] Valincius G., *J. Electroanal. Chem.*, 478, 40-49 (1999).

- [88] Guidelli R., *J. Electroanal. Chem.*, 453, 69-77 (1998).
- [89] T.A. Brunt, T. Rayment, S.J. O'Shea, and M.E. Welland, *Langmuir* 12, 5942-5946 (1996).
- [90] T. A. Brunt, E.D. Chabala, T. Rayment, S. J. O'Shea, and Mark E. Welland, *J. Chem. Soc., Faraday Trans.*, 92, 3807 (1996).
- [91] S.J. O'Shea, M.E. Welland, T.A. Brunt, A.R. Ramadan, and T. Rayment, *J. Vac. Sci. Technol. B* 14, 1383-1385 (1996).
- [92] R. Raiteri and H.-J. Butt, *J. Phys. Chem.* 99, 15728-15732 (1995).
- [93] Tatsuya Miyatani and Masamichi Fujihira, *J. Appl. Phys.* 81, 7099-7115 (1997).
- [94] Tatsuya Miyatani and Masamichi Fujihira, *Jpn. J. Appl. Phys., Part 1* 36, 5280-5281 (1997).
- [95] F. Tian, J.H. Pei, D.L. Hedden, G.M. Brown, T. Thundat, *Ultramicroscopy* 100, 217 (2004). – also the published comments on this article by G.G. Lang, T.A. Rokob, G. Horanyi, *Ultramicroscopy* 104, 330–332 (2005).
- [96] M. Lahav, C. Durkan, R. Gabai, E. Katz, I. Willner, and M.E. Welland, *Angew. Chem. Int. Ed.* 40, 4095-4097 (2001).
- [97] M. Roemer, T. Kurzenknabe, E. Oesterschulze, and N. Nicoloso, *Anal. Bioanal. Chem.* 373, 754-757 (2002).
- [98] F. Quist, V. Tabard-Cossa, and A. Badia, *J. Phys. Chem. B* 107, 10691-10695 (2003).
- [99] D. M. Mohilner and T. R. Beck, *J. Phys. Chem.* 83, 1160-1166 (1979).
- [100] J. Lipkowski, W. Schmickler, D.M. Kolb, and R. Parsons, *J. Electroanal. Chem.* 452, 193-197 (1998).
- [101] H. Ibach, *Surf. Sci. Rep.* 29, 193-263 (1997).
- [102] W. Haiss, *Rep. Prog. Phys.* 64, 591-648 (2001).
- [103] W. Schmickler and E. Leiva, *J. Electroanal. Chem.* 453, 61-67 (1998).
- [104] H. Ibach, C. E. Bach, M. Giesen, and A. Grossmann, *Surf. Sci.* 375, 107-119 (1997).
- [105] W. Haiss, R. J. Nichols, J. K. Sass, and K. P. Charle, *J. Electroanal. Chem.* 452, 199-202 (1998).

- [106] Godin M. , Williams P. J., Tabard-Cossa V., Laroche O., Beaulieu L. Y., Lennox R. B., and Grütter P., *Langmuir*, 20, 7090-7096 (2004).
- [107] H.-J. Butt, K. Graf, M. Kappl, *Physics and Chemistry of Interfaces*, (John Wiley & Sons, 2003), Chap. 4
- [108] L. D. Burke, P. F. Nugent, *Gold bulletin*, 30 (1997).
- [109] Jacek Lipkowski, Zhichao Shi, Aicheng Chen, Bruno Pettinger and Christoph Bilger *Electrochimica Acta* 44, 1037-1052 (1998).
- [110] Shi Z., Lipkowski J., *J. Electroanal. Chem.* 403, 225-239 (1996).
- [111] Vasiljevic N., Trimble T., Dimitrov N., Sieradzki K. *Langmuir* 20, 6639-6643, (2004).
- [112] Heusler K.E., Pietrucha J., *J. Electroanal. Chem.* 329, 339 (1992).
- [113] Haiss W., Sass J. K., *Langmuir*, 12, 4311 (1996).
- [114] Ibach H., *Electrochimica Acta*, 45, 575-581 (1999).
- [115] M. W. Finnis and V. Heine; *Journal of Physics F: Metal Physics* 4, L37 (1974)
- [116] V. Heine and L. D. Marks; *Surface Science* 165, 65 (1986).
- [117] V. Fiorentini, M. Methfessel, and M. Scheffler, *Phys. rev. Lett.* 71, 1051-1054 (1993).
- [118] Godin M., PhD. Thesis, McGill University, Montreal, Canada (2004)
www.physics.mcgill.ca/SPM/Theses.htm
- [119] Xie R., Chen D., Wang X., He T., Liu F.C., *J. Phys. Chem. B*, 106, 12948-12956 (2002).
- [120] Sondag-Huethorst J. A. M., Fokkink L. G. J., *Langmuir*, 11, 2237-2241 (1995).
- [121] See reference 102 page 633-634
- [122] Smela E., *Adv. Mater.*, 15, 481-494 (2003).
- [123] Jager E. W. H., Smela E., and Inganäs O., *Science*, 290, 1540-1545 (2000).
- [124] Baughman R. H., *Synth. Met.*, 78, 339-353 (1996).
- [125] Gandhi M.R., Murray P., Spinks G.M., and Wallace G.G, *Synth. Met.*, 73, 247-256 (1995).
- [126] Smela E., *J. Micromech. Microeng.*, 9, 1-18 (1999).

- [127] Pei Q. and Inganäs O., *J. Phys. Chem.*, 97, 6034-6041 (1993).
- [128] Jager E. W. H., Inganäs O., and Lundström I., *Science*, 288, 2335-2338 (2000).
- [129] Bar-Cohen Y., Sherrit S. and Lih S.-S., *Smart materials and structures*, Proc. SPIE, 4329, 319-327 (2001).
- [130] Lahav M., Durkan C., Gabai R., Katz E., Willner I. and Welland M.E., *Angew. Chem. Int. Ed.*, 40, 4095-4097 (2001).
- [131] Roemer M., Kurzenknabe T., Oesterschulze E. and Nicoloso N., *Anal. Bioanal. Chem.*, 373, 754-757 (2002).
- [132] This value is obtained by integrating the area under the cathodic peak.
- [133] Pyo M., Bohn C. C., Smela E., Reynolds J. R. and Brennan A. B., *Chem. Mater.*, 15, 916-922 (2003).
- [134] Golan Y., Margulis L., and Rubinstein I., *Surf. Sci.*, 264, 312-326 (1992).
- [135] Pei Q.g and Qian R., *Electrochimica Acta*, 37, 1075-1081 (1992).
- [136] Smela E, and Gadegaard N., *J. Phys. Chem. B*, 105, 9395-9405 (2001).
- [137] Smela E., and Gadegaard N., *Adv. Mater.*, 11, 953-957 (1999).
- [138] Bay L., Jacobsen T., Skaarup S., and West K., *J. Phys. Chem. B*, 105, 8492-8497 (2001).
- [139] Bay L., Mogensen N., Skaruup S, Sommer-Larsen P., Jorgensen M., and West K., *Macromolecules*, 35, 9345-9351 (2002).
- [140] Rammelt U., Bischoff S., El-Dessouki M., Schulze R., Plieth W., and Dunsch L., *J. Solid State Electrochem.*, 3, 406-411 (1999).
- [141] Takashima W., Pandey S. S., and Kaneto K., *Sensors and Actuators B*, 89, 48-52 (2003).
- [142] Skaarup S., West K., Gunaratne L.M.W.K., Vidanapathirana K.P., and Careem M.A., *Solid State Ionics*, 136-137, 577-582 (2000).
- 143 Shimoda S., and Smela E., *Electrochimica Acta*, 44, 219-238 (1998).
- [144] Maw S., Smela E., Yoshida K., Sommer-Larsen P., and Stein R. B., *Sensors and Actuators A*, 89, 175-184 (2001).

- [145] Willicut R. J., and McCarley R. L., *Langmuir*, 11, 296-301 (1995).
- [146] Spinks G. M., Xi B., Zhou D., Truong V.-T., Wallace G.G., *Synth. Met.*, 140, 273-280 (2004).
- [147] Idla K., Inganäs O., Standberg M., *Electrochimica Acta*, 45, 2121-2130 (2000).
- [148] Weissmüller J., Viswanath R. N., Kramer D., Zimmer P., Würschum R., and Gleiter H., *Science*, 300, 312-315 (2003).
- [149] <http://www.veeco.com>, Santa-Barbara, USA
- [150] <http://www.concentris.ch>, Basel, Switzerland
- [151] <http://www.protiveris.com>, Rockville, USA
- [152] <http://www.cantion.com>, Lyngby, Denmark
- [153] <http://www.lunainnovations.com>, Blacksburg, USA
- [154] George S. Tulevski, Matt B. Myers, Mark S. Hybertsen, Michael L. Steigerwald, Colin Nuckolls, *Science* 309, 591 (2005).
- [155] T.A. Rokob, G.C. Lang, *Electrochimica Acta* 51, 93-97 (2005).